Dissertation
submitted to the
Combined Faculties for the Natural Sciences and for Mathematics
of the Ruperto-Carola University of Heidelberg, Germany
for the degree of
Doctor of Natural Sciences

presented by

Andreas Weller
born in: Gießen, Germany

Oral examination: June 24, 2009

Dynamics and Interaction of Dark Solitons in Bose-Einstein Condensates

Referees:	Prof. Dr. Markus K. Oberthaler
	Prof. Dr. Peter Schmelcher

In Gedenken an meine Mutter

Abstract: In this thesis we experimentally observe the dynamics of dark solitons in elongated Bose-Einstein condensates (BEC) in the crossover regime between 1D and 3D. Dark solitons are dynamically stable in this regime. This allows the observation of the collisional and oscillational dynamics of two dark solitons in a harmonically confined BEC over several oscillation periods. We can detect the repulsive inter-solitonic interaction as an increase of the oscillation frequency of the two solitons strongly depending on their mean distance. Thereby we give the first experimental evidence of the theoretically predicted repulsive interaction between the solitons. We compare our experimental findings to numerical simulations of the Gross-Pitaevskii equation and effective 1D equations. Additionally we develop a model in which the solitons are approximated by repulsively interacting classical particles. This model is based on a soliton interaction potential suggested by [Kiv1995] and can describe the essentials of the soliton dynamics. We observe well agreement between the soliton oscillation frequencies measured in the experiment, the numerical simulations and the results of the particle model. Besides we verify the theoretical prediction that the oscillation frequency of dark solitons in a harmonically confined BEC should be slower than the trap frequency.

Zusammenfassung: Im Rahmen dieser Arbeit wurde die Dynamik von dunklen Solitonen in zigarrenförmigen Bose-Einstein Kondensaten (BEC) im Übergangsregime zwischen 1D und 3D untersucht. In diesem Regime sind dunkle Solitonen stabil. Dies ermöglicht es die Kollisions- und Oszillations-Dynamik zweier dunkler Solitonen im harmonisch gefangenen BEC über mehrere Oszillationsperioden hinweg zu untersuchen. Dadurch kann die repulsive Wechselwirkung zwischen den Solitonen als ein Anstieg der Oszillationsfrequenz der beiden Solitonen, welcher stark von ihrem mittleren Abstand abhängt, detektiert werden. Dies ist der erste experimentelle Nachweis der seit langem theoretisch vorhergesagten repulsiven Wechselwirkung zwischen dunklen Solitonen. Wir vergleichen unsere experimentellen Erkenntnisse mit numerischen Simulationen der Gross-Pitaevskii Gleichung und effektiven 1D Gleichungen. Zusätzlich entwickeln wir ein Modell im Rahmen dessen die Solitonen als repulsiv wechselwirkende klassische Teilchen approximiert werden können. Dieses Model basiert auf einem Wechselwirkungs-Potential für Solitonen wie in [Kiv1995] vorgeschlagen. Es kann die Grundzüge der Solitonendynamik auf einfache Weise beschreiben. Die experimentell ermittelten Oszillationsfrequenzen der Solitonen werden in guter Übereinstimmung durch die numerischen Simulationen und die Ergebnisse des Teilchenmodells bestätigt. Außerdem konnte die theoretische Vorhersage, dass dunkle Solitonen in einem harmonisch gefangenen BEC langsamer oszillieren sollten als mit der Fallenfrequenz, bestätigt werden.

Contents

Chapter 1

Introduction: Solitons

Every wave packet in a linear dispersive medium suffers from spreading with time. Due to the superposition principle such a system can be decomposed into a set of linear Fourier modes which evolve independently in time with different phase velocities. Adding a nonlinear term to a linear equation couples the linear modes and destroys the validity of the superposition principle. This makes it possible in a nonlinear system to compensate the effect of dispersion by a strong enough nonlinearity and enables the creation of non-spreading structures. Such non-spreading structure is called a soliton. Nonlinear modes like solitons can be obtained analytically from a nonlinear equation by the method of inverse scattering transform [Zak1973, Kiv1993], if the equation is exactly integrable [Kiv1998].
The very first discovery of solitons was the observation of non-spreading water waves [Rus1844], which are described mathematically by the so-called Korteweg-de Vries equation [Kor1895]. Also the well known Tsunami wave is a soliton. Apart from hydrodynamics, solitons occur e.g. in solid state physics, mechanics, biophysics, optics and Bose-Einstein condensates (BECs). Depending on the underlying nonlinear equation different kinds of solitons can appear. Solitons have been observed as non-spreading wave packets [Rus1844, Mol1980, Gas1987, EieII2004] or as non-spreading kinks in the background medium [Emp1987, Kro1988, Wei1988] [Den1990, Den1992, Che1993] [Bur1999, Den2000] in a lot of different physical systems with nonlinear interaction. This nonlinearity can be realized by different effects in different media. In the case of BECs the inter-atomic interaction serves as nonlinearity whereas in the case of optical solitons various effects can support a nonlinearity. The most prominent one is the optical Kerr effect [Kiv1998] which occurs as an intensity dependent refractive index $n = n_0 + n_2 I$, with n_2 the second-order nonlinear refractive index and I the intensity. The dynamics of many of these nonlinear systems can be described by formally similar equations. Therefore results gained in one system can be transferred to others.

In the fields of optics and BECs two families of solitons are distinguished: bright and dark (kink) solitons [Kiv1998]. Non-spreading wave packets are called bright solitons, whereas non-spreading kink states are called dark solitons. In optics the later describe intensity dips in the background field and non-spreading density dips in a BEC respectively. The solitons in both fields are described, in their idealized form, by the same kind of homogeneous nonlinear Schrödinger equation of the form:

$$i\frac{\partial u}{\partial x} = -\frac{1}{2}\frac{\partial^2 u}{\partial z^2} + \sigma|u|^2 u \tag{1.1}$$

In the case of $\sigma = -1$ the nonlinearity is attractive (or focusing respectively) and supports bright solitons. The corresponding solution for the fundamental (stationary) bright soliton takes the form [Kiv1993, Kiv1998] (see Fig. 1.1):

$$u(z, x) = a\,\mathrm{sech}(az)e^{ia^2x}, \tag{1.2}$$

with the amplitude a.
For $\sigma = +1$, dark solitons are supported and the fundamental dark soliton is described by [Kiv1993, Kiv1998] (see Fig. 1.1):

$$u(z, x) = u_0 \tanh(u_0 z)e^{iu_0^2x}, \tag{1.3}$$

with the background density u_0. The dark solitons in Bose-Einstein condensates regarded in this thesis behave the same way as spatial dark solitons in nonlinear optical Kerr-media. In contrast to the field of BEC, in optics one has to distinguish between spatial and temporal solitons. Spatial optical solitons are solitons in the transverse intensity profile of a laser beam and are described by Eqn. 1.2 and Eqn. 1.3 with the spatial coordinates (z,x). Temporal optical solitons occur as non-dispersive laser pulses or non-dispersive intensity dips in these pulses in the coordinate system (x,t). Here x denotes the direction of beam propagation and t the time. A historic introduction to solitons can be found in [Ron2008].

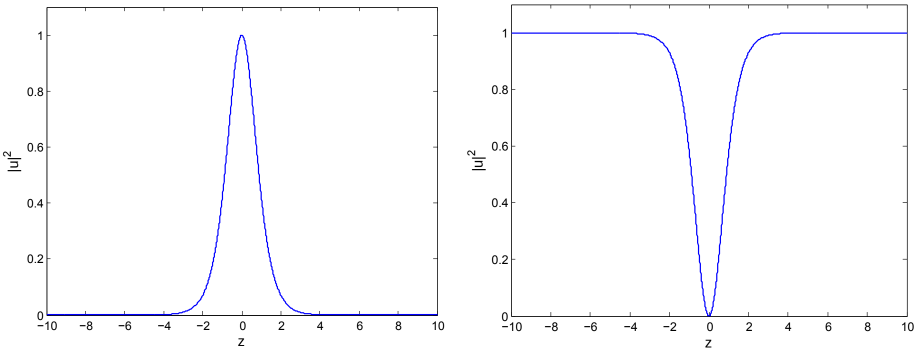

Figure 1.1: **left**: fundamental bright soliton, $a = 1$. **right**: fundamental dark soliton, $u_0 = 1$.

In this thesis we will focus on dark solitons in BECs. We will discuss experiments creating dark solitons in a harmonic trap by means of matter wave interference. Our observations will focus on the oscillation frequencies of the solitons and on their mutual interaction. The thesis is divided into four main chapters. Chapter 2 will provide the reader with the theoretical basics of dark soliton physics in BECs. In chapter 3 we present our experimental technique of creating the solitons. Chapter 4, the main part of this work, will discuss our experimental findings of the oscillation frequencies and interaction of dark solitons in BECs. Finally, we will describe our experimental apparatus and methods in chapter 5.

Chapter 2

Dark solitons in Bose-Einstein condensates: Theoretical approach

In the field of Bose-Einstein condensates (BECs) dark solitons are non-spreading dips in the atom density distribution of a BEC. If more than one of such structure is created in a harmonically confined BEC interesting oscillation- and interaction-dynamics will occur. These are the content of our experiments (see chapter 4).

In this chapter we will provide the reader with the theoretical basics of dark solitons in BECs in view of the experiments performed in the context of this thesis (see chapter 4). Starting from the ideal one-dimensional homogeneous case we will go over to the experimental situation of dark solitons in harmonically trapped BECs including the repulsive interaction between the solitons. Since analytic solutions exist for the one-dimensional homogeneous case we will extract details of the general collisional behavior of dark solitons from these. For the experimental case numerical simulations will be performed showing the effects of dimensionality of the system and the inter-soliton interaction. We will develop a model regarding the solitons as particles in an effective potential which helps to distinguish these two effects.

2.1 The one-dimensional homogeneous regime

We start with the discussion of analytic descriptions that have been developed for the case of one and two dark solitons in the homogeneous one-dimensional (1D) regime. As we will see these descriptions also include soliton collisions.

2.1.1 The analytic single dark soliton solution

Mathematically a dark soliton is an analytic solution of the general homogeneous nonlinear Schrödinger equation (NLSE, see Eqn. 1.1), first described by Zakharov and Shabat [Zak1972]. This equation is formally equal to the homogeneous one-dimensional Gross-Pitaevskii equation (1D GPE) describing the idealized case of a one-dimensional Bose-Einstein condensate (see also section 2.2.1):

$$i\hbar\frac{\partial}{\partial t}\Psi(z,t) = \left[-\frac{\hbar^2}{2m}\frac{\partial^2}{\partial z^2} + g_{1D}|\Psi(z,t)|^2\right]\Psi(z,t). \tag{2.1}$$

In the 1D case the one-dimensional constant of atomic interaction in Eqn. 2.1 is given by $g_{1D} = gm\omega_\perp/(2\pi\hbar) = 2\hbar\omega_\perp a_s$ with the s-wave scattering length a_s, the transverse trapping frequency $\omega_\perp = 2\pi\nu_\perp$ and the three-dimensional interaction constant $g = 4\pi\hbar^2 a_s/m$. The NLSE and the homogeneous 1D GPE[1] are connected by the following transformation:

1D GPE	$\leftrightarrow$	NLSE
t	$\leftrightarrow$	$\frac{\hbar}{gn}\tilde{t}$
z	$\leftrightarrow$	$\frac{\hbar}{\sqrt{gnm}}\tilde{z}$
$\Psi(z,t)$	$\leftrightarrow$	$\sqrt{n}\cdot u(\tilde{t},\tilde{z})$

One excitation of Eqn. 2.1 is the so called kink state or also called dark soliton [Fed1999, Bur2002]:

$$\Psi_d(z,t) = \sqrt{n}\left[i\nu + \sqrt{1-\nu^2}\tanh\left[\sqrt{1-\nu^2}\frac{(z-\nu c_s t)}{\xi}\right]\right]e^{itc} \tag{2.2}$$

$$c = \mu/\hbar, \tag{2.3}$$

$$\nu = v_d/c_s \tag{2.4}$$

with the homogeneous atomic background density n, the velocity of the soliton v_d, the Bogoliubov speed of sound $c_s = \sqrt{ng/m}$, the chemical potential $\mu = ng$ and the healing length $\xi = \hbar/\sqrt{mng}$. As can be seen from Eqn. 2.2 the dark soliton exhibits a phase jump and a resulting density notch exhibiting a width on the order of the healing length ξ (see Fig. 2.1).

According to its speed the depth of this density notch n_d is described by $n_d/n = 1-\frac{v^2}{c_s^2}$. We define the darkness of the soliton as $B = \sqrt{1-\frac{v^2}{c_s^2}} = \sqrt{n_d/n}$. A really black, stationary soliton, has a sharp phase jump of π whereas a grey, moving soliton, has a less sharp and smaller phase jump. Regardless of the darkness of the soliton we will use the general term dark soliton in the following. The speed of the soliton is always smaller than the speed of sound $v_d < c_s$. For $v_d \to c_s$, the wavefunction of the soliton Ψ_d becomes identical to the ground state of the condensate, in the considered case a homogeneous density distribution. As the stationary dark soliton is an excited state it has a higher energy than the ground state. Therefore, one can regard the moving soliton exhibiting a negative kinetic energy. This kink-related kinetic energy can be calculated to be $-\frac{1}{2}\Psi_d\frac{d^2\Psi_d}{dz^2}$. For the black soliton, this yields $-\tanh^2(z/\xi)/(\cosh^2(z/\xi))$ [Mur1999].

---

[1] Note: In this section we give all soliton equations in the form of the homogeneous 1D Gross-Pitaevskii equation (hom. 1D GPE, see Eqn. 2.1) relevant for BECs. If the constants $\hbar$, m (atomic mass), n (atomic density), $c = ng/\hbar$, ξ (healing length), g (constant of inter-atomic interaction), $\nu_\perp$ (transverse trap frequency) and c_s (Bogoliubov speed of sound) are substituted in the following way the equations transform into the form resulting from the general nonlinear Schrödinger equation (NLSE, see Eqn. 1.1): $\hbar \to 1$, $m \to 1$, $n \to 1$, $c \to 1$, $\xi \to 1$, $g \to 1$, $\nu_\perp \to 1$ and $c_s \to 1$.

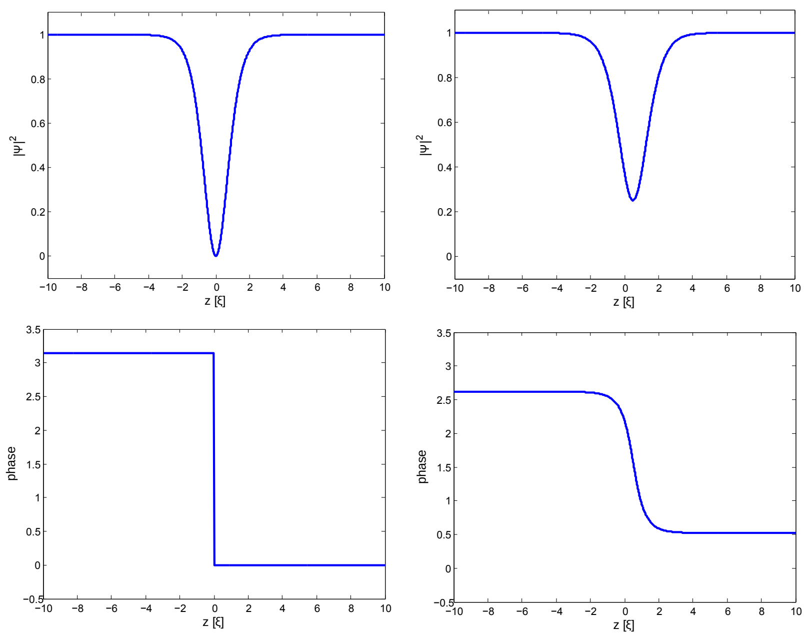

Figure 2.1: A dark soliton is connected to a gradient of the phase of the wavefunction and a resulting density notch depending on its velocity. The width of this density dip is on the order of the healing length. **Top left**: Density profile for $v_d = 0$. **Top right**: Density profile for $v_d = 0.5c_s$. **Bottom left**: Phase profile for $v_d = 0$. **Bottom right**: Phase profile for $v_d = 0.5c_s$.

2.1.2 Two-dark-soliton solutions

Based on the work of Zakharov and Shabat [Zak1972], Blow and Doran [Blo1985] have derived an equation which allows to calculate the full propagation of two dark solitons in a homogeneous medium including their collision. For the case of a homogeneous 1D Bose gas the solution takes the following form:

$$\begin{aligned}\Psi_{2d}(z,t) = [1 - \frac{2i}{\Gamma}[\frac{2}{B_1+B_2}\left(\frac{1}{iB_1+\nu_1}+\frac{1}{iB_2+\nu_2}\right)\\ + (iB_1-\nu_1)\left(\frac{1}{B_1}+\frac{e^{2\frac{z}{\xi}B_1}}{\mu_1}\right) + (iB_2-\nu_2)\left(\frac{1}{B_2}+\frac{e^{2\frac{z}{\xi}B_2}}{\mu_2}\right)]]e^{-2it\mu/\hbar},\end{aligned} \tag{2.5}$$

with

$$\begin{aligned}\Gamma =& (\nu_1 - iB_1)(\nu_2 - iB_2)\left(\frac{e^{2\frac{z}{\xi}B_1}}{\mu_1}+\frac{1}{B_1}\right)\left(\frac{e^{2\frac{z}{\xi}B_2}}{\mu_2}+\frac{1}{B_2}\right) - \\ & \frac{1}{(B_1+B_2)^2}\left(\frac{1}{\nu_1+iB_1}+\frac{1}{\nu_2+iB_2}\right)^2, \\ \mu_j =& e^{2B_j(z_j^0/\xi+2\nu_j tc)}, \\ B_j =& \sqrt{1-\nu_j^2}, \\ \nu_j =& v_d^j/c_s, \quad with \quad j=1,2,\end{aligned} \tag{2.6}$$

v_d^j the velocities of the solitons and c_s the Bogoliubov speed of sound. The constants z_j^0 set the initial positions of the solitons. Using this equation we can calculate the time evolution of two solitons with arbitrary velocities in a homogeneous one-dimensional BEC. This is exemplified in Fig. 2.2.

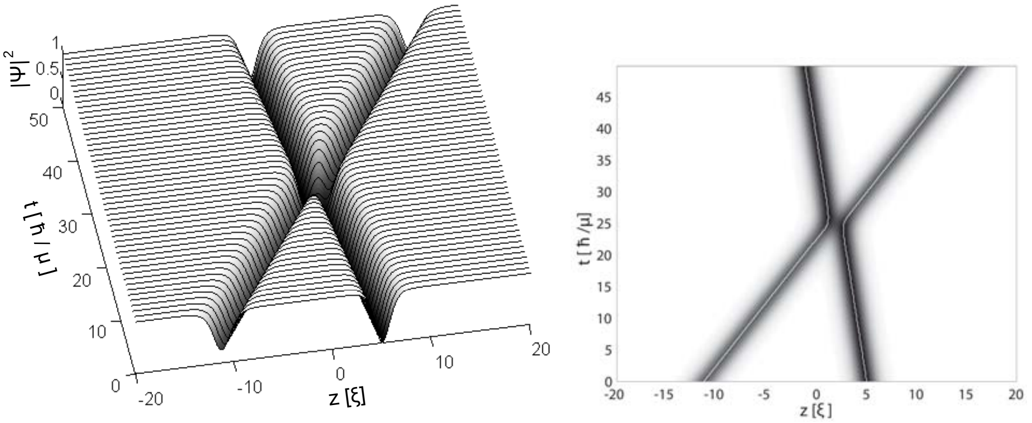

Figure 2.2: Collision of two dark solitons calculated by Eqn. 2.5, with $\nu_1 = 0.5$, $\nu_2 = 0.1$. a) 3D plot. b) Color scale plot showing the trajectories of the density minima as the white lines.

For the case of two solitons moving with equal opposite velocities Eqn. 2.5 can be simplified as derived by Akhmediev and Ankiewicz [Akh1993]:

$$\Psi_{2d}(z,t) = \frac{(1-2\nu^2)\cosh(2t\nu Bc) - \sqrt{\nu^2}\cosh(2Bz/\xi) + 2i\nu B\sinh(2t\nu Bc)}{\cosh(2t\nu Bc) + \sqrt{\nu^2}\cosh(2Bz/\xi)} e^{itc}, \qquad (2.7)$$

with $c = ng/\hbar$. Eqn. 2.7 is symmetric in time with the point of closest approach of the two solitons at $t = 0$.

2.1.3 Investigating the inter-soliton interaction during soliton collisions

As the two-soliton solutions cover cases where two solitons approach each other during their propagation, the question how the solitons behave in such collision arises. In section 2.1.4 we will discuss the collisional behavior of dark solitons and use analytic solutions to calculate the effect of a collision on their propagation trajectories. E.g. Fig. 2.3a reveals that two dark solitons interact repulsively when they get close to each other. In section 2.1.6 we will extract an inter-soliton interaction potential from Eqn. 2.7 which confirms the repulsive character of the inter-soliton interaction. This will also reveal that the interaction is of a short range nature with a length scale on the order of the healing length of the condensate.

2.1.4 Symmetric collisions of dark solitons observed in the analytic solutions

In order to take a closer look on the collisions of dark solitons, we will start with the symmetric case of $v_1 = -v_2$, where $v_{1,2}$ denotes the velocity of each of the two colliding solitons. We will use the analytic soliton solutions to investigate the behavior of the solitons on the collision point in detail. In view of the soliton interaction potential of section 2.1.6 one key point will be the estimation of the critical velocity below which the solitons always stay separated during a collision.

Collisions observed in two-soliton solutions

For the case of head on collisions with equal absolute values of the velocities it is possible to derive an equation from Eqn. 2.7 which determines the distance $2z_0$ between the solitons on the point of closest proximity [The, Kev]:

$$z_0 = \frac{1}{2\sqrt{n - n_{min}}} \cosh^{-1}\left(\sqrt{\frac{n}{n_{min}}} - 2\sqrt{\frac{n_{min}}{n}}\right)\xi, \tag{2.8}$$

with $n_{min}/n = 1 - (n_d/n) = v_d^2/c_s^2$ denoting the minimal density n_{min} at the density notch of each soliton for $t \to -\infty$ and the background density n. The existence of such minimal distance during a collision implies that the solitons slow down to zero and change the sign of their velocity. This also means, that $n_{min}/n = 0$ on the turning point as a soliton with $v_d = 0$ is really black. Increasing the initial velocities of the solitons leads to a critical point at $v_d^c = 0.5c_s$, where each soliton exhibits an initial density minimum of $n_{min}/n = v_d^2/c_s^2 = 0.25$. From Eqn. 2.8 we learn that for this critical value of $v_d^c = 0.5c_s$ the distance between the centers of the solitons becomes $2z_0 = 0$ at the collision point, meaning that they completely overlap. For velocities $v_d > 0.5c_s$ the two density minima even stick together for a certain time

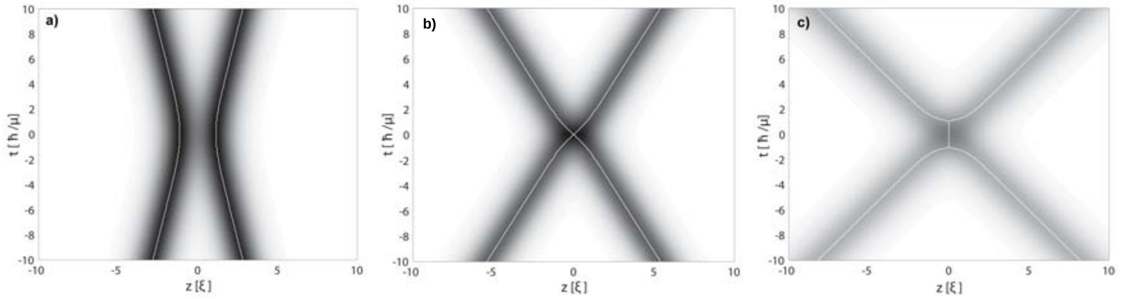

Figure 2.3: Symmetric collision ($\nu_1 = -\nu_2$) of two dark solitons for different velocities calculated by Eqn. 2.7. Trajectories of the density minima are marked by the white lines. a) $\nu = |\nu_1| = |\nu_2| = 0.2$, the two density minima are always well separated. b) $\nu = 0.5$, the density minima overlap on one point. c) $\nu = 0.8$, the minima overlap, stick together for a certain time and separate again. In b) and c) it is impossible to assign the two density dips to one or to the other trajectory after the collision.

during their collision before they separate again. In this case the density on the collision point becomes $n_{min}^{cp} > 0$ as can be seen in Figs. 2.3, 2.4 and 2.7.

Eqn. 2.8 points out that two different regimes can occur during the collision depending on the speed of the solitons. Both are exemplified in Fig. 2.3a and c. In the first regime (Fig 2.3a), the two solitons approach each other with opposite sign but otherwise equal velocities and $v_d < 0.5c_s$. Here the solitons very much behave like repulsively interacting classical particles. In the case $v_d \ll 0.5c_s$, even at the point of closest approach, the density between the two solitons hardly differs from the background density. In the second regime (Fig 2.3c) the starting conditions are similar, but the solitons approach with $v_d > 0.5c_s$. Here, the two density minima form a single density dip during the collision and the total density at the collision point is always different from 0: $n_{min}^{cp} > 0$. Fig. 2.3b shows the limit between the two regimes where $v_d = 0.5c_s$ and the solitons overlap completely only in one point during their time evolution. We illustrate this in Fig. 2.4. Therefore, one might suppose that for $v_d \geq 0.5c_s$ the two solitons pass through each other. If in contrast, the solitons were regarded as being reflected they would undergo a discontinuity of their velocities. Their velocities would have to change their signs instantaneously during the collision without decelerating to 0. Remember that the absolute value of the velocity of a soliton is directly connected to the darkness of the soliton. But regardless of wether solitons were reflected or transmitted, the trajectories of their density minima behave in a way at the collision point that suggests that the two solitons are firstly accelerated, then come to rest instantaneously, re-accelerate instantaneously again and finally decelerate after the collision as shown in Fig. 2.3c. In a classical particle picture this would not only be a contradiction to a repulsive collision but also an

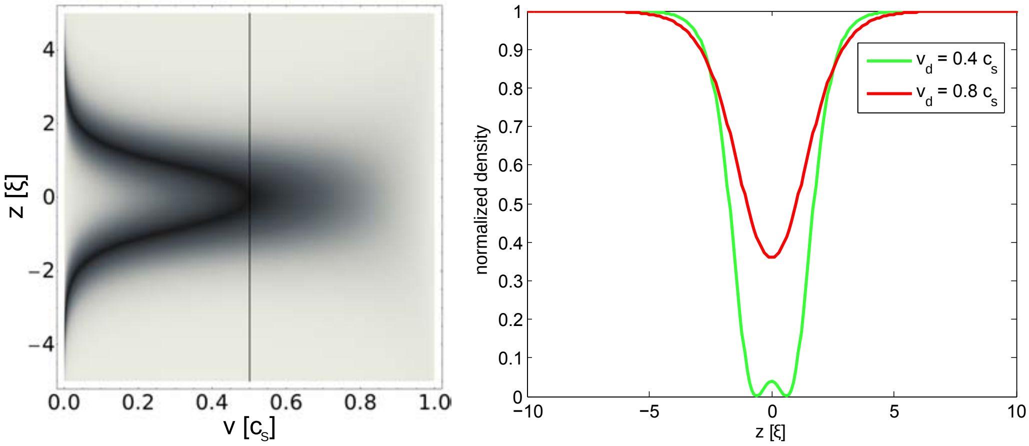

Figure 2.4: **Left**: Density profiles at the collision time, $t = 0$, calculated from Eqn. 2.7 for different initial velocities $\nu = v_d/c_s$ of the solitons. **Right**: Density profiles at $t = 0$ for two different initial velocities of the solitons. For $v_d = 0.4c_s$ the two density minima stay always seperated, exhibiting zero density on the point of closest approach. For $v_d = 0.8c_s$ the two minima completely overlap during the collision and the density at the collision point is higher than zero.

unphysical behavior. This points out that dark solitons cannot be regarded as particles in the regime $v_d \geq 0.5c_s$. As the solitons completely overlap in this regime like shown in Fig. 2.3c they are additionally no longer distinguishable after the collision and cannot be assigned to one or the other trajectory. The question if solitons cross through each other or get reflected for $v_d \geq 0.5c_s$ always leads to contradictions and cannot be answered. On this point we can only make a definition as we will do in section 2.1.5.

Scattering of two separated single soliton solutions

Zakharov and Shabat have investigated the collision of two solitons using the inverse scattering method [Zak1973]. They demonstrate that dark solitons interact with each other with a repulsive short range interaction. In their approach the two-soliton solution is regarded as breaking up into two individual solitons for asymptotic times $t \to \pm\infty$

$$\Psi(z,t) \to \Psi_d(z-\nu_1 c_s t, \nu_1, z_1^+) + \Psi_d(z-\nu_2 c_s t, \nu_2, z_2^+), t \to +\infty \tag{2.9}$$

$$\Psi(z,t) \to \Psi_d(z-\nu_1 c_s t, \nu_1, z_1^-) + \Psi_d(z-\nu_2 c_s t, \nu_2, z_2^-), t \to -\infty \tag{2.10}$$

where $z_{1,2}^{\pm}$ denotes the position of each soliton. It is stated, that the solitons preserve their velocities after collisions. Under this assumption the only effect each soliton experiences is a shift of its phase, resulting in a spatial shift of its trajectory like exemplified in Fig. 2.5. This shift can be calculated as

$$\delta z_1 = z_1^+ - z_1^-, \quad \delta z_2 = z_2^+ - z_2^- \tag{2.11}$$

and results in

$$\delta z_1 = \frac{1}{2B_1} \ln \frac{(\nu_1-\nu_2)^2 + (B_1+B_2)^2}{(\nu_1-\nu_2)^2 + (B_1-B_2)^2} \xi \tag{2.12}$$

$$\delta z_2 = -\frac{1}{2B_2} \ln \frac{(\nu_1-\nu_2)^2 + (B_1+B_2)^2}{(\nu_1-\nu_2)^2 + (B_1-B_2)^2} \xi . \tag{2.13}$$

If the absolute values of the solitons' velocities are equal, $\nu_1 = -\nu_2$, the shift is the same for both solitons and Eqn. 2.13 simplifies to:

$$\delta z = -\frac{\ln[|\nu_1|]}{B_1} \xi . \tag{2.14}$$

As the spatial shift of the trajectories is always in direction of the velocity of each individual soliton the interaction is of repulsive nature [Zak1973] (see Fig. 2.6).

We emphasize that this approach cannot be used to describe the dynamics at the collision point of the solitons. As shown in Fig. 2.6 the definition that each soliton preserves its velocity including its propagation direction for $t \to \infty$ leads to problems there. For instance this definition assumes the density notch of each soliton to

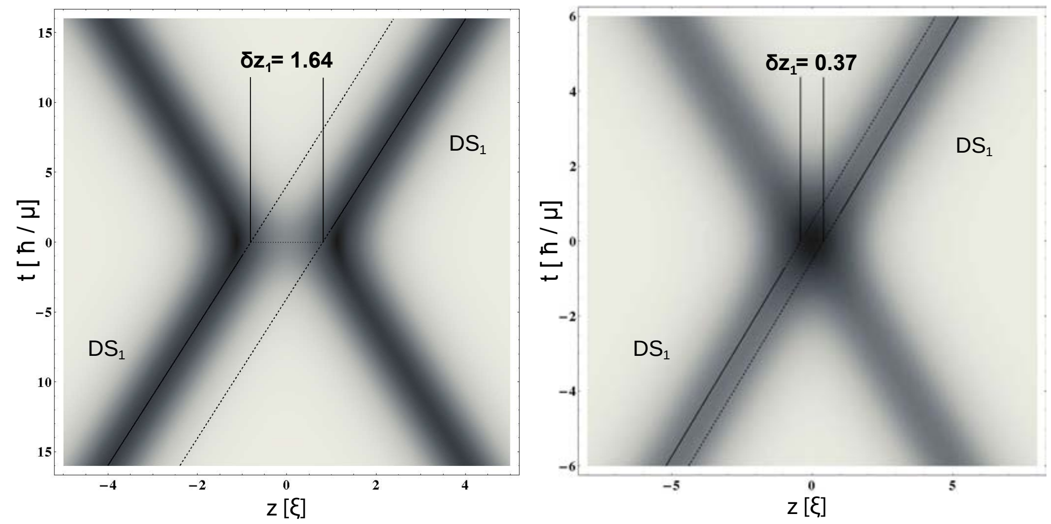

Figure 2.5: Spatial shift of the soliton trajectory of soliton 1 (DS1) as predicted by Eqn. 2.14 and evolution of the full density profile calculated by Eqn. 2.7. a) $\nu = 0.2$. b) $\nu = 0.8$.

undergo a jump in position at the collision point, for the case of $\nu < 0.5$. In a classical particle picture this would be an unphysical discontinuity of the trajectories.
One has to remember that Zakharov and Shabat confined their calculation on the asymptotic behavior $t \to \pm\infty$ [Zak1973]. They have used separated wavefunctions for the two solitons which is valid as they show for $t \to \pm\infty$ and breaks down for small distances between the solitons. Therefore it is not surprising that this approach fails to describe the detailed dynamics of the density minima at the collision point. Its strength is the ability to describe the asymptotic behavior of the soliton trajectories correctly for $t \to \pm\infty$ for all regimes.

2.1.5 The different collisional regimes

We have seen that dark solitons interact repulsively in collisions. The dependence of the minimal distance $2z_0$ between two solitons during a symmetric collision on $\nu = v_d/c_s$ is shown in Fig. 2.7, as calculated from Eqn. 2.8. Additionally the dependence of the spatial shift of their trajectories calculated by Eqn. 2.14 is plotted. We conclude that for $v_d < 0.5c_s$ dark solitons are reflected similar to classical particles. As mentioned above for the regime $v_d \geq 0.5c_s$ the question if two dark solitons get reflected during a symmetric collision or pass through each other cannot be answered and is a matter of definition. If willing to make such definition one has to regard the two approaches describing soliton collisions which are summarized as follows:

a) **Two separated single soliton wavefunctions for $t = \pm\infty$.** This approach has been used by Zakharov and Shabat applying the method of inverse scattering transform [Zak1973]. It describes the trajectories of the solitons correctly for $t \to \pm\infty$. Only close to the collision point contradictions occur. The solitons

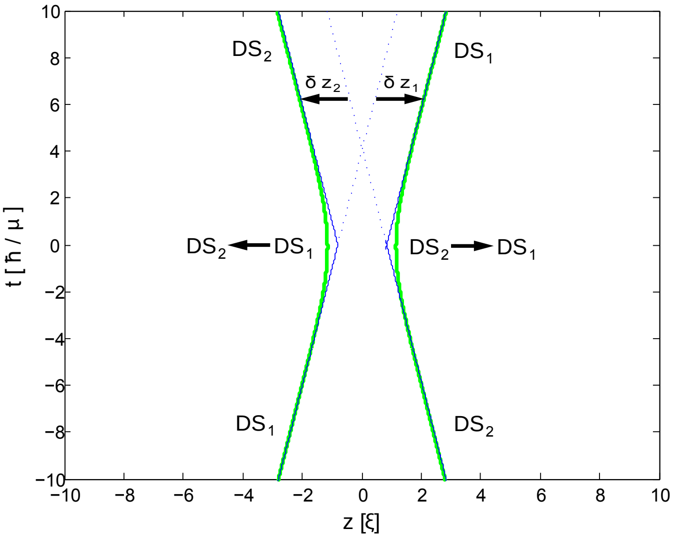

Figure 2.6: Schematic dark soliton trajectory shifts as predicted by [Zak1973]. green: trajectories of the density minima, blue: asymptotic trajectories calculated by Eqn. 2.14. The shift for soliton1 (DS1) is always positive $\delta z_1 > 0$ and the one for DS2 is always negative $\delta z_1 < 0$. This allows to conclude a repulsive interaction for dark solitons. Per definition the solitons have to jump to the opposite trajectory at $t = 0$. This points out, that the calculation by [Zak1973] can only give the correct trajectories for $t \to \pm\infty$.

are defined as always being transmitted through each other. This results in a contradiction as in the case of slow solitons with $v_d < 0.5c_s$, each soliton is shifted in space instantaneously.

b) An analytic two-soliton wavefunction. This approach has been used by Blow and Doran [Blo1985] as well as by Akhmediev and Ankiewicz [Akh1993]. It allows the calculation of the full time evolution of two solitons in the homogeneous one-dimensional case. From Eqn. 2.7 one can derive a formula (Eqn. 2.8) which determines the distance of the density minima of the two solitons at their closest approach during the collision. In head on collisions and for $v_d < 0.5c_s$ the approach results in trajectories of the soliton minima similar to the behavior of repulsively interacting classical particles. For $v_d > 0.5c_s$ it suggests on first sight that the solitons pass through each other, because of the not vanishing density at the collision point. But looking in detail on the behavior of the density minima close to the collision point, it becomes obvious that for $v_d \geq 0.5c_s$ they stick together for a certain time, so that it becomes impossible to distinguish the two solitons afterwards.

As we see none of the two descriptions can describe the collisional behavior of dark solitons contradiction-free in all regimes.

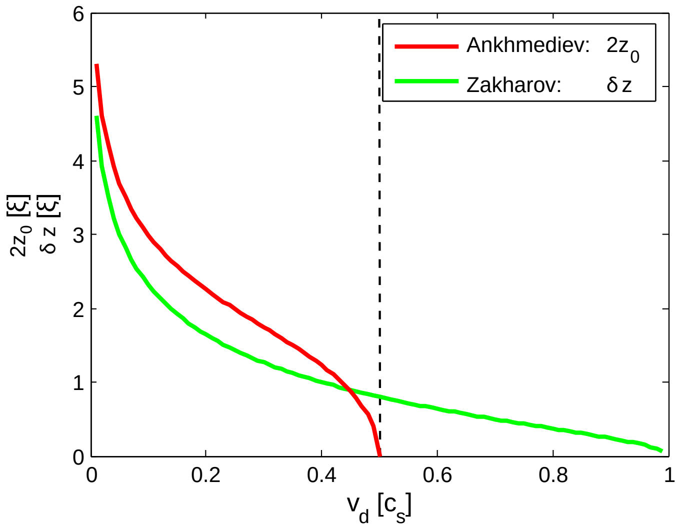

Figure 2.7: Minimal distance $2z_0$ between the solitons for different velocities ν as calculated from Eqn. 2.8 and shift of the soliton trajectories as calculated from Eqn. 2.14. The case of symmetric collisions $\nu = |\nu_1| = |-\nu_2|$ is regarded.

In our perception throughout this work we make the following definition. We regard two dark solitons in symmetric head on collisions with $v_d < 0.5c_s$ as being reflected similarly to repulsively interacting classical particles. In the case of $v_d \geq 0.5c_s$ we regard them as density dips passing through each other and undergoing a spatial shift during their collision, keeping in mind that regarding them as particles would never be free of contradiction in this regime.

2.1.6 The interaction potential approach for soliton collisions

Symmetric collisions of two solitons

Since the analytic two-soliton solutions and as well the phase shifts stemming from the inverse scattering method are only valid in the one-dimensional homogeneous case it would be useful to extract a soliton interaction potential from these analytic solutions. This might enable one to directly apply the soliton interaction in any regime, maybe even in a realistic experimental situation. This opens the possibility of not being dependent on numerical simulations to predict the soliton trajectories after a collision. An approach of Kivshar and Krolikowski [Kiv1995] describes the repulsive interaction between two dark solitons by regarding them as particles exhibiting a velocity dependent interaction potential. We will see in section 2.5.1 that it is possible to include this interaction potential together with the influences of a harmonic confinement in an effective potential, which then indeed can describe the soliton trajectories in a good approximation.

This soliton interaction potential is derived in [Kiv1995] based on the analytic two-soliton solution Eqn. 2.7 stemming from [Akh1993] and under the assumption, that the solitons are always well separated. It is valid for two dark solitons with $\dot{z} = \nu_1 c_s = -\nu_2 c_s$ in the one-dimensional homogeneous case and reads as follows [2]:

$$V(z,\dot{z}) = \frac{\mu B^2}{2m\sinh^2(2Bz/\xi)}, B = \sqrt{1 - \frac{(\dot{z}/\xi)^2}{c_s^2}}, \tag{2.15}$$

with $z = -z_1 = z_2$ the position of the solitons. According to this model the solitons

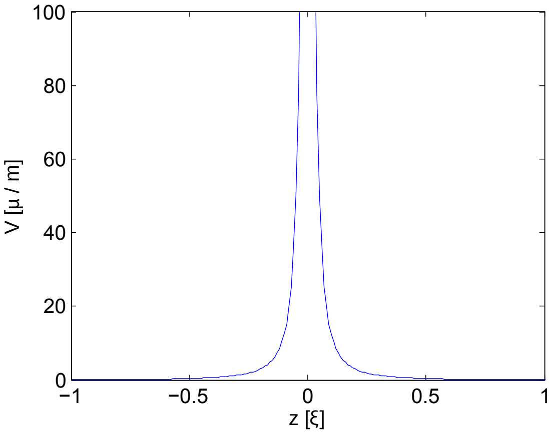

Figure 2.8: Simplified plot of the interaction potential assuming that always $B = 1$.

are regarded as classical particles moving in a potential given by Eqn. 2.15. We learn from Eqn. 2.15, that the interaction is of repulsive nature and has a short range character with a length scale on the order of the healing length ξ. Additionally we see that the interaction is velocity dependent. The slower the solitons the stronger the interaction. Furthermore the chemical potential of the condensate μ influences the potential strength. From Eqn. 2.15 an equation of motion for dark solitons moving in this interaction potential can be derived using the Lagrange equation:

$$\begin{aligned} &\frac{d}{dt}\left(\frac{\partial \mathfrak{L}}{\partial \dot{z}}\right) = \frac{\partial \mathfrak{L}}{\partial z} \\ &\mathfrak{L} = T - V = \frac{\dot{z}^2}{2} - V(z,\dot{z}) \end{aligned} \tag{2.16}$$

$$\Rightarrow \ddot{z}\left(1 - \frac{\partial^2 V}{\partial \dot{z}^2}\right) - \frac{\partial^2 V}{\partial z \partial \dot{z}}\frac{\partial z}{\partial t} + \frac{\partial V}{\partial z} = 0 \tag{2.17}$$

As the potential is symmetric $z = -z_1 = z_2$ also the equation of motion for each of the two solitons can be determined like: $\ddot{z} = -\ddot{z}_1 = \ddot{z}_2$. The interaction potential has

---

[2] Note that the potential shown here differs from the one shown in [Kiv1995] and used in [Wel2008] as it contains a sinh instead of a cosh. [Kev] found out while reconstructing the derivation of Eqn. 2.15, that the sinh is the formally correct function here. This was confirmed by W. Krolikowski, one of the authors of [Kiv1995]. But as the derivation of Eqn. 2.15 explicitly assumes that the potential is valid when the two solitons do not overlap, only the asymptotic behavior of the function is important which is the same for sinh and cosh. In this validity regime of Eqn. 2.15 no significant deviation occurs if cosh is changed to sinh.

been derived in [Kiv1995] under the assumption, that the two solitons are well separated. From Eqn. 2.8 we have calculated, that this is only the case for $v_d < 0.5c_s$. The green lines in Fig. 2.9 represent trajectories obtained from the equation of motion Eqn. 2.17 for three different velocities. Additionally we plot the analytic result obtained from Eqn. 2.7. We mark the trajectories of the density minima of the analytic result as the white lines. We see that for $v_d = 0.2c_s$ the green and white trajectories completely overlap. This shows that the picture of classical particles exhibiting an interaction potential is an excellent description for slowly moving solitons. For $v_d \geq 0.5c_s$ the behavior of the trajectories of the density minima obtained from the analytic result at the collision point is very different from the trajectories obtained with the interaction potential description. This emphasizes the breakdown of the particle model for $v_d \geq 0.5c_s$. Additionally we perform a comparison of the analytically obtained spatial shift of the soliton trajectories obtained from Eqn. 2.14 and the shift obtained from the result of the equation of motion 2.17. We come to the same conclusion as before. As shown in Fig. 2.10 the shifts predicted by the interaction potential differs from the analytic result for $v_d \geq 0.5c_s$. Yet for $v_d < 0.5c_s$

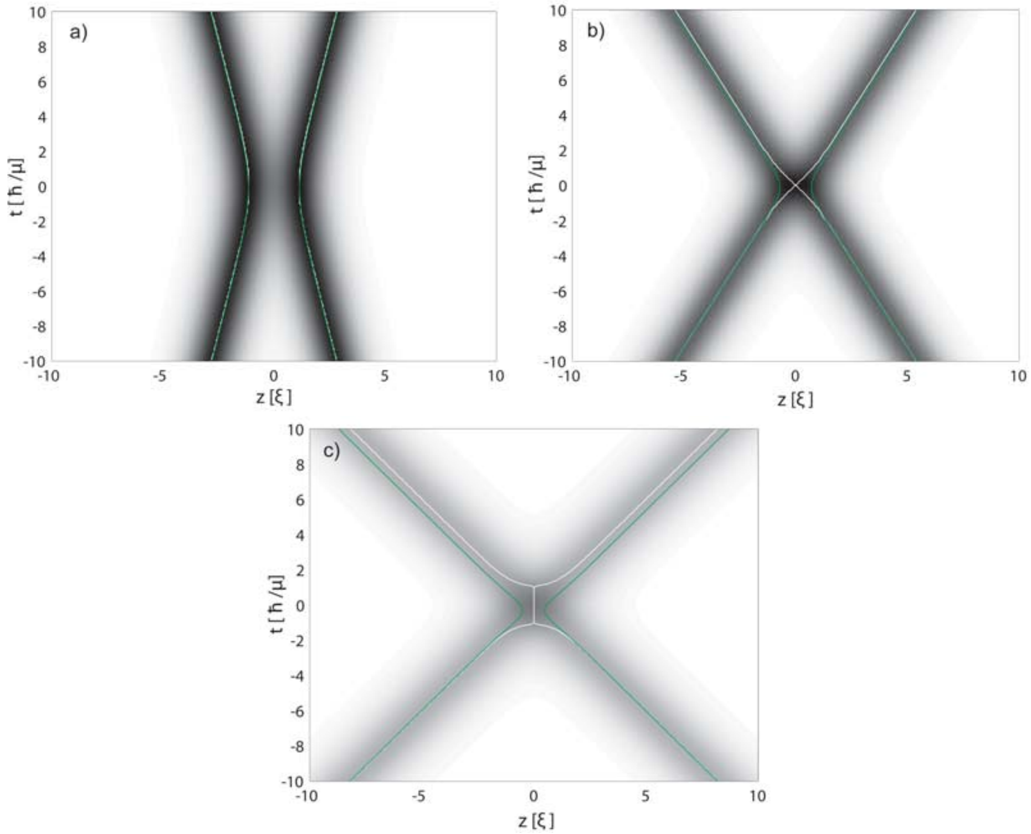

Figure 2.9: Symmetric collision of two dark solitons obtained from the analytic Eqn. 2.7, $\nu = \nu_1 = -\nu_2$. White lines: Density minima of the analytic result. Green lines: Trajectories obtained from the interaction potential approach. a) $\nu = 0.2$, the white and green lines completely overlapp. b) $\nu = 0.5$. c) $\nu = 0.8$. In b and c the green trajectories deviate from the white ones showing that the interaction approach is not a good description in this regime.

the agreement is very good pointing out the particle-like behavior of the solitons in this regime.

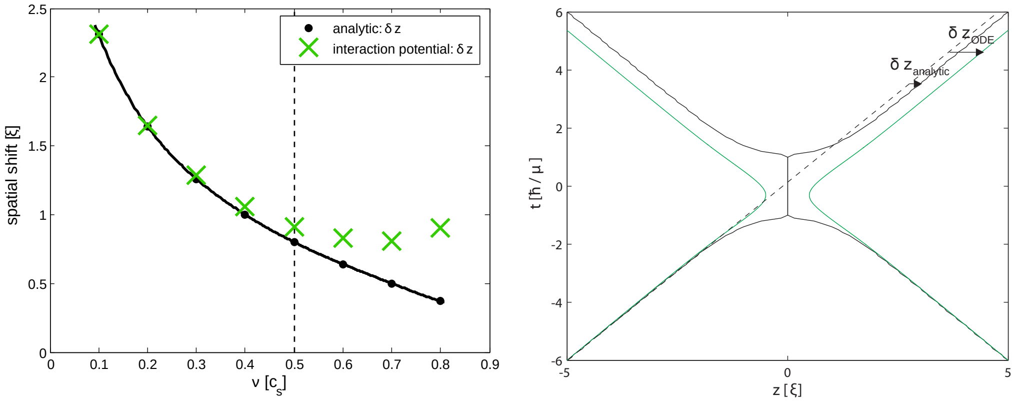

Figure 2.10: **left**: Analytically calculated spatial shifts and comparison with the shifts of the soliton trajectories obtained from the interaction potential approach. Symmetric case: $\nu = \nu_1 = -\nu_2$. The velocity $\nu = 0.5$ is marked by the dashed line. We see that for $\nu < 0.5$ both approaches agree very well. In the regime $\nu \geq 0.5$ the interaction potential cannot be applied. **right**: Illustration of the difference between the shift obtained from analytic calculation $\delta z_{analytic}$ and from the interaction potential δz_{ODE}.

Asymmetric collisions of two solitons and multiple soliton collisions

As we have seen it is possible to derive an interaction potential for the case of a symmetric collision of two dark solitons directly from the analytic two-soliton solution Eqn. 2.7. Of course Eqn. 2.7 is a very special case and more general two-soliton solutions like Eqn. 2.5 are much more complex. Therefore it has not been achieved to derive a simple interaction potential like Eqn. 2.15 from these, which would allow the calculation of the collisional trajectories of two solitons with arbitrary velocities. Based on an idea of [Kev] we establish such general potential from Eqn. 2.15 by assuming an average darkness $B_{ij} = (B_i + B_j)/2$ of the solitons and by replacing z in the symmetric case by relative coordinates $z \to (z_i - z_j)/2$. The resulting potential Eqn. 2.18 describes asymmetric collisions and even multiple soliton collisions. Of course our approach is not a formally correct derivation, but we will compare it to analytic results and numerical simulations. This will show that it gives reasonable results and has the same validity regime as Eqn. 2.15. Following our idea the potential for the $i - th$ soliton in a set of solitons reads as follows (see also [Ron2008]):

$$V_i = \sum_{j \neq i} \frac{\mu B_{ij}^2}{2m \sinh^2(B_{ij}(z_i - z_j))}, B_{ij} = \frac{B_i + B_j}{2}. \tag{2.18}$$

In the case of $\nu_1 = -\nu_2$, $z_1 = -z_2$ for $i, j = 1, 2$ Eqn. 2.18 reduces to Eqn. 2.15. Similarly to Eqn. 2.17 we can now derive equations of motion for an arbitrary number of solitons with arbitrary velocities. We get the Lagrangian $\mathfrak{L}$ and the following set of coupled Lagrangian equations for n solitons.

$$\begin{aligned}
&\mathfrak{L} = T - V = \sum_{i=1}^{n} T_i - \sum_{i=1}^{n} V_i = \sum_{i=1}^{n} \frac{\dot{z}_i^2}{2} - \sum_{i,j=1,i\neq j}^{n} \frac{\mu B_{ij}^2}{2m \sinh^2(B_{ij}(z_i - z_j)/\xi)} \\
&\frac{d}{dt}\left(\frac{\delta \mathfrak{L}}{\delta \dot{z}_i}\right) = \frac{\delta \mathfrak{L}}{\delta z_i}, i = 1, ..., n \\
&\Rightarrow \ddot{z}_i - \left(\sum_{j=1}^{n} \frac{\partial^2 V}{\partial \dot{z}^2}\ddot{z} + \sum_{j=1}^{n} \frac{\partial^2 V}{\partial z \partial \dot{z}} \frac{\partial z}{\partial t}\dot{z}_j\right) + \frac{\partial V}{\partial z} = 0, i = 1, ..., n \qquad (2.19)
\end{aligned}$$

By numerical integration of this set of equations of motion we can now in principle calculate the trajectories $z_i(t)$ of n interacting solitons.

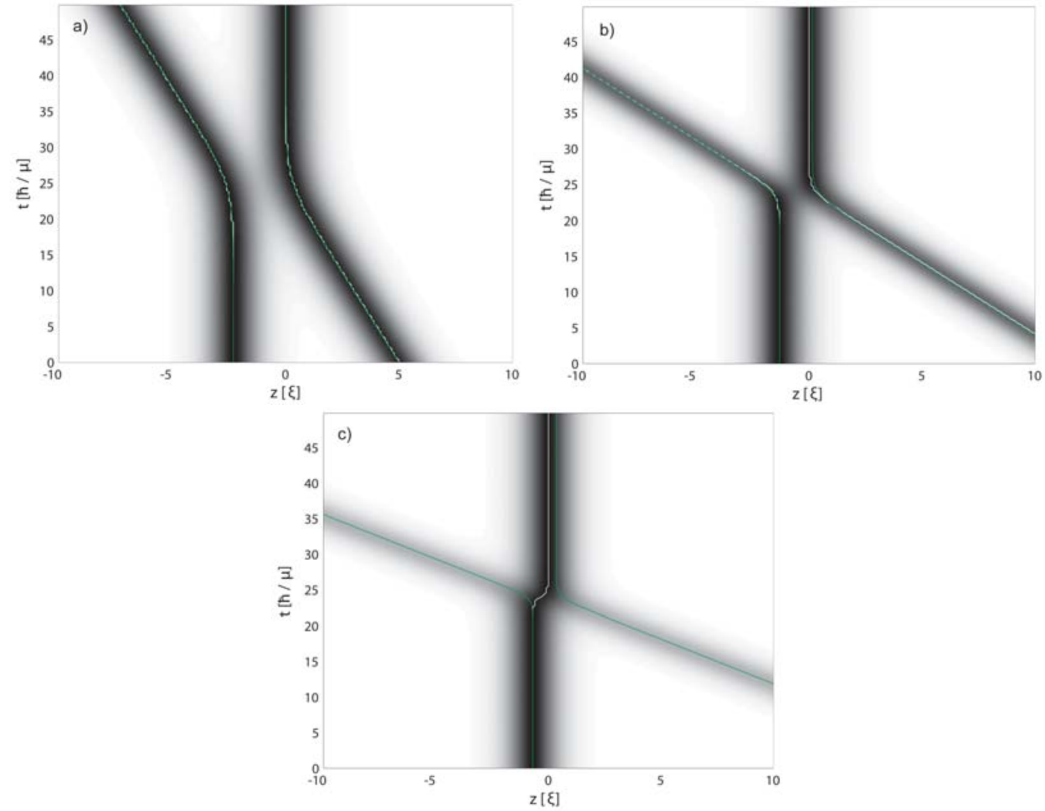

Figure 2.11: Asymmetric collision of two dark solitons obtained from the analytic Eqn. 2.5, $\nu_1 = 0$ $\nu_2 < 0$. White lines: Density minima of the analytic result. Green lines: Trajectories obtained from the interaction potential approach. a) $\nu_2 = -0.2$, the white and green lines completely overlap. b) $\nu_2 = 0.5$. c) $\nu_2 = 0.8$. In b and c the green trajectories deviate from the white ones showing that the interaction approach is not a good description in this regime. In c our fitting routine can naturally not find the weaker minimum of the faster soliton in the analytic result after the collision. Therefore we only show one white trajectory in this case.

We start with the case of an asymmetric collision $\nu_1 \neq -\nu_2$ of two solitons. Also this example we use to probe the validity regime of our approach. We exemplary regard the collision of a moving soliton $\nu_2 < 0$ with a stationary soliton $\nu_1 = 0$ for three different velocities as shown in Fig. 2.11. As one of the solitons is stationary, this case is maximally different from the symmetric case.

We plot the results obtained by the general analytic two-soliton solution Eqn. 2.5 and the trajectories calculated from Eqns. 2.19 in one figure. For the example of a slowly moving soliton $\nu_2 = -0.2$ we see that the trajectories of the interaction potential result (green lines) and the density minima of the analytic result (white lines) completely overlap. In the examples of $\nu_2 = -0.5$ and $\nu_2 = -0.8$ the two approaches deviate after the collision and especially at the collision point.

For a more systematic check we compare the analytically obtained shift of the trajectory of soliton #1, δz_1, and soliton #2, $-\delta z_2$, to their equivalent observed in the interaction potential approach for different velocities. From [Zak1973] we know that an analytic calculation reveals that the two shifts should not be equal for an asymmetric collision: $|\delta z_1| \neq |\delta z_2|$. This effect cannot be captured by our potential of Eqns. 2.18 which is, because of the assumption of an average darkness of the two solitons, symmetric in the spatial coordinate $z = (z_i - z_j)/2$. Therefore we observe for the shifts predicted by the interaction potential approach: $|\delta z_1| = |\delta z_2|$. Despite we see in Fig. 2.12 that the agreement for $-\nu_2 < 0.5$ is still good. Additionally we learn that the prediction of the interaction potential always seems to fit better to the

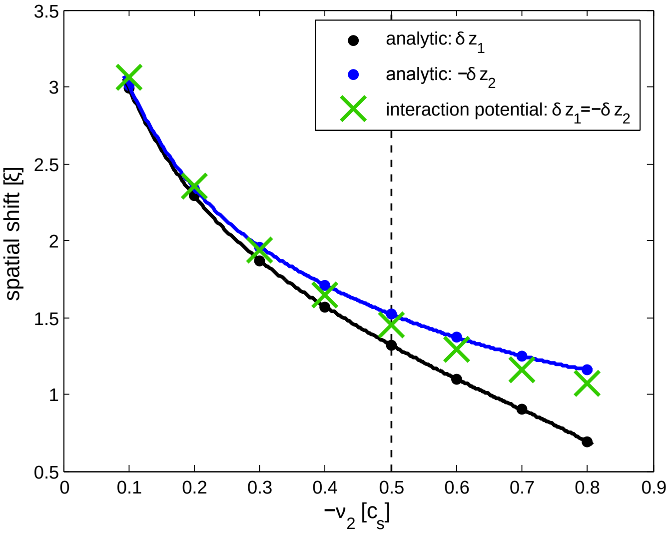

Figure 2.12: Analytically calculated spatial shifts and comparison with the shifts of the soliton trajectories obtained from the interaction potential approach. Asymmetric collision: $\nu_1 = 0$, $\nu_2 < 0$. The velocity $-\nu_2 = 0.5$ is marked by the dashed line. We see that for $-\nu_2 < 0.5$ both approaches agree quite well. In the regime $-\nu_2 \geq 0.5$ the interaction potential cannot be applied. Note one deviation: From the analytic calculations [Zak1973] it follows that the shifts of the two trajectories are not equal: $|\delta z_1| \neq |\delta z_2|$. This effect is not captured by our generalized interaction potential which results in equal shifts: $|\delta z_1| = |\delta z_2|$.

analytic prediction for the faster soliton. The agreement is even better than in the symmetric case (see Fig. 2.10). For $-\nu_2 \geq 0.5$ again larger deviations occur like in the symmetric case. It seems that the more general interaction potential of Eqn. 2.18 has approximately the same validity regime for asymmetric collisions of two solitons as the potential of Eqn. 2.15 for symmetric collisions: $\nu_i < 0.5$ for $i = 1, 2$.

In another example we observe the case of two solitons propagating with $\nu_1 = -\nu_3$ that collide with a standing soliton $\nu_2 = 0$ in the center between them. This case will be relevant for the experiment in section 4.3.1. Due to the lack of an analytic three-soliton solution we compare the trajectories obtained from the interaction potential approach with numerical simulations of the homogeneous 1D GPE equation in Fig. 2.13. We observe the three cases $\nu_1 = -\nu_3 = 0.2, 0.45, 0.55$. For $\nu_1 = -\nu_3 < 0.5$ we find a good agreement, whereas for $\nu_1 = -\nu_3 = 0.55$ the trajectories obtained from Eqns. 2.19 do not get close enough at the collision point to fit the density minima of the simulation. Also in this situation of a symmetric collision of three solitons our ad hoc approach works well for $\nu < 0.5$.

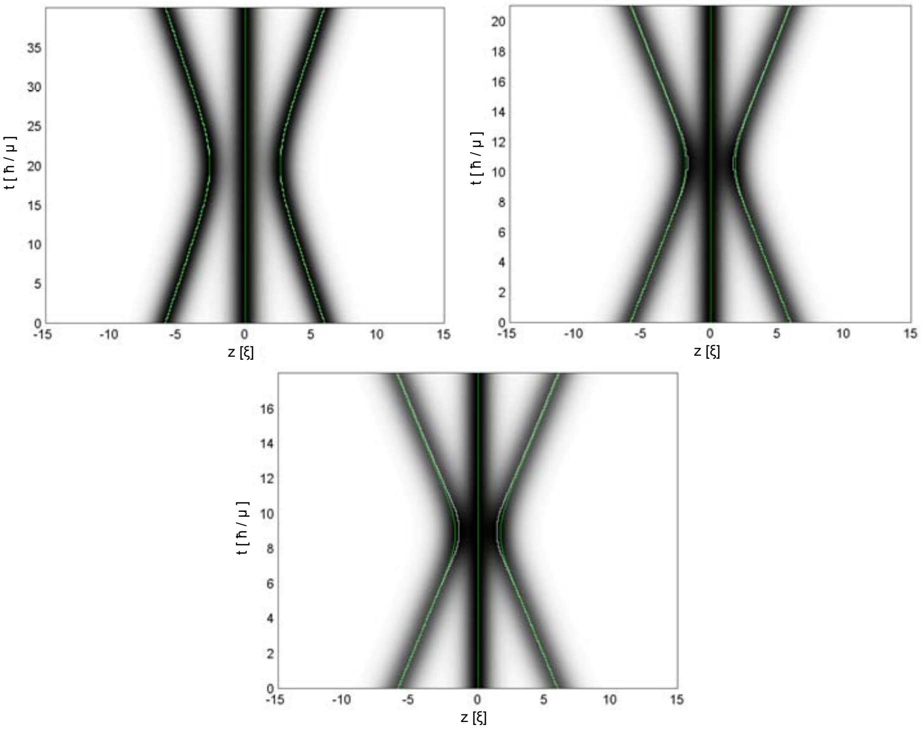

Figure 2.13: Symmetric collision of three dark solitons: $\nu_1 = -\nu_3$, $\nu_2 = 0$. Comparison of the evolution of the density profile obtained by the one-dimensional homogeneous GPE equation (density minima marked by the white lines) with the trajectories from the interaction potential approach (green lines). **top left**: $\nu_1 = -\nu_2 = 0.2$. **top right**: $\nu_1 = -\nu_2 = 0.45$. **bottom**: $\nu_1 = -\nu_2 = 0.55$. For $-\nu_2 > 0.55$ our fitting routine cannot fit the outer two density minima on the collision point properly, because the two density maxima between the three solitons vanish.

2.2 The harmonically confined crossover regime between 1D and 3D

Experiments cannot be performed in the idealized homogeneous 1D regime discussed before. But we will see in section 4.5 that stable dark solitons can be experimentally created in a regime which is referred to as the crossover regime between 1D and 3D and which is characterized by the so-called dimensionality parameter $N\Omega a_s/a_\perp \approx 1$ [Men2002]. As this regime always includes a confinement, in our case a harmonic trap, an interesting point is the investigation of the oscillation frequency of the solitons in this trap. The frequency of a dark soliton is an observable quantity which is directly accessible to the experiment and which can be influenced by various effects. In this section we will show the emergence of these effects whereas we will discuss their experimental investigation and interpretation in more detail in section 4.2.

2.2.1 Equations describing dark solitons in a non-homogeneous and non-1D regime

We have seen that a dark soliton from the theoretical point of view and strictly speaking is a solution of a homogeneous 1D nonlinear Schrödinger equation, e.g. the homogeneous 1D GPE. We will now see that also in a more 3D-like regime stable dark-soliton-like structures exist. We will not differentiate at this point and also call these structures dark solitons. Even though there is no analytic solution for dark solitons in a 3D regime they exist as stable non-dispersive density dips of a BEC in the crossover regime between 1D and 3D (see section 4.5). Regarding now a harmonically confined BEC in three dimensions the system can be in general described only by the full 3D GPE [Gro1961, Pit1961] (see appendix B):

$$i\hbar\frac{\partial}{\partial t}\Psi(\mathbf{r},t) = \left[-\frac{\hbar^2}{2m}\nabla^2 + V(\mathbf{r}) + g|\Psi(\mathbf{r},t)|^2\right]\Psi(\mathbf{r},t), \tag{2.20}$$

with the wavefunction of the condensate Ψ, the external potential V and the constant of atomic interaction $g = 4\pi\hbar^2 a_s/m$. For special cases, e.g. highly elongated BECs which are not transversally excited, the description is also possible by effective 1D equations. In these cases the transverse motion ($\sim \omega_\perp^{-1}$) is fast compared to the time scale of the axial motion ($\sim \omega_z^{-1}$) meaning that the transverse degrees of freedom adjust instantaneously to the lowest energy configuration (adiabatic approximation) [Mat2008]. This implies that the axial and transverse motion can be treated independently so that the wavefunction can be factorized as:

$$\Psi(\mathbf{r},t) = \varphi(r_\perp, n_z(z,t))\Phi(z,t), \tag{2.21}$$

with the axial density $n_z(z,t) = |\Phi(z,t)|^2$. In the derivation of the effective 1D equations axial and time variations of φ induced by the axial density $n_z(z,t)$ are neglected. Neglecting $(\partial/\partial t)\varphi$ requires the above discussed adiabatic approximation and neglecting $(\partial^2/\partial z^2)\varphi$ requires the axial density to vary sufficiently slowly

[Mat2008]. An example for such equation is the nonpolynomial Schrödinger equation (NPSE) derived by Salasnich et al. [Sal2002]:

$$\begin{aligned} i\hbar\frac{\partial}{\partial t}\Phi = \big[-\frac{\hbar^2}{2m}\frac{\partial^2}{\partial z^2} + V_z(z) + \frac{gN}{2\pi a_\perp^2}\frac{|\Phi|^2}{\sqrt{1+2a_sN|\Phi|^2}} + \\ \frac{\hbar\omega_\perp}{2}\left(\frac{1}{\sqrt{1+2a_sN|\Phi|^2}} + \sqrt{1+2a_sN|\Phi|^2}\right)\big],\Phi \end{aligned} \tag{2.22}$$

with $\omega_\perp = 2\pi\nu_\perp$ the transverse trap frequency. It has been shown by [The2007] that this equation is a very good approximation for the description of dark solitons in the crossover regime between 1D and 3D. The disadvantage of this equation is that properties of the condensate like the healing length ξ and the chemical potential μ cannot be calculated correctly from it. The results always vary significantly from the 3D GPE result.

A new approach of Muñoz Mateo and Delgado results in an equally accurate but simpler effective 1D equation [Mat2008]:

$$i\hbar\frac{\partial\Phi}{\partial t} = -\frac{\hbar^2}{2m}\frac{\partial^2\Phi}{\partial z^2} + V_z(z)\Phi + \hbar\omega_\perp\sqrt{1+4a_sN|\Phi|^2}\Phi. \tag{2.23}$$

Analytic equations can be obtained from the Muñoz Mateo-Delgado equation (MDE) which allow the direct calculation of μ and ξ and the density $n(z)$ [Mat2009]. For the parameters of our experiment in section 4.2 the results differ only by 1% from the ones obtained by numerical integration of the 3D GPE.

If $a_s n_z \ll 1$ the effective 1D equations reduce to the 1D GPE [Mat2008]:

$$i\hbar\frac{\partial\Phi}{\partial t} = -\frac{\hbar^2}{2m}\frac{\partial^2\Phi}{\partial z^2} + V_z(z)\Phi + g_{1D}N|\Phi|^2\Phi, \tag{2.24}$$

with $g_{1D} = 2a_s\hbar\omega_\perp$ the constant of one dimensional atomic interaction. If even $V_z(z) = 0$ the effective 1D equations transform into the homogeneous 1D GPE.

2.2.2 Numerical simulations

To investigate the dynamics of dark solitons in a harmonic trap it is necessary to perform numerical simulations as no analytic solutions exist.

We perform two kind of simulations which differ in the creation process of the solitons:

a) **Initialized-soliton (IS) simulations.** [3] These simulations are based on two steps. At first the solitons are obtained in the following way. We calculate

---

[3] We will use the term NPSE-IS simulations for initialized-soliton simulations using the NPSE.

the ground state of the BEC and the first excited state in the requested harmonic trap using the split step fourier transform method [Fei1982, Vri1986] in imaginary-time propagation. As a standing dark soliton is the first fundamental excitation of a harmonically trapped BEC (its analog in a linear regime would be the first excited state of the harmonic oscillator) we extract the pure soliton by dividing the first excited state by the ground state. In the second step we initialize one or more dark solitons at desired positions in the BEC and let them numerically evolve using the same method as before but now in real-time propagation. As this kind of simulation does not involve transversal excitations of the BEC it is sufficient to use one of the effective 1D equations here (see Fig. 2.14 and section 2.2.1). The effective 1D equations are much less time consuming in simulations.

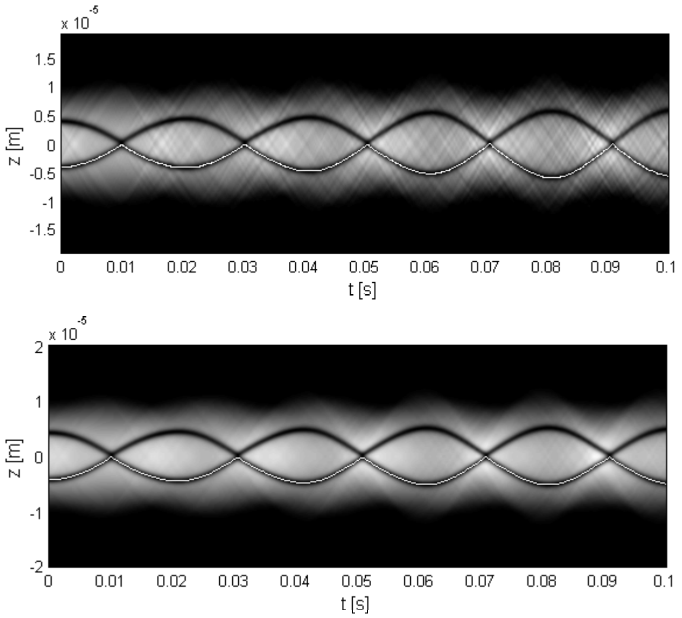

Figure 2.14: **top**: Two soliton IS simulation using the 3D GPE resulting in $\nu_d = 0.744$. **bottom**: Two soliton IS simulation using the NPSE resulting in $\nu_d = 0.751$. The path of the density minimum of one of the solitons is shown by the white lines. For the parameter sets of our measurements (see section 4.2) we checked the difference of the oscillation frequency obtained by numerical simulations using the NPSE from the 3D GPE result. For the mean deviation of $\nu_{3DGPE} - \nu_{NPSE}$ we get $\Delta(\nu_{3DGPE} - \nu_{NPSE}) = 1\% \pm 0.6\%$. Parameters: Set #4 of tables 4.1 and 4.2.

b) Simulations including the preparation process. In these kind of simulations we include the full creation process of the solitons in our experiments as described in section 3.3. As we merge two atom clouds in this process transverse excitations of the BEC might occur. Therefore it is more accurate to perform a full 3D GPE simulation for reconstructing the exact time evolution in this case. Even though the effective 1D equations still give acceptable agreement with the

3D GPE results for short enough evolution times, details of the dynamics can differ (see Fig. 2.15).

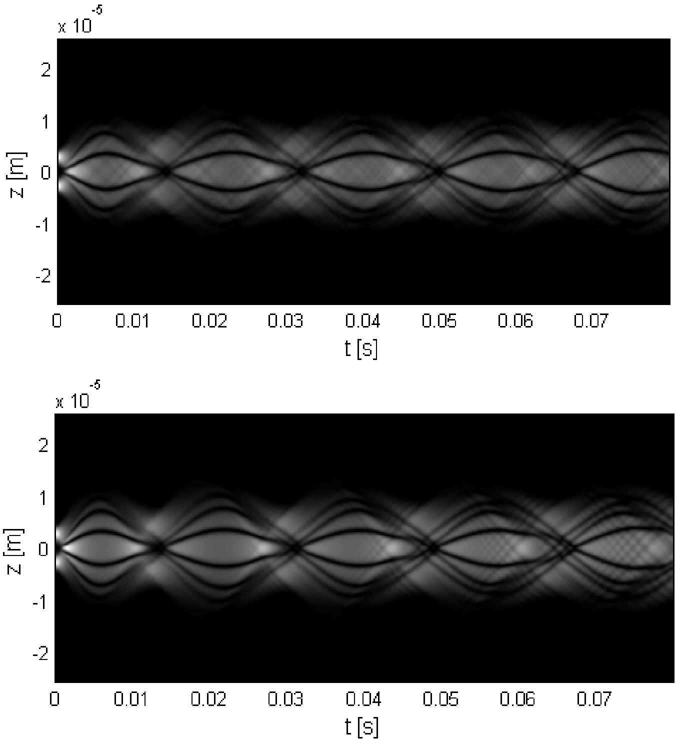

Figure 2.15: Comparison of simulations taking the creation process (see section 3.3) of the solitons into account using the 3D GPE (**top**) and the NPSE (**bottom**). Note that an effective 1D equation like the NPSE is especially not a very good approximation for the initial state of the creation process. In this double well potential the BEC in each of the wells has rather a three-dimensional character than a one-dimensional one. According to this fact we have to adjust the barrier height of the initial optical lattice to get a similar result for the simulations of both equations: $V^0_{3DGPE} = 1500\,\mathrm{HZ}$ and $V^0_{NPSE} = 1250\,\mathrm{HZ}$. Parameters: $N = 2000$, $\nu_\perp = 408\,\mathrm{Hz}$, $\nu_z = 37\,\mathrm{Hz}$, $t_{\nu_z} = 10\,\mathrm{ms}$ and $t_{SW} = 0.5\,\mathrm{ms}$, with t_{ν_z} the ramping times of the longitudinal trap frequency and t_{SW} the ramping time of the optical lattice.

By determining the path of the density minima of the solitons in the simulations and afterwards fitting we can extract the oscillation frequencies of the solitons from the simulations. In the single soliton case the fit is performed with a sin-function, whereas we use the absolute value of a sin for the two soliton case. The obtained frequencies in the two soliton case are divided by two in order to compare them to the oscillation frequencies of single trapped solitons.

2.3 Dark solitons in the crossover regime between 1D and 3D

Due to the lack of an analytic solution in the crossover regime we have to perform numerical simulations of the 3D GPE or one of the effective 1D equations to learn about the dynamics of dark solitons in this regime. We have performed extensive studies using the NPSE, and also the MDE, to investigate the effects which can influence the oscillation frequencies of dark solitons in harmonically trapped BECs. The outcome of our NPSE-IS simulations and their agreement with the interaction potential approach (see section 2.1.6) will be discussed in the following two sections (2.4 and 2.5).

2.4 A single dark soliton in a harmonically confined BEC

Busch and Anglin [Bus2000] (see section 4.2) have shown that a dark soliton in a harmonically confined BEC in the Thomas-Fermi 1D regime (see section 4.2 and [Men2002]) can be described by an equation of motion in a particle-like manner (see Fig 2.16):

$$\ddot{z} + \frac{\omega_z^2}{2} z = 0. \tag{2.25}$$

This implies that the soliton should oscillate (see Fig. 2.18) slower than the trap

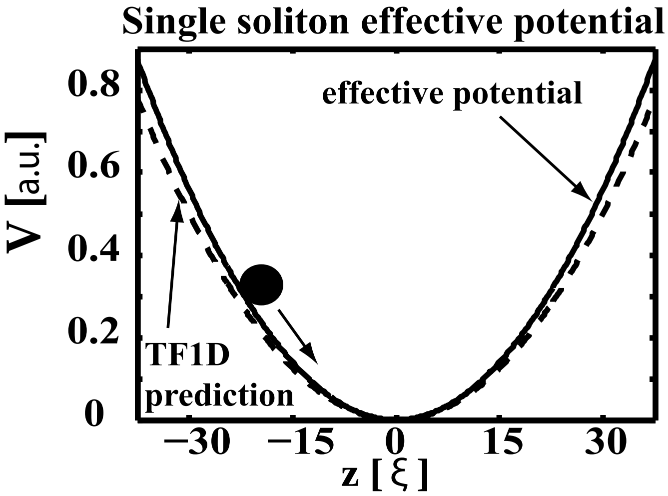

Figure 2.16: A dark soliton in a harmonically trapped BEC can be modeled by a classical particle oscillating in an effective potential with frequency ν_d and $\nu_z > \nu_d > \nu_z/\sqrt{2}$. In the idealized 1D-TF regime the effective potential exhibits the frequency $\nu_z/\sqrt{2}$, shown by the dashed line.

frequency with $\nu_d^{1D} = \nu_z/\sqrt{2}$. Muryshev et al. have reproduced this result using a Bogoliubov-de-Gennes analysis [Mur1999]. Besides Fedichev et al. demonstrated that in the homogeneous 1D regime, adding a harmonic trap decreases the energy of a dark soliton by the term $-M\omega_z^2 z^2/4$ [Fed1999]. The ratio of the soliton mass $-M$ over this potential energy of the soliton gives: $1/(\omega_z^2 z^2/4)$, which is exactly two times the ratio of the atomic mass m over the external potential: $1/(\omega_z^2 z^2/2)$. In this sense a dark soliton can be regarded as a particle with a negative mass of $-2m \cdot N_d$ [Bra2006, Bec2008, Fed1999], with N_d the number of atoms repelled out of the soliton notch[4]. Since the prediction of Busch and Anglin is derived for the Thomas-Fermi 1D regime characterized by $N\Omega a_s/a_\perp \ll 1$ and $((N/\sqrt{\Omega})a_s/a_\perp)^{1/3} \gg 1$ it is also interesting to observe other regimes closer to experiments and look for deviations from this result.

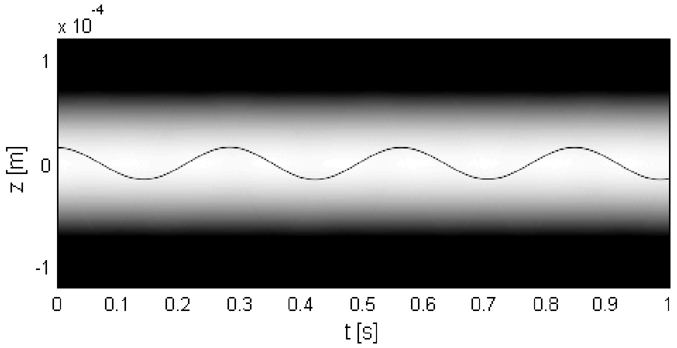

Figure 2.17: Exemplary simulation of a dark soliton oscillating in a harmonically trapped BEC in the 1D Thomas-Fermi regime using the NPSE. For the oscillation frequency of the soliton we get $\nu_d = 0.712$ in this case of $N\Omega a_s/a_\perp = 0.001$ and $((N/\sqrt{\Omega})a_s/a_\perp)^{1/3} = 17.3$. In contrast to simulations of the 1D GPE where the oscillation frequency of a dark solitons always (independently of Ω) tends toward the value of $\nu_d^{1D} = \nu_z/\sqrt{2}$ for $N\Omega a_s/a_\perp \to \infty$, one has to choose extremely small values of Ω to observe this result in a more adequate effective 1D or 3D simulation (see Fig. 2.19). Parameters: $N = 1000$, $\nu_\perp = 5000\,\mathrm{Hz}$ and $\nu_z = 5\,\mathrm{Hz}$.

Theocharis et al. [The2007] have investigated the oscillation frequencies of single dark solitons in a harmonic trap in the crossover regime between 1D and 3D by numerical studies using the 3D GPE and the NPSE. Additionally they perform a Bogoliubov-de-Gennes analysis of the NPSE and 1D GPE model, which reveals the different eigenfrequencies of the system. They show that one of the frequencies obtained by the Bogoliubov-de-Gennes analysis of the NPSE, the so called anomalous mode, coincidences with the soliton oscillation frequency. By performing the analysis for a multitude of values of the dimensionality parameter $N\Omega a_s/a_\perp$ (see section 3.4) they obtain curves which show the dependence of the oscillation frequency on this parameter.

---

[4] Fedichev et al. [Fed1999] have shown, that the number of atoms missing at the soliton notch can be calculated as $N_d = nS \cdot 2\xi$, with n the background density, S the transverse cross section of the condensate and ξ the healing length.

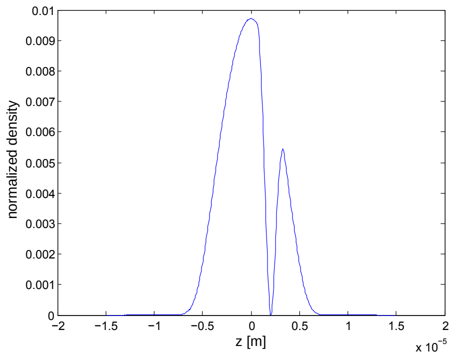

Figure 2.18: Oscillation of a dark soliton in a harmonically trapped BEC. If a dark soliton is created away from the trap center it will gain velocity and start to oscillate. As the darkness of the soliton is connected to its speed, its speed is highest on positions close to the trap center (**right**) and zero on the turning point (**left**).

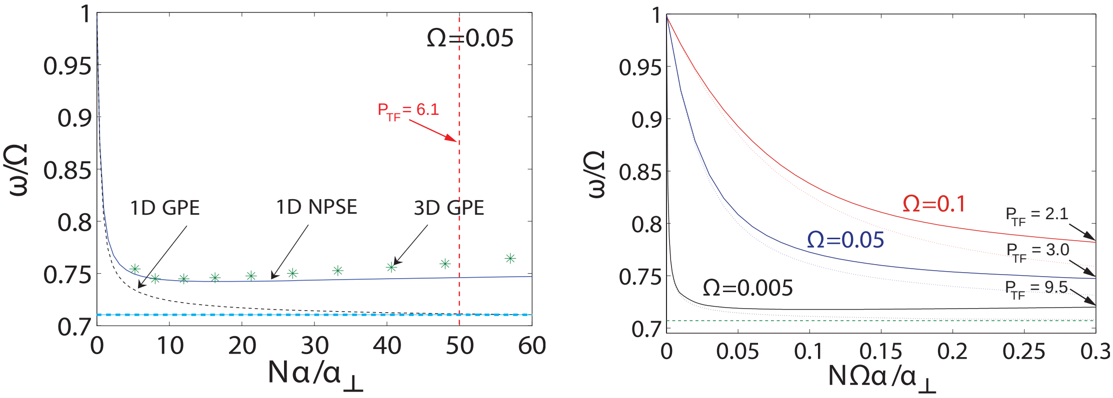

Figure 2.19: Oscillation frequencies of single dark solitons in the crossover regime between 1D and 3D obtained by Bogoliubov-de-Gennes analysis by [The2007]. **left**: Oscillation frequency vs. $N\Omega a_s/a_\perp$ for the case of $\Omega = 0.05$. blue dashed line: 1D-TF prediction, dashed black line: 1D GPE result, black solid line: NPSE result, green stars: 3D GPE simulation. For $(N/\sqrt{\Omega}a_s/a_\perp)^{1/3} \gg 1$ the 1D GPE result is expected to match $\nu_d^{1D} = \nu_z/\sqrt{2}$. The red dashed line marks the value $P_{TF} = (N/\sqrt{\Omega}a_s/a_\perp)^{1/3} = 6.1$. **right**: Comparison for three different values of Ω. The NPSE result, in contrast to the 1D GPE result, only tends towards $\nu_d^{1D} = \nu_z/\sqrt{2}$ for extremely small values of Ω. The green dashed line marks the 1D-TF prediction. Note that $N\Omega a_s/a_\perp \gg 0$ when the 1D GPE result matches ν_d^{1D} for large values of Ω. This is out of the validity regime of the 1D GPE. Note that the oscillation frequency is given in units of $[\Omega] = [\nu_z/\nu_\perp]$ here. Figures taken from [The2007] and adapted.

They find out that the oscillation frequency of a dark soliton in the observed regime can differ on the order of 10% from the asymptotic prediction $\nu_d^{1D} = \nu_z/\sqrt{2}$. One of their main results is shown in Fig. 2.19 where the behavior of the oscillation frequency $\omega_d = 2\pi\nu_d$ is plotted for different aspect ratios of the trap $\Omega = \omega_z/\omega_\perp$. Firstly, we see that for small values of the dimensionality parameter $N\Omega a_s/a_\perp$ the frequency tends

towards the trapping frequency ω_z ($\omega_z/\omega_\perp$ in the units of Fig. 2.19). This behavior is expected, because when the dimensionality parameter is decreased the density of the gas gets lower and lower until the nonlinear interaction term no longer dominates the Gross-Pitaevskii equation. On that point one enters the linear regime.
More interesting is the behavior of the frequency towards large values of $N\Omega a_s/a_\perp$. As we see the 1D GPE simulations predict that ω_d should always go down to the asymptotic value of $\nu_d^{1D} = \nu_z/\sqrt{2}$ when the TF-limit is reached, like also observed in [Bus2000]. But the 1D GPE is not a sufficient equation for the regarded regime as it cannot capture the effects of dimensionality of the system. This is emphasized by the NPSE and 3D GPE simulations, which for the shown values of Ω never go completely down to $\nu_d^{1D} = \nu_z/\sqrt{2}$. This means that in the crossover regime between 1D and 3D the frequency of a single dark soliton in a harmonically trapped BEC is always $\nu_d > \nu_z/\sqrt{2}$. We will refer to this effect as the dimensionality effect. Theocharis et al. have also shown, that an effective 1D equation like the NPSE is a very good approximation to the 3D GPE for the observation of dark solitons in the crossover regime between 1D and 3D. Exemplary Fig. 2.21 shows a numerical simulation of a dark soliton in the crossover regime between 1D and 3D oscillating with a frequency $\nu_d = 0.757\nu_z \neq \nu_d^{1D}$.

In addition to the work of Theocharis et al. [The2007] we have performed a multitude of NPSE simulations of a dark soliton in a harmonically trapped BEC for different oscillation amplitudes. Fig. 2.20 shows that the dependence of the soliton oscillation frequency on the oscillation amplitude is small.

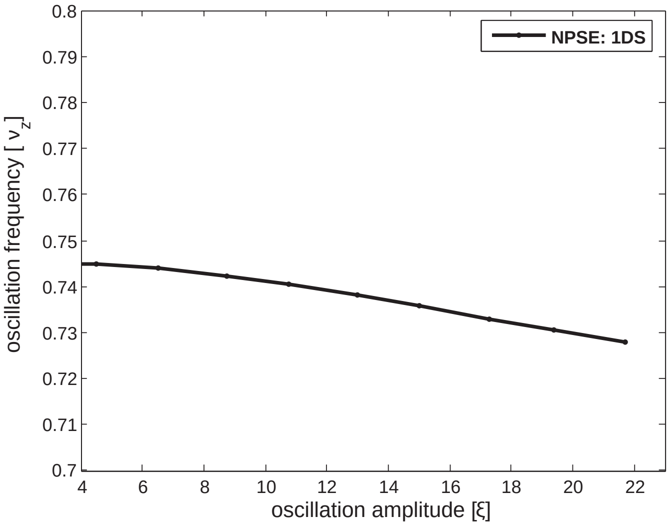

Figure 2.20: Frequency dependence of a single dark soliton on the oscillation amplitude obtained by NPSE-IS simulations. Parameters: $N = 1000$, $\nu_z = 50\,\mathrm{Hz}$ and $\nu_\perp = 500\,\mathrm{Hz}$.

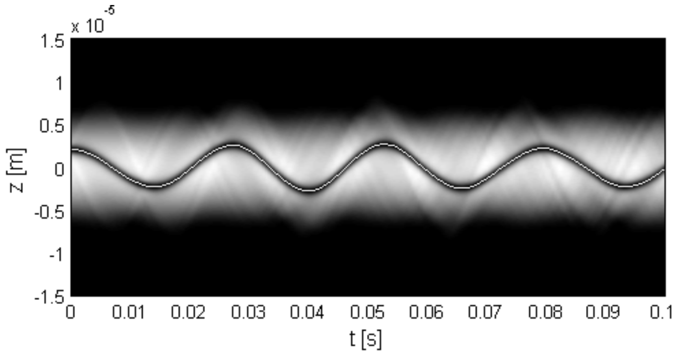

Figure 2.21: Oscillation of a single dark soliton in the crossover regime using the NPSE, $\nu_d = 0.757\nu_z$. Parameters: $N = 1000$, $\nu_z = 50\,\mathrm{Hz}$, $\nu_\perp = 500\,\mathrm{Hz}$ and initial displacement from trap center: $2\,\mu\mathrm{m}$. The path of the density minimum is marked by the white line.

2.5 Multiple dark solitons in a harmonically confined BEC

Up to now we have only considered single solitons in a harmonically trapped BEC. Since we have seen in section 2.1.6 dark solitons exhibit a mutual interaction. It is therefore interesting to find out how this interaction affects the oscillation of solitons in a harmonic trap.

In this section we will investigate NPSE simulations for the case of two and three solitons symmetrically oscillating in a harmonically confined BEC. Both cases are relevant for our experiments described in section 4.2. We will also extend our interaction potential approach to this regime and compare its results with numerical simulations.

2.5.1 The effective potential approach for the crossover regime

It is possible to include the soliton interaction potential discussed in section 2.1.6 together with a potential taking the harmonic confinement plus the dimensionality effect into account in an effective soliton potential. Again we make an ad hoc approach here which we do not derive formally. But as we will see our approach fits the numerical multi soliton IS simulations very well and can therefore be justified afterwards. We assume the effective soliton potential for the symmetric two soliton collision to be described by the following potential:

$$\begin{aligned} V_{eff}(z,\dot{z}) &= V_{interaction}(z,\dot{z}) + V_{eff\,trap}(z) \\ V_{eff}(z,\dot{z}) &= (2\pi\nu_{1S})^2\frac{z^2}{2} + \frac{\mu B^2}{2m\sinh^2(2Bz/\xi)}, \end{aligned} \qquad (2.26)$$

where ν_{1S} is the oscillation frequency of a single dark soliton in the regarded harmonic trap. Due to the dimensionality effect (see section 2.4) this frequency always lies in the range: $\nu_z/\sqrt{2} < \nu_{1S} < \nu_z$, with ν_z the longitudinal trap frequency. Therefore the first term on the right hand side describes the effective harmonic potential for the soliton including the dimensionality of the system. The second term is the inter-soliton interaction potential derived for the homogeneous 1D regime as suggested by [Kiv1995][5]. We set the interaction constant μ to be the chemical potential obtained from the 3D GPE and the darkness of the soliton to $B = \sqrt{1 - \dot{z}^2/c_s^2}$, with $c_s = \sqrt{\mu/m}$ the Bogoliubov speed of sound. From the potential of Eqn. 2.26 we can derive a Lagrange equation of motion for two symmetrically colliding dark solitons in a harmonic trap, as described in section 2.1.6.[6]

As also described in section 2.1.6 we can again generalize Eqn. 2.26 to the case of asymmetric collisions in a harmonic trap. Then the effective potential takes the form:

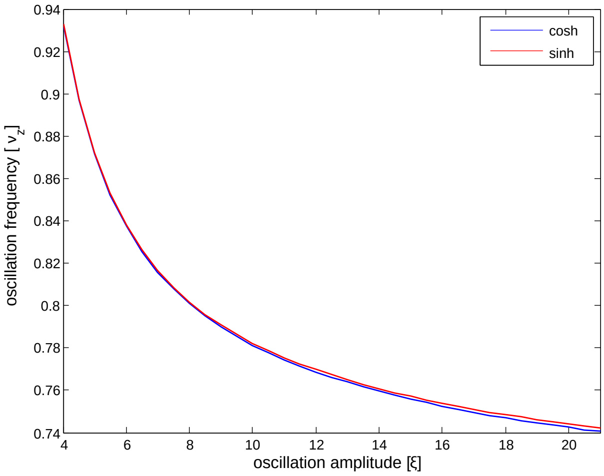

Figure 2.22: Comparison of the soliton oscillation frequencies obtained from Eqn. 2.26 to the ones obtained from a similar potential where the sinh function has been replaced by cosh. red curve: sinh case, blue curve: cosh case.

$$V_i^{eff} = (2\pi\nu_{1S})^2 \frac{z_i^2}{2} + \sum_{j \neq i} \frac{\mu B_{ij}^2}{2m \sinh^2(2B_{ij}(z_i - z_j)/\xi)}, \tag{2.27}$$

with z_i and z_j the positions and $B_{ij} = (B_1 + B_j)/2$ the average darkness of two colliding solitons. From the Lagrangian $\mathfrak{L} = \sum_{i=1}^n \dot{z_i}^2/2 - \sum_{i=1}^n V_i^{eff}$ we can now in principle derive the equations of motion for an arbitrary number of colliding solitons in a harmonic trap. As an example we show the collisions and oscillations of three solitons in Fig. 2.23.

---

[5] Note that the potential shown here differs from the one shown in [Kiv1995] and used in [Wel2008] as it contains a sinh instead of a cosh. [Kev] found out while reconstructing the derivation of Eqn. 2.15, that the sinh is the formally correct function here. This was confirmed by W. Krolikowski, one of the authors of [Kiv1995]. But as the derivation of Eqn. 2.15 explicitly assumes that the potential is valid when the two solitons do not overlap, only the asymptotic behavior of the function is important which is the same for sinh and cosh. In this validity regime of Eqn. 2.15 no significant

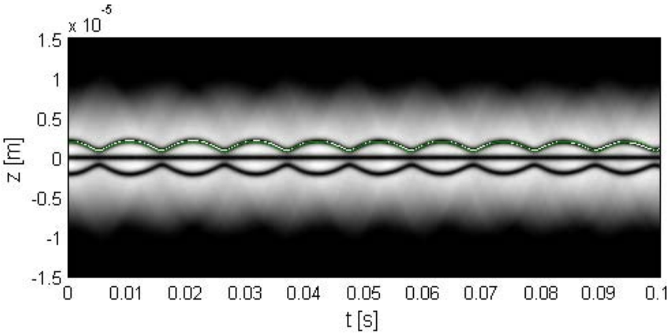

Figure 2.23: Oscillation of three dark solitons in the crossover regime, $\nu_d = 0.904\nu_z$. The path of the density minimum of one of the solitons is marked by the white line. For the same soliton we also give the trajectory obtained from the effective potential approach of Eqn. 2.27 as the green line. Both results nearly overlap. Parameters: $N = 2000$, $\nu_z = 53\,\mathrm{Hz}$, $\nu_\perp = 890\,\mathrm{Hz}$ and initial displacement from trap center: $2\,\mu\mathrm{m}$.

2.5.2 Two dark solitons in a harmonically confined BEC

To illustrate the behavior of the frequency of two dark solitons symmetrically oscillating ($v_1 = -v_2$) in a harmonic trap we perform a multitude of IS simulations (see section 2.2.2) of the NPSE for different oscillation amplitudes, or in other words different mean distances between the solitons. We see in Fig. 2.25 that the oscillation frequency in the two soliton case is always higher than for a single soliton (see Fig. 2.20) and is strongly depending on the oscillation amplitude. An example of such simulation is shown in Fig.2.24. Additionally we plot in Fig. 2.25 the

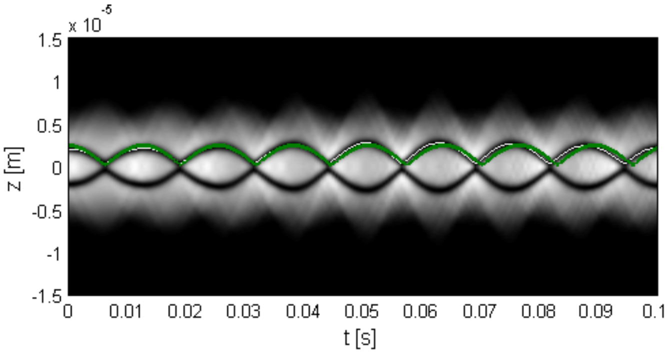

Figure 2.24: Oscillation of two dark solitons in the crossover regime using the NPSE, $\nu_d = 0.797\nu_z$. The path of one density minimum is marked by the white line. The green line shows the trajectory obtained by the effective potential approach for the same soliton. Parameters: $N = 1000$, $\nu_z = 50\,\mathrm{Hz}$, $\nu_\perp = 500\,\mathrm{Hz}$ and initial displacement from trap center: $2\,\mu\mathrm{m}$.

---

deviation occurs if cosh is changed to sinh.

[6] Fig. 2.22 shows that changing the sinh function in Eqn. 2.26 to cosh does not influence the oscillation frequency of the solitons significantly.

oscillation frequencies as obtained from the differential equation (ODE) stemming from the effective potential approach of Eqn. 2.26. Wee see that the simulation- and effective-potential results are in good agreement. A more detailed interpretation of these results will be discussed in section 4.2, where we will discuss our experiments performed in this context.

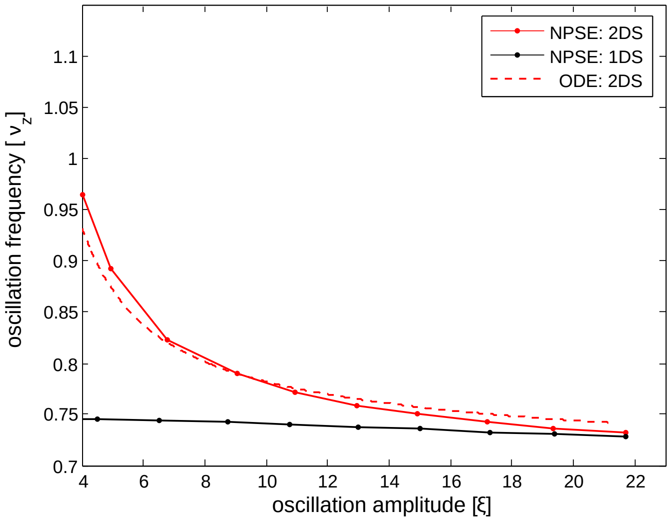

Figure 2.25: Frequency dependence of two dark solitons on the oscillation amplitude and comparison to the single soliton case. Bold curves: NPSE-IS simulations. Dashed curve: Effective potential approach. Parameters: $N = 1000$, $\nu_z = 50\,\mathrm{Hz}$ and $\nu_\perp = 500\,\mathrm{Hz}$.

2.5.3 Three dark solitons in a harmonically confined BEC

In the case of three symmetrically oscillating ($v_1 = -v_3, v_2 = 0$) dark solitons the oscillation frequency is even more upshifted from the single soliton results as in the case of two solitons, see Fig. 2.26. Again the agreement with the effective potential approach of Eqn. 2.27 is good. The symmetric three soliton oscillation in a harmonically trapped BEC is exemplified in Fig. 2.23. For comparison we additionally plot the trajectories expected from the effective potential approach in this figure. We again leave the further interpretation to chapter 4.

In conclusion, in this chapter we have discussed the basic features of dark solitons and of their mutual interaction. We have combined an interaction potential for dark solitons derived in the 1D homogeneous regime with a harmonic potential taking the effective soliton frequency due to the role of dimensionality into account. We have shown that the resulting effective potential can describe the essentials of the soliton dynamics of a harmonically trapped BEC in the crossover regime between 1D and 3D. Furthermore, we have seen that in the case of multiple harmonically trapped solitons, the oscillation frequencies strongly depend on the mean distance between

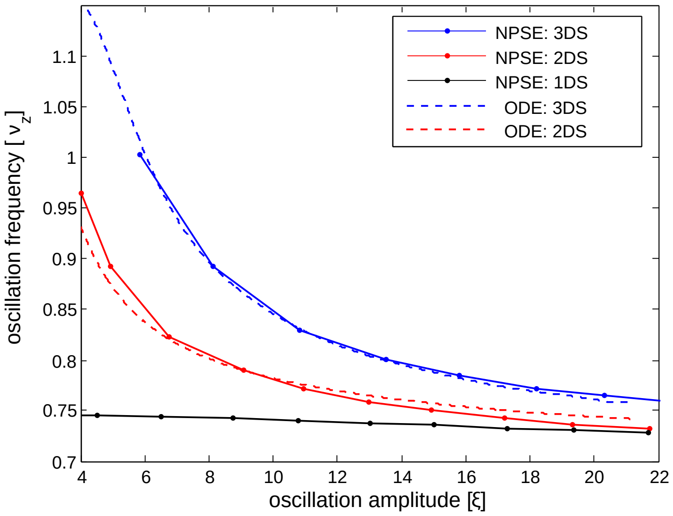

Figure 2.26: Frequency dependence of three dark solitons on the oscillation amplitude and comparison to the single- and two-soliton case. Bold curves: NPSE-IS simulations. Dashed curves: Effective potential approach. Parameters: $N = 1000$, $\nu_z = 50\,\mathrm{Hz}$ and $\nu_\perp = 500\,\mathrm{Hz}$.

the solitons. This opens the way to a new possibility of detecting the interaction between dark solitons experimentally and will be very important for our experiments discussed in section 4.2.

Chapter 3

Experimental observation of dark solitons in Bose-Einstein Condensates

We start this chapter with a short summary of the history of dark solitons in BECs. Then the two main methods, including our method, for the creation of dark solitons in BECs will be presented. Furthermore, we will discuss in which regime the solitons should be created experimentally.

3.1 History of dark solitons in BECs

Dark solitons in BECs have been created for the first time by Burger et al. [Bur1999] and Denschlag et al. [Den2000]. These experiments showed, that dark solitons can move through a BEC. Yet the solitons were so short-lived that solely their translation and not their oscillation in the harmonically trapped BEC could be observed. Theoretical works discovered, that this instability was due to the 3D character of the trap and the corresponding dimensionality regime. The trap was either chosen to produce a nearly spherical BEC or a cigar-shaped BEC with too high number of atoms. The dimensionality parameter (see section 3.4) in these experiments was $N\omega\frac{a_s}{a_\perp} \gg 1$ which characterizes the genuine 3D regime. Solitons, which are in principle one-dimensional objects, created in such regime, get bent, fill up from the side and finally decay into two vortex rings. This is the so called 'snaking instability' [Mur1999] (see section 4.5.1), which was revealed experimentally by Anderson et al. [And2001]. The interesting predictions of Busch and Anglin [Bus2000] and Theocharis et al. [The2007] (see section 2.4) that dark solitons in harmonically trapped BECs should not oscillate with the trap frequency but slower than this, could not be observed, because of the short lifetime of the solitons.

Most of these experiments used the so called phase imprinting method (see section 3.2.1) for the creation of dark solitons. Later additional methods have been explored like dragging a laser beam through a condensate [Eng2007] or using a compressed pulse of slow light to create a defect which evolves into dark solitons [Dut2001].

Very recently it has become possible to overcome the snaking instability by creating dark solitons in cigar-shaped condensates in the crossover regime between 1D and 3D where they are stable. A single oscillation of one dark soliton [Bec2008], a single collision between two dark solitons [Ste2008] and multiple oscillations and collisions of two dark solitons in a harmonically trapped BEC [Wel2008] have been reported. Also a periodic transition between a soliton and a vortex ring has been observed [Sho2008]. In the experiments of [Sho2008] and in our experiments [Wel2008] the solitons were created by means of matter wave interference (see section 3.2.2) after merging two condensates initially prepared in a double well potential. As we will show in this section our experiments reveal the predicted frequency reduction for the oscillation of dark solitons in a harmonically trapped BEC and the repulsive interaction between them. This interaction is observed as an increase of the oscillation frequency with decreasing amplitude of the distance between the solitons during their oscillation.

3.2 Methods of creating dark solitons in BECs

Among the many methods of creating dark solitons in a BEC, two offer the possibility to create solitons with shot-to-shot reproducibility. The first one is the so-called phase imprinting method, which was the first method to produce dark solitons. The second one is the method of matter wave interference also referred to as density engineering, which is used in our experiments. In the following we will describe these two methods in more detail.

3.2.1 The phase imprinting method

Since a dark soliton is connected to a phase jump $\Delta\phi \leq \pi$, imprinting this structure onto the wavefunction of a BEC by means of a light field will lead to the creation of a soliton. The needed intensity profile $I(z)$ must correspond to a step function with a width of its edge close to the width of the soliton [Bur2002] (see Fig. 3.1). A possible experimental realization consists in shining a laser pulse onto the edge of a razor blade.

Such potential takes the form $U(z) = (\hbar\Gamma^2/8\delta)[I(z)/I_0]$ [Den2000] (see also section 5.2.1) corresponding to a phase of $\phi(z) = U(z)\tau/\hbar$ with Γ the transition line width, I_0 the saturation intensity, δ the detuning of the laser beam from the atomic resonance and τ the duration of the laser pulse. The laser pulse must be applied for a duration shorter than the correlation time of the condensate $\tau_{cor} = \hbar/\mu$, with the chemical potential μ, so that the wavefunction acquires the local phase factor $exp(-i\phi)$ without changing its density profile. A formula for estimating the imprinted phase is given in [Bur2002]

$$\phi(z) = \frac{\Delta\phi}{2}\left(1 + \tanh\left[\frac{z - z_0}{0.45 l_e}\right]\right) \tag{3.1}$$

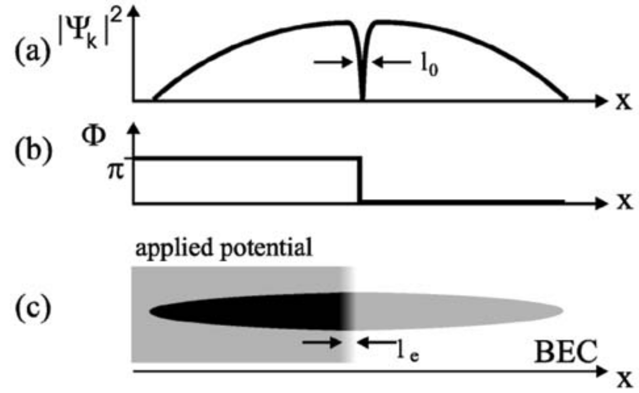

Figure 3.1: a) Density profile of a BEC including an ideal standing dark soliton. The width of the soliton is given by the healing length l_0. b) The corresponding phase profile to this case is a step funcion with a sharp phase step of π. c) Demonstration of light-shift potential which leads to the creation of a dark soliton. l_e denotes the potential edge. Figure taken from [Bur1999].

where l_e denotes the width of the potential edge, which determines the steepness of the phase gradient at $z - z_0$. The factor 0.45 is an empirical factor and determines the experimental steepness of the phase gradient resulting from the potential edge l_e. Attainable values for this edge are in the order of $l_e \approx 2\,\mu$m. The desired imprinted phase step $\Delta\phi$ can be chosen by the amplitude of the potential. However, a sharp phase jump of π is impossible to reach in any experimental situation because of the finite slope of the potential edge. Therefore the generated soliton will always be moving with its speed and depth directly depending on l_e and $\Delta\phi$. Furthermore, the imprinted phase profile leads to a field of superfluid flow $v_z(z) = (\hbar/m)\partial\phi(z)/\partial z$ [Bur2002] (see also chapter B). This velocity field leads to a depletion of the density profile in the region of $\partial v_z/\partial z > 0$ for $z > z_0$, which develops into the dark soliton, and to an increase of the density in the region $\partial v_z/\partial z < 0$ for $z < z_0$ (see Fig. 3.2). The timescale for the soliton to develop can be estimated by $\tau_d \approx \tau_{cor}(l_e/\xi)$ [Bur2002] with the healing length of the condensate ξ. In order to efficiently create a soliton, l_e must be on the order of ξ otherwise only shallow solitons can be created. Choosing the correct phase step $\Delta\phi \approx \pi$ is equally important, because if $\Delta\phi$ is too small the soliton will be very shallow or it will not be possible to create a soliton at all. Yet a phase imprint of $\Delta\phi > \pi$ leads to the creation of multiple solitons [Bur2002].

3.2.2 The interference method (density engineering)

Under certain conditions, the collision of two initially separated condensates can lead to the creation of dark solitons. We will now discuss these conditions and the involved mechanism in more detail following the explanation of Scott et al. [Sco1998]. Let us first imagine a single displaced ground state of a BEC evolving in a harmonic trap. As shown by [Mor1997] this wavefunction will retain its shape while undergoing an oscillation with the trap frequency. The spatial phase profile of this system is linear

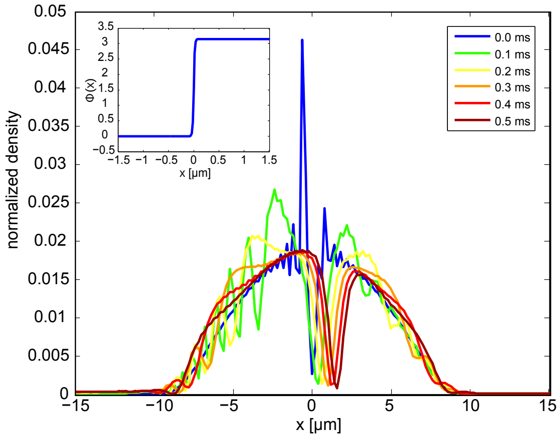

Figure 3.2: Simulation of the phase imprinting method and time evolution of the created soliton by means of the Muñoz Mateo-Delgado equation (see section 2.2.1). The corresponding imprinted phase profile is shown in the inset. Directly after the phase imprint ($t = 0$) a density notch and a peak have developed. The notch develops into a dark soliton moving to the right side. Whereas the peak and accompanying sound waves move much faster to the opposite side. Parameters: $N = 1400$, $\nu_z = 35\,\mathrm{Hz}$ and $\nu_\perp = 408\,\mathrm{Hz}$.

in space with a slope proportional to its velocity. If we now add a second BEC of equal number of atoms in its harmonic ground state displaced by the same distance from the trap center as the first one but in the opposite half of the trap, there will be two different regimes [Sco1998].

In the first one, the so-called linear regime, the wave function of the whole system can be approximated by a superposition of the wavefunctions of each condensate alone. In this case, the two initially separated BECs interfere in the middle of the trap, produce a linear interference pattern there and then separate again regaining their initial shape. At any time during the collision, the fringe spacing of the interference pattern is just given by the wave vectors of each condensate at that time. At the point of maximal overlap this results in a fringe spacing of $l_{fs} = \pi/d(\hbar/(2m\omega_z))$ [Sco1998], with d the initial distance between the condensates. The higher the kinetic energy the higher is the number of fringes and the smaller is the fringe spacing. The linear regime occurs as long as the kinetic energy of the condensates exceeds the nonlinear interaction energy of the atoms. The authors of [Sco1998] approximate the two separate wavefunctions by Thomas-Fermi profiles, the kinetic energy by the curvature of a $\cos^2$ interference pattern and the nonlinear energy by its value at the center of the fringes. Following this ansatz they can estimate a condition for the system to be in the linear regime. This condition is fulfilled if the initial distance between the two atom clouds is bigger than a critical distance D_c.

$$D_c = \pi \left(6 \frac{N \hbar a_s}{\nu_z m} \right)^{1/3} \tag{3.2}$$

Here, N denotes the number of atoms, a_s the s-wave scattering length, ν_z the longitudinal trap frequency and m the atomic mass.

If the distance is smaller than D_c the system is in the second possible regime, the so-called nonlinear regime, where the creation of stable fringes with a phase kink on the order of π out of the interference pattern occurs. These fringes can be identified with dark solitons. Besides this the two initial condensates do not reform separately, but the combined condensate undergoes a quadrupole excitation instead. The formation process of the solitons starts with a linear interference pattern which

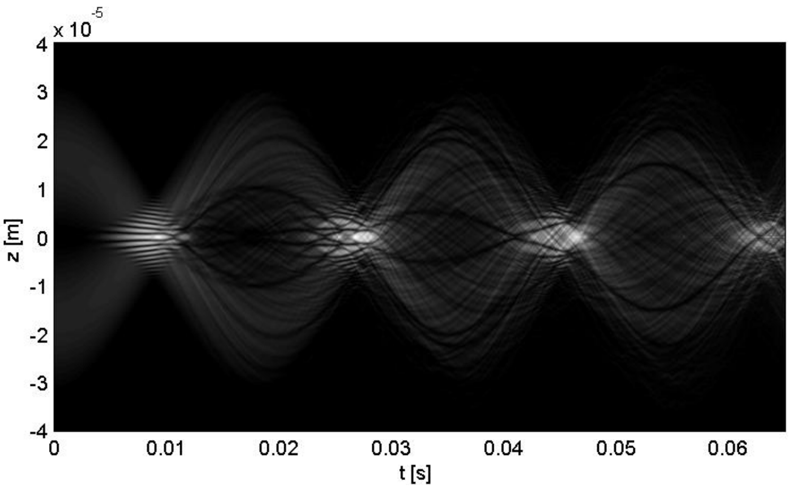

Figure 3.3: The collision of two equally but opposite displaced BEC ground states of a harmonic trap leads to a interference pattern whose central fringes develop into dark solitons, as described in the text. The simulation must be executed using the $3D$ Gross-Pitaevski equation, because of strong transverse excitations during the collision of the two ground states. A test with an effective 1D equation did not even produce solitons as the two atom clouds did not merge but passed through each other meaning that their axial kinetic energy was less reduced in the collision than in the 3D simulation. Parameters: $N = 5000$, $\nu_x = 30\,\mathrm{Hz}$, $\nu_y = \nu_z = 600\,\mathrm{Hz}$ and $d = 34\,\mu\mathrm{m}$.

possesses a multitude of fringes. The central ones exhibit a larger distance from each other and a larger width than the outer ones, because the kinetic energy during the collision process was still smaller during their creation than at the later created outer ones. Only the central fringes which have a width comparable to the one of a soliton transform into dark solitons, because it is energetically favourable to do so. As solitons are stable topological structures they are connected to an extremum of the total energy of the system. Fringes which cannot transform into solitons are not stable and vanish on a time scale of $T/4$ [Sco1998], with the oscillation period T of the trap. The number of created solitons is dependant on the kinetic energy and is always an even number if the phase of the two initially separated condensates is equal (see Fig. 3.3).

If the phase of the initially separated atom clouds is not equal the evolution pattern of the solitons gets asymmetric and also odd numbers of solitons can occur during the creation process. In the special case of a phase difference of $\Delta\phi = \pi$ between the two atom clouds the number of solitons is odd with a standing dark soliton in the middle of the trap.

3.3 Soliton creation by matter wave interference in our experiment

In our experiments, matter wave dark solitons are created by the following interference method. We prepare a BEC of ^{87}Rb in the $5^2S_{1/2}$ $|F=2, m_F=2\rangle$ state in an optical double well potential. This potential is realized by the superposition of an crossed optical dipole trap and an optical lattice (see section 5.3.4). The longitudinal and transversal frequencies of the dipole trap are $\nu_z^{initial} = 63\,\text{Hz}$ and $\nu_\perp^{initial} = 408\,\text{Hz}$, the lattice spacing is $l = 5.7\,\mu\text{m}$. This results in a double well potential with a well distance of $\approx 5.4\,\mu\text{m}$. By switching off the optical lattice the barrier between the two wells is removed. Subsequently the two atom clouds collide and form an interference pattern whose fringes convert into dark solitons due to the nonlinear inter-atomic interaction. Additionally we lower the longitudinal trap frequency to the values of interest $(\nu_z, \nu_\perp)$ with an empirically optimized ramping time to minimize the quadrupole excitation of the atom cloud (see Fig. 3.4). Typical examples for this ramp are from $(\nu_z^{initial}, \nu_\perp^{initial})$ to $(\nu_z, \nu_\perp) = (53\,\text{Hz}, 408\,\text{Hz})$ within $10\,\text{ms}$ for $N = 1700$ atoms or to $(58\,\text{Hz}, 408\,\text{Hz})$ within $3\,\text{ms}$ for $N = 950$. The height of the initial barrier which is on the order of $1\,\text{kHz}$ has to be well optimized. On the one hand it has to be low enough to allow a sufficient tunneling coupling to prevent thermal phase fluctuation at the estimated temperature of $10-20\,\text{nK}$[1]. On the other hand it has to be high enough so that high contrast solitons are formed. As the phase difference between the wells is in principle zero an even number of solitons is created. However, by variation of the experimental parameters the number and the distance between the solitons can be changed as we will discuss below.

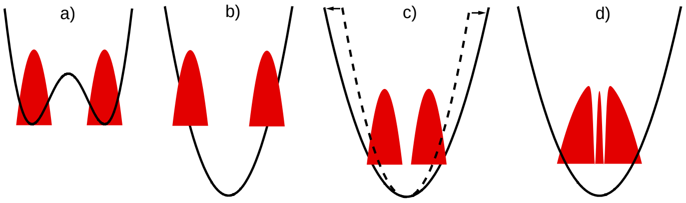

Figure 3.4: a) The initial double well potential. b) The barrier in the middle is switched of which transforms the double well into a harmonic potential. c) The two atom clouds collide in the harmonic potential. The trap is opened in an empirically optimized ramping time to minimize the excitation of quadrupole vibration of the combined atom cloud. d) A nonlinear interference pattern forms whose fringes convert into dark solitons.

---

[1] This temperature was determined by the method of [GatII2006]

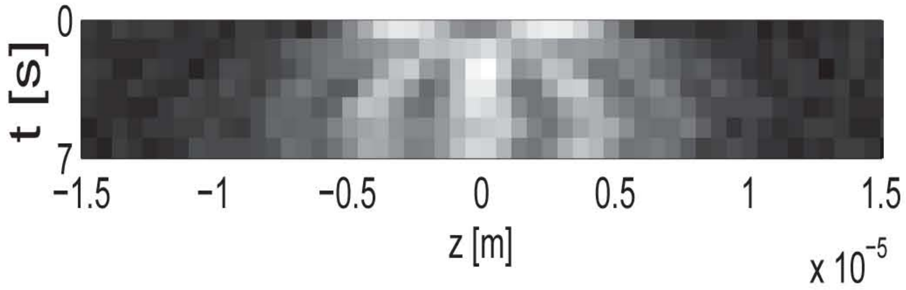

Figure 3.5: Experimental example for the creation of dark solitons by means of matter wave interference.

3.3.1 Varying the number and the distance of the created solitons

Varying the following experimental parameters makes it possible to increase the kinetic energy during the collision process, and by doing so, to lower the distance between the created solitons and to create additional solitons further away from the trap center: Lowering the number of atoms, lowering the ramping-down time of the optical lattice (see Fig. 3.6) and increasing the aspect ratio $\omega_z/\omega_\perp$ of the trap. This knowledge was gained by extensive sets of numerical simulations. Even though it is additionally possible to vary the soliton distance by the height of the optical lattice in the simulations this possibility has to be dropped in the experiment, because we use it to adjust the tunneling coupling between the two initial wells and the initial phase coherence. This is necessary because of the finite temperature of the experiment, whereas the simulation always assumes zero temperature.

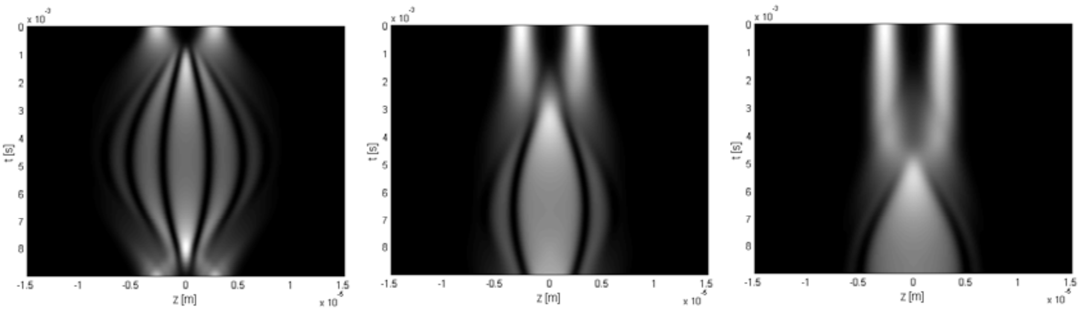

Figure 3.6: Varying the distance of the central soliton pair and the creation of additional solitons further away from the trap center is possible by e.g. changing the duration of the ramping down time of the optical lattice. From left to right: $t_{ramp} = 0\,\mathrm{ms}$, $t_{ramp} = 2\,\mathrm{ms}$ and $t_{ramp} = 4\,\mathrm{ms}$. For the case of longer ramping times the system acquires less kinetic energy which leads to the production of less soliton pairs. Parameters: $N = 1400$, $\nu_z = 63\,\mathrm{Hz}$, $\nu_{perp} = 408\,\mathrm{Hz}$ and $V_0 = 1200\,\mathrm{Hz}$.

3.3.2 Creating an odd number of solitons with our setup

By changing the symmetry of the double well potential for a certain time we can accumulate a phase difference between the wells. This becomes possible by shifting the second beam of the crossed optical dipole trap ('Xdt') (see section 5.3.2) and leads to an energy difference between the levels of the two wells (see Fig. 3.7). In accordance to the equation $\Delta\phi = \Delta E/\hbar \cdot t$ the phase difference is proportional to the duration of the time while the potential is shifted. A small phase difference between the wells leads to an asymmetric evolution pattern of the solitons while a phase shift close to π leads to the creation of a soliton between the other solitons meaning that an odd number of solitons can be produced by this method. If the phase difference is exactly π the central one is a standing dark soliton (see Fig. 3.8). In principle it should be possible to produce even a single soliton by very slowly ramping down the optical lattice resulting in a low collisional energy. However, we could not observe this in the experiment. One problem is the necessary long ramping down time of about $t_{ol} = 7\,\mathrm{ms}$ of the optical lattice. This results in a very shallow slope of the decreasing light intensity, meaning also a long time at low intensities, which is a problem for the phase lock of the optical lattice (see section 5.3.3).

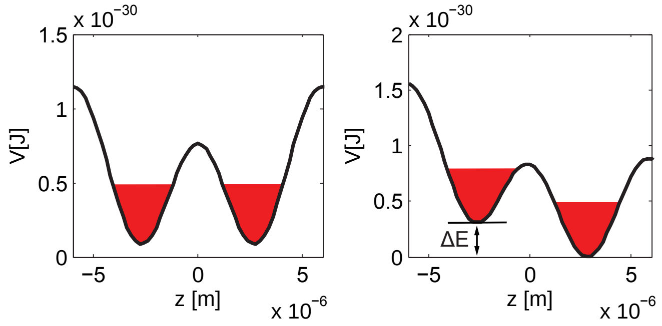

Figure 3.7: By moving the center of the harminic trap relative to the optical lattice we can change the symmetry of the double well potential. This leads to an energy difference ΔE between the levels of the two wells which makes it possible to acquire a phase difference between the two initial atom clouds: $\Delta\phi = \Delta E/\hbar \cdot t$.

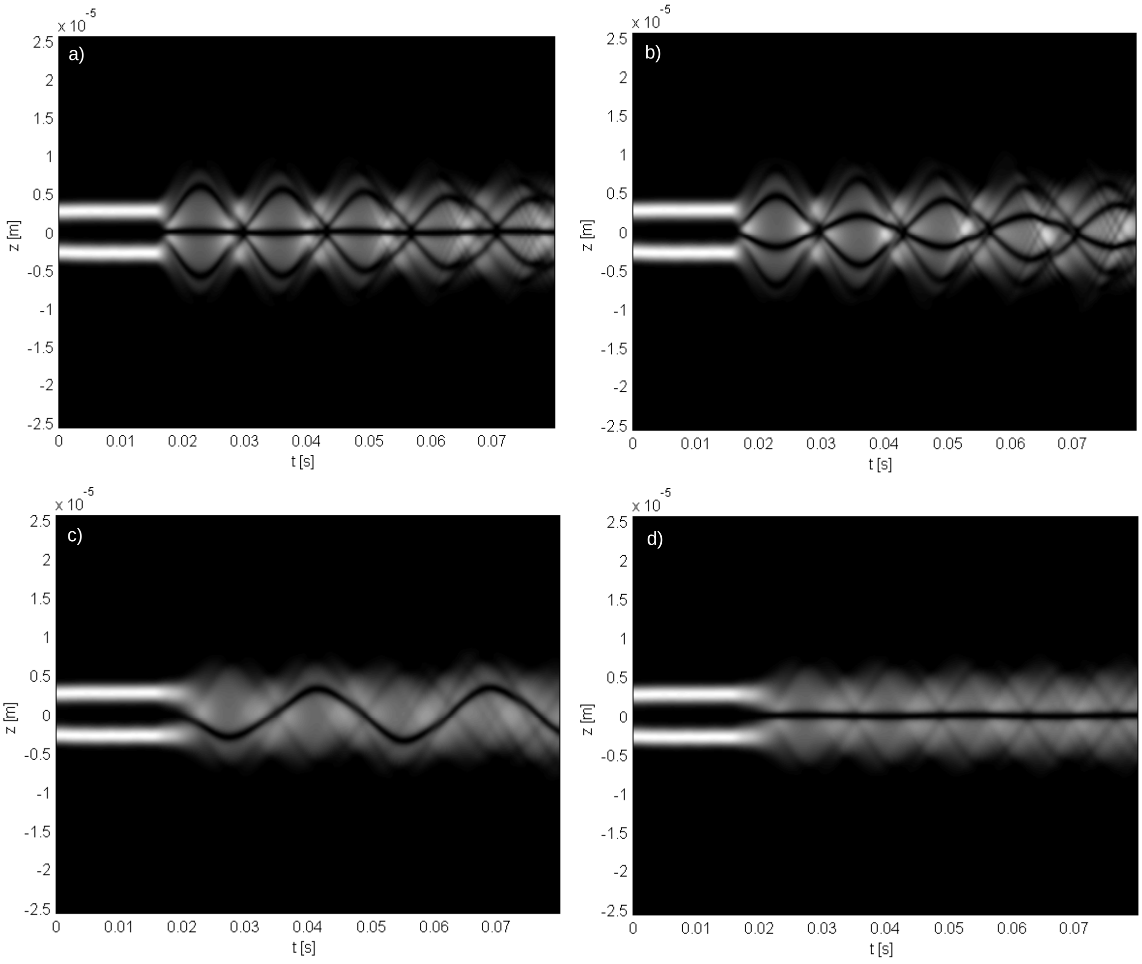

Figure 3.8: By shifting the symmetry of the double well for a certain time a phase difference between the wells can be accumulated as discussed in the text. This can result in the production of an odd number of solitons. By a slow ramping down time t_{ol} of the optical lattice in principle even a single soliton can be gained. a) $\Delta\phi \approx \pi$, $t_{ol} = 2\,\mathrm{ms}$, b) $0 < \Delta\phi < \pi$, $t_{ol} = 2\,\mathrm{ms}$, c) $0 < \Delta\phi < \pi$, $t_{ol} = 7\,\mathrm{ms}$, d) $\Delta\phi \approx \pi$, $t_{ol} = 7\,\mathrm{ms}$. Parameters: $N = 1000$, $\nu_z = 35\,\mathrm{Hz}$, $\nu_{perp} = 408\,\mathrm{Hz}$ and $V_0 = 1150\,\mathrm{Hz}$

3.3.3 Differences between our method and the theoretically suggested method of Scott et al.

In our experiments we start with a BEC in a double well potential which we transform to a harmonic potential and collide the two atom clouds there. The wavefunction has to adjust to the new potential, which means that the situation is more complex than in the case of Scott et al. [Sco1998] (see section 3.2.2). However, the resulting soliton pattern is much less complex as can be seen in Fig. 3.9a. A substantial difference occurs in the creation process of the solitons as from our method only few interference fringes are produced which all convert into solitons (see Fig. 3.10). This shows that the kinetic energy of the colliding atom clouds is much smaller in our case than in the collision of two displaced ground states of the harmonic trap as regarded by [Sco1998]. Besides, in our case the two atom clouds are not perfectly

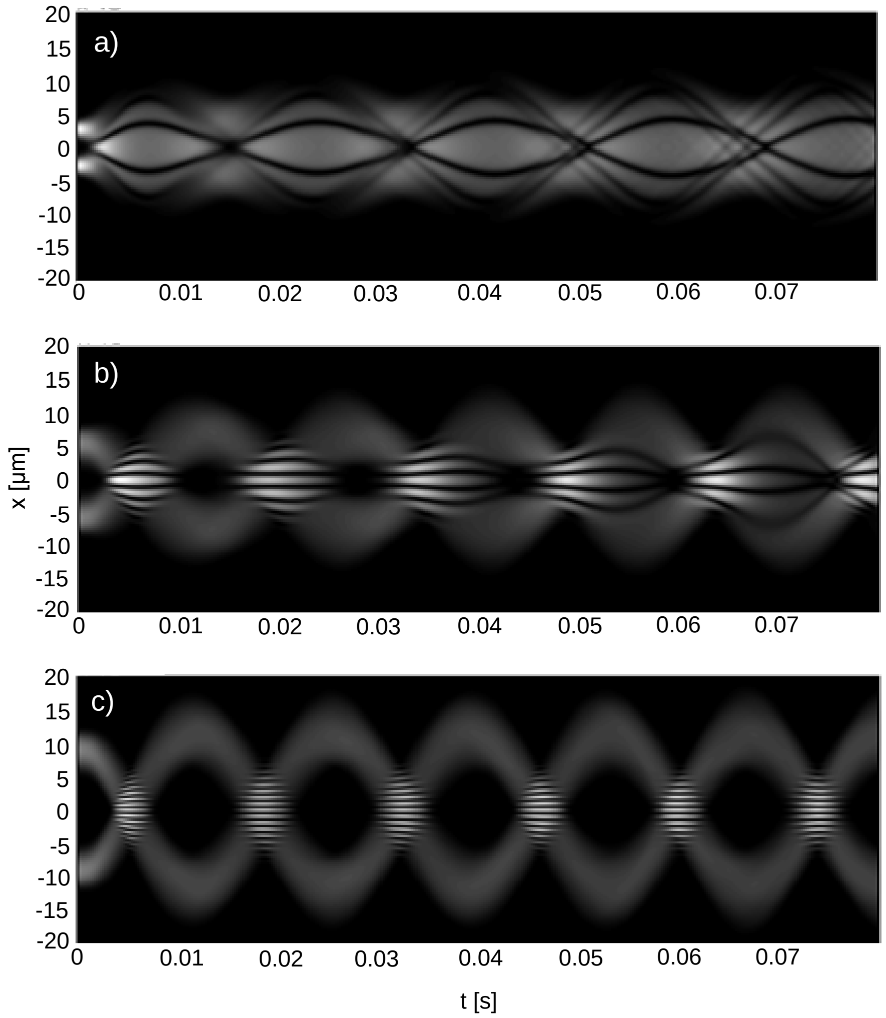

Figure 3.9: Simulation using the Muñoz Mateo-Delgado equation of the different regimes for matterwave interference for our system assuming three different lattice spacings l. Eqn. 3.2 predicts a critical distance of $D_c = 25.4\,\mu\mathrm{m}$ to be in the linear interference regime. a) nonlinear regime as used in our experiments, $l = 5.7\,\mu\mathrm{m}$. c) linear regime, $l = 26\,\mu\mathrm{m}$, b) transition regime, $l = 15\,\mu\mathrm{m}$ Parameters: $N = 1400$, $\nu_z = 22\,\mathrm{Hz}$ and $\nu_{perp} = 408\,\mathrm{Hz}$. The lattice height was adjusted to result in a small but finite density between the wells in each case. Note the different oscillation frequencies of the fringe patterns for the three cases as the trap frequency was kept constant.

in the Thomas-Fermi regime, which was assumed by Scott et al.. This means that Eqn. 3.2 can only be an approximation for our case. But still it gives reasonable results for our situation as can be seen in the example of Fig. 3.9. Furthermore we learned from numerical simulations that there is also a transition regime between the linear and nonlinear regime where at first a linear interference pattern occurs and solitons are formed after several collisions. Fig. 3.9 shows simulations for three different initial distances between the atom clouds: Our case (the nonlinear regime), a case where the distance is slightly above the critical distance D_c (the linear regime) and a situation in between.

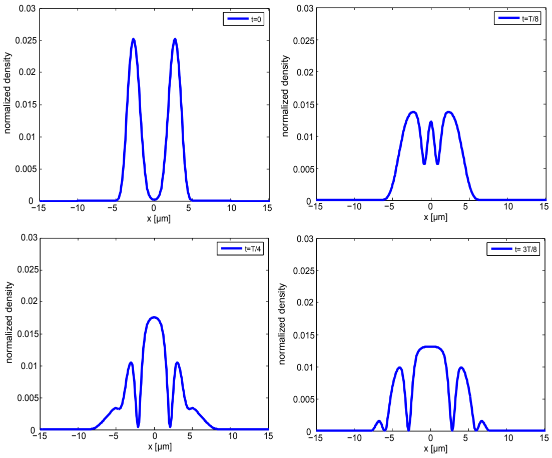

Figure 3.10: DE simulation showing the soliton creation by our method. All fringes that occur are converted into solitons in contrast to the idealized method of [Sco1998].

3.4 Dimensionality regime

A dark soliton in a Bose-Einstein condensate appears from the theoretical point of view as a solution of the homogeneous one-dimensional Gross-Pitaevski equation (see Eqn. 2.2) and is therefore actually a one-dimensional object. However, from the experimental point of view a genuinely 1D regime of the BEC is impossible to reach for two reasons. First every experimentally realizable trapping potential will result in a finite transversal width of the condensate. Second if one can manage to realize a trap with a very small aspect ratio of the trap frequencies $\Omega = \omega_z/\omega_\perp$ and a small number of atoms, as needed for a 1D regime, another problem will occur, the breakdown of the long-range phase coherence of the BEC [Hel2001] which is then referred to as a quasi-BEC. The appearing phase fluctuations of the BEC cannot be captured by the GPE. In this regime a dark soliton, which is directly connected to a phase-kink, cannot be stable. For the creation of a dark soliton the experimentalist has to make a compromise. The system should be close to 1D but cannot be genuinely 1D. This restricts one to a regime which is called the crossover regime between 1D and 3D with a cigar shaped BEC. Dark solitons can be dynamically stable there [Mur1999, Mur2002] so that only dissipative effects induced by the finite temperature can destroy the soliton [Fed1999].

To estimate the dimensionality of a BEC the following dimensionless parameter can be employed [Men2002]:

$$N\Omega a_s/a_\perp, \tag{3.3}$$

with a_s the s-wave scattering length and $a_\perp = \sqrt{\hbar/(m\omega_\perp)}$ the transverse harmonic oscillator length. For $N\Omega a_s/a_\perp \gg 1$ the system is in the radial Thomas-Fermi regime [Men2002] where many modes of the harmonic oscillator are excited in the radial direction. This is the genuinely 3D regime where all directions of the BEC are described by a Thomas-Fermi density profile. The Thomas-Fermi density profile in the longitudinal direction n_1 can be calculated by $n_1(z) = \frac{1}{16a}(15N\Omega a/a_\perp)^{4/5}(1-\frac{z^2}{Z^2})^2$ [Men2002] with the Thomas-Fermi radius $Z = \frac{a_z}{\sqrt{\Omega}}(15N\Omega a/a_\perp)^{1/5}$ and the longitudinal harmonic oscillator length $a_z = \sqrt{\hbar/(m\omega_z)}$.

For $N\Omega a_s/a_\perp \ll 1$ the 1D mean field limit is reached [Men2002], where the BEC approaches the Gaussian ground state of the harmonic oscillator in its radial direction. In this regime the Thomas-Fermi condition for the longitudinal density profile is only fulfilled if

$$\left(\frac{N}{\sqrt{\Omega}}\frac{a}{a_\perp}\right)^{1/3} \gg 1. \tag{3.4}$$

We refer to the regime which fulfills $N\Omega a_s/a_\perp \ll 1$ as well as Eqn. 3.4 as the Thomas-Fermi 1D (TF 1D) regime. The crossover regime between 1D and 3D is characterized by $N\Omega a_s/a_\perp \approx 1$. Fig. 3.11 shows the different possible regimes for a BEC. Most

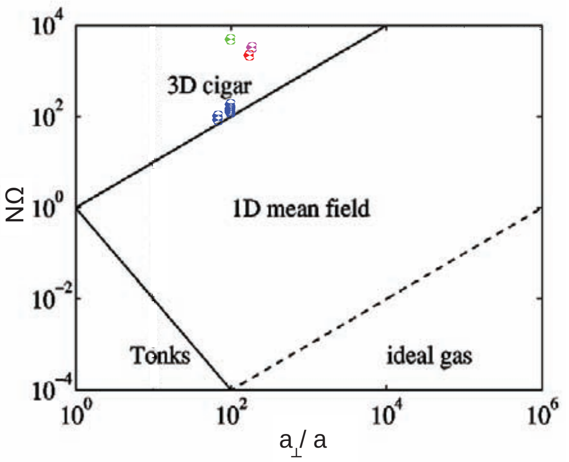

Figure 3.11: Different dimensionality regimes of a BEC. The 3D and the 1D mean field regime are discussed in the text. In the Tonks regime the atoms of the BEC behave like hard core particles. The dashed line indicates the $N\Omega = \Omega^{3/2}a_\perp/a$ for the example of $\Omega = 10^{-4}$. Stable dark solitons can be created in the crossover regime between 1D and 3D. The regimes of different experiments concerning dark solitons are marked by the dots. green: Burger et al. [Bur1999], magenta: Shomroni et al. [Sho2008], red: Stellmer et al. [Ste2008], blue: our experiments. Diagramm taken from [Men2002] and adapted.

experiments which have been executed concerning dark solitons were performed with a high number of atoms between 10^4 to 10^6. Consequently, with Eqn. 3.3 a very small aspect ratio of the trapping frequencies is needed to get close to the 1D regime. Our experiment offers the possibility to reproducibly create BECs with small atom numbers on the order of 10^3 which additionally helps to reduce the dimensionality of the system. Fig. 3.11 shows some of the dark soliton experiments that have been closest to the 1D regime. For our measurements the parameter $N\Omega a_s/a_\perp$ was in the range of $1.2 - 1.8$ and the parameter $((N/\sqrt{\Omega})a_s/a_\perp)^{1/3} \approx 2.8 - 4.4$.

Chapter 4

Experimental results

In this chapter we will discuss in detail the experiments about dynamics and interaction of dark solitons in Bose-Einstein condensates performed in the context of this thesis. We will start explaining how our measurements were conducted in general. Then we will go on to the systematic measurements of the frequency of two solitons oscillating together in a harmonic trap and to the effects of the solitons mutual interaction which we can conclude from our observations. The experimental results are compared with simulation using the three-dimensional Gross-Pitaevskii equation (3D GPE) and the Nonpolynomial-Schrödinger equation (NPSE) and with the effective potential approach. We demonstrate the possibility to vary the number of created solitons in our experiment. Finally we discuss the stability of our created solitons.

4.1 Observation of dark solitons in our experiments

We start with the creation of our solitons using the interference method explained in section 3.3 and take images of the the BEC after the desired evolution time. Using the technique of high power absorption imaging we shine a resonant laser beam onto the atom cloud and detect the shadow of the BEC on a CCD camera (see section 5.4). In single shots of the experiment we get pictures like shown in the top row of Fig. 4.1. In these pictures we can detect the distance of the solitons from the trap center at different points in evolution time to observe their oscillation dynamics as discussed in section 4.2 or the depth of the soliton notch as discussed in section 4.5.4. To demonstrate the time evolution of the solitons it is more convenient to use pictures averaged over several shots to reduce the noise of the images. To enhance the contrast of the solitons in the pictures we additionally use a short time of flight before imaging between 0.6 and 0.9 ms. Note that averaging the images only works up to about $80 - 100\,\mathrm{ms}$ of evolution time. On longer evolution times we loose the shot-to-shot reproducibility of the experiment due to effects that smear out the trajectories of the solitons. We will discuss these effects in detail in section 4.5.4. Up to the above mentioned time scale we can use the averaged images to produce time evolution plots

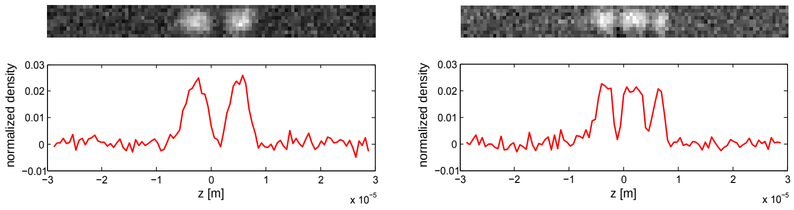

Figure 4.1: Single shots of the density profile of the BEC including two dark solitons. The solitons appear as density notches in the profiles. **left:** Point of closest distance of the solitons. Because of the limited optical resolution of the experiment ($\approx 1\mu m$) we can not distinguish the two solitons at this point resulting in a single density dip. **right:** Two dark solitons close to the amplitude of their oscillation in the trap. For each point in time the original images as well as their integration over the transverse direction is shown.

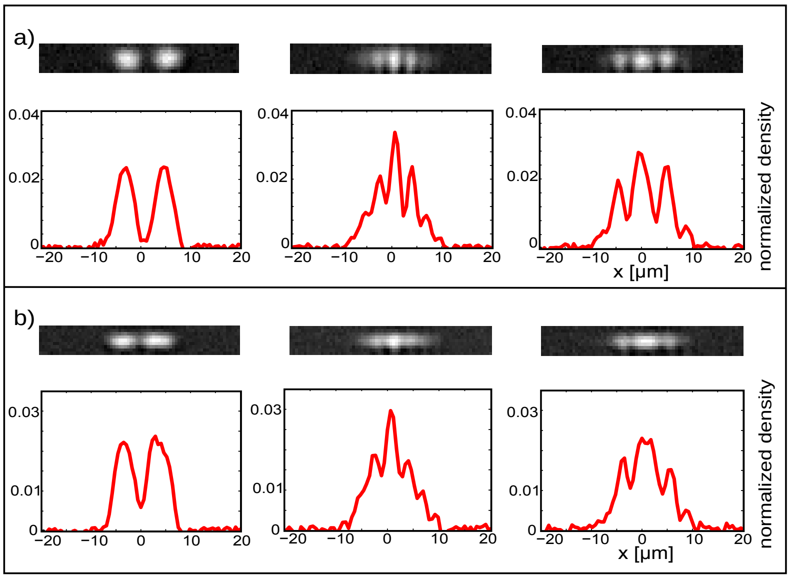

Figure 4.2: Images of the dark soliton dynamics in the harmonically trapped BEC at different point during the time evolution of the solitons. The images are averaged over approximately 15 shots. a) Time of flight of $0.8\,\mathrm{ms}$. b) Insitu imaging without time of flight. The images of each column correspond to similar points in the time evolution.

in analogy to the evolution plots obtained by simulations. To do so we integrate the averaged pictures over their transverse direction and get longitudinal density profiles. If we now pile up these longitudinal profiles (vertical lines in Fig. 4.3) in a row we can get experimental time evolution plots like the ones shown in Fig. 4.3a and 4.4.

We additionally compare our experiments to simulations which helps to understand the soliton dynamics in more detail and to optimize the choice of experimental parameter sets. As an example we execute a 3D GPE simulation (see Fig. 4.3b) for the experimental parameters used for the measurement of Fig. 4.3a. Including the optical and time resolution, the experimentally observed density profile evolution is well reproduced (see Fig. 4.3c). A dominant pair of solitons oscillates close to the center of the cloud and we can also distinguish additional pairs of solitons with much lower contrast. In the following, we focus on the dynamics of the dominant central pair and show that its oscillation frequency is well described within a two soliton approximation.

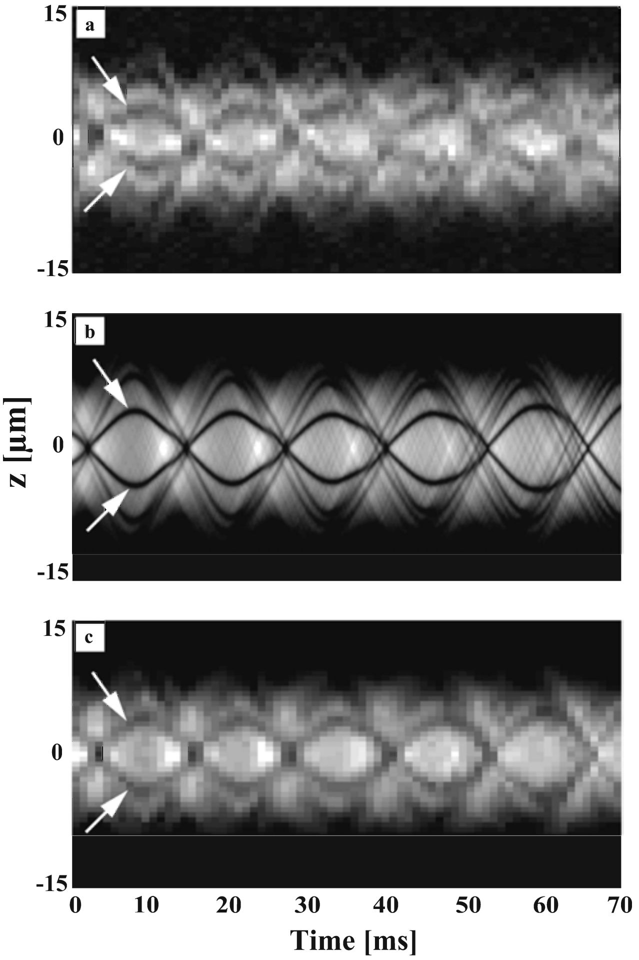

Figure 4.3: Observation of the time evolution of dark solitons in a harmonic trap. The dominant soliton pair is indicated by arrows. a) Experimental observation of the dynamics of the longitudinal atomic density. Each longitudinal density profile (vertical lines), corresponding to a given evolution time, is deduced from 7 experimental realizations. The obtained absorption images of the condensate at each time step are averaged and integrated over their transverse direction. The number of atoms in the shown case is $N = 1700$ and the trapping frequencies are $(\nu_z, \nu_\perp)$=(53 Hz,890 Hz). b) Result of the numerical integration of the 3D GPE taking into account the full preparation process of the solitons. c) Same as b), taking into account the finite spatial (1 μm) as well as temporal resolution (1 ms) of the experiment. The loss of contrast on this timescale can be explained by the convolution of the imaging process (see section 4.5.4 and Fig. 4.17).

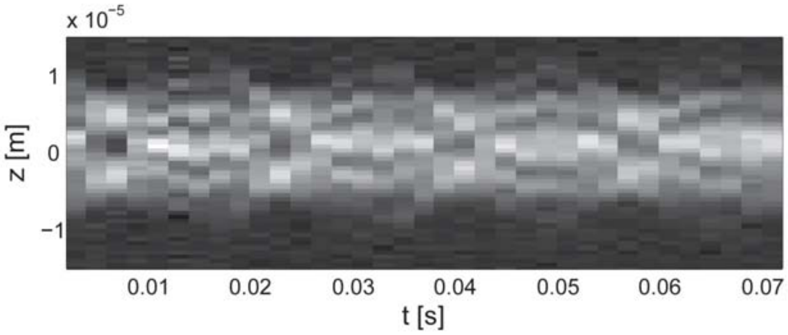

Figure 4.4: Experimental time evolution of soliton dynamics. Parameters: $\nu_z = 37 \pm 0.85\,\mathrm{Hz}$, $\nu_\perp = 407.5 \pm 40.8\,\mathrm{Hz}$, $N = 1603 \pm 132$.

4.2 Measurement of the oscillation frequencies and the inter-soliton interaction

Having overcome the snaking instability (see section 4.5.1) our solitons are dynamically stable. This enables us to observe the soliton dynamics including multiple collisions and makes it possible to measure interesting features of the solitons such as their oscillation frequency, their velocity and their mutual interactions.

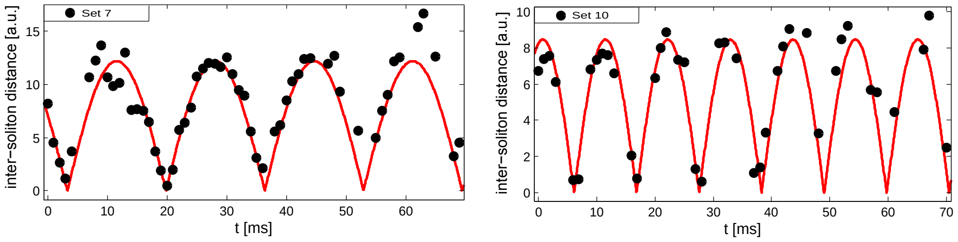

Figure 4.5: In order to extract the oscillation frequency of the solitons in the experimental data, we determine the distance between the two solitons in single shots of the experiment for 3 to 10 runs. Subsequently, the results are averaged for each point in time. Note that it is not always possible to determine a proper distance in every shot. In these cases the shots are dropped. We then fit the resulting time evolution of the inter-soliton distance. The obtained frequency is divided by two in order to compare it to the oscillation frequency expected for a single trapped soliton. The shot to shot reproducibility of the soliton dynamics up to $100\,ms$ allows the observation of up to 7 collisions. The typical statistical experimental error in the frequency measurement is ±1.5% In the shown examples (parameter set 7 and 10 of Tabs. 4.1 and 4.2) we determine the oscillation frequency to be: $\nu_d = (30.25 \pm 0.24)\,\mathrm{Hz} = (0.778 \pm 0.007) \cdot \nu_z$ (left) and $\nu_d = (46.70 \pm 0.28)\,\mathrm{Hz} = (0.810 \pm 0.009) \cdot \nu_z$ (right).

4.2.1 Oscillation frequency and dimensionality effect

Particularly interesting is the fact that the oscillation frequency of a dark soliton in a harmonic trap is expected to be slower than the trap frequency (see section 2.4). For a single dark soliton oscillating in a harmonically trapped BEC it was calculated analytically to be [Bus2000]:

$$\nu_d^{1D} = \frac{\nu_z}{\sqrt{2}} \approx 0.707\nu_z, \tag{4.1}$$

with ν_z being the longitudinal frequency of the trap. This result obtained by Busch and Anglin is only valid for the TF 1D regime [Men2002], which is characterized by $N\Omega a_s/a_\perp \ll 1$ and $((N/\sqrt{\Omega})a_s/a_\perp)^{1/3} \gg 1$. Later Theocharis et al. [The2007] showed that if the system is not perfectly 1D or not in the TF-regime the frequency of the soliton ν_d is still smaller than the frequency of the harmonic trap, but lies in the range: $\nu_d^{1D} < \nu_d < \nu_z$ (see section 2.4). As the value ν_d^{1D} became quite famous and well known we regard every soliton frequency in the range of $\nu_d^{1D} < \nu_d < \nu_z$ as being upshifted from ν_d^{1D}.

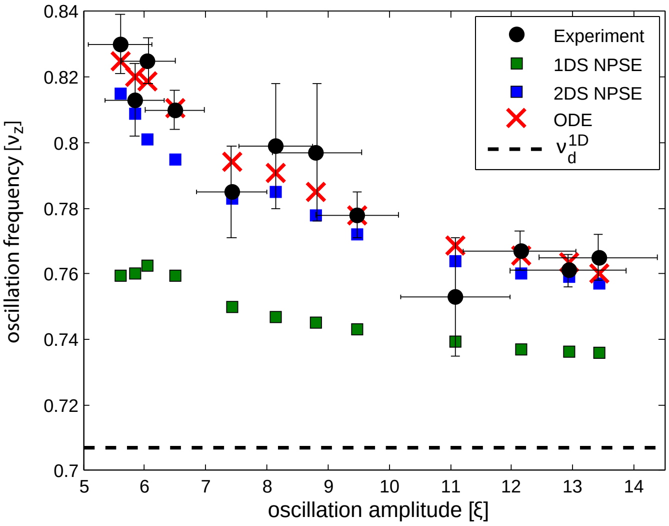

Figure 4.6: Comparing the experimental results with the values obtained from NPSE simulation of the corresponding parameter sets and with the results from the effective potential. Details are discussed in the text.

The parameter ranges for the TF- and dimensionality-parameters in our experiments which we will discuss in the following are given by: $((N/\sqrt{\Omega})a_s/a_\perp)^{1/3} \approx 2.8 - 4.4$ and $N\Omega a_s/a_\perp \approx 1.2 - 1.8$, respectively. As therefore all our measurements are performed in the crossover regime between 1D and 3D (see section 3.11) the measured frequencies are expected to be upshifted from ν_d^{1D} and we will call this the dimensionality effect. This is exemplified in the two measurements of Fig. 4.5 for which we get $v_d = (0.778 \pm 0.007)\nu_z$ and $v_d = (0.810 \pm 0.006)\nu_z$. How we determine the soliton oscillation frequency from single shots of the experiment is explained in the caption of Fig. 4.5. But we measure deviations from ν_d^{1D} of up to 16% (see Fig. 4.6) which cannot be explained by the dimensionality effect alone. These high upshifts are due to the fact that in our experiments not a single but two solitons oscillate in a harmonic trap. The interaction between the two solitons leads to an additional frequency upshift. This will be the content of the following.

4.2.2 Inter-soliton interaction effects

Since the two dominant solitons created in our experiment have a distance of a few healing lengths ξ (ξ is on the order of $250-400nm$) the inter-soliton interaction leads to a significant modification of their oscillation frequency as discussed in section 2.5.2. This interaction and the corresponding frequency upshift is strongly depending on the oscillation amplitude of the solitons, or in other words, on the mean distance of the solitons during the oscillation. To observe this effect we perform systematic measurements for different mean inter-soliton distances.
As discussed in section 3.3.1 our setup offers different possibilities to change the distance between the created solitons. In our measurements we varied the aspect ratio $\Omega = \nu_z/\nu_\perp$ and the number of atoms N forming the BEC. The experimental parameter sets of the 12 executed measurements are shown in table 4.1. These result in soliton oscillations specified by the parameters of table 4.2. In Fig.4.6 we see that the oscillation frequency clearly increases with decreasing oscillation amplitude. At first we compare this result with IS simulations using the NPSE (see section 2.2.2) at which we initialize a single dark soliton in a trap corresponding to the experimental parameters and at an oscillation amplitude equal to the one obtained from the fit of the experimental data, see Fig.4.6. We observe two facts: Firstly the frequencies of the single soliton simulations are upshifted from the value of ν_d^{1D} by a few percent due to the dimensionality of the system; secondly the experimental data,in agreement with the two soliton simulations and the effective potential approach, is again upshifted from the single soliton simulation results by another few percent. This second effect, which in contrast to the dimensionality effect, strongly depends on the oscillation amplitude, can only be explained by the repulsive interaction between dark solitons due to the effective potential (see section 2.5.1 and Eqn. 2.26):

$$V(z, \dot{z}) = (2\pi\nu_{1s})^2 \frac{z^2}{2} + \frac{\mu B^2}{2m \sinh^2(2Bz/\xi)}. \tag{4.2}$$

In this model we regard the solitons as particles oscillating in an effective potential of Eqn. 4.2, which takes into account the dimensionality of the system and the mutual interaction between the solitons. This picture is exemplified in Fig. 4.7. We set the interaction parameter μ to be the chemical potential of the condensate obtained from the 3D GPE equation and the darkness of the solitons to $B = \sqrt{1 - \dot{z}^2/c_s^2}$, with $c_s = \sqrt{\mu/m}$ the Bogoliubov speed of sound. Now we can apply the equation of motion corresponding to the potential of Eqn. 4.2 to the frequencies obtained from the single soliton simulations ν_{1s}. By doing so we include the dimensionality effect. As can be seen in Fig. 4.6 the oscillation frequencies get shifted up to the values marked by the "red x" due to the effect of the interaction potential. The obtained

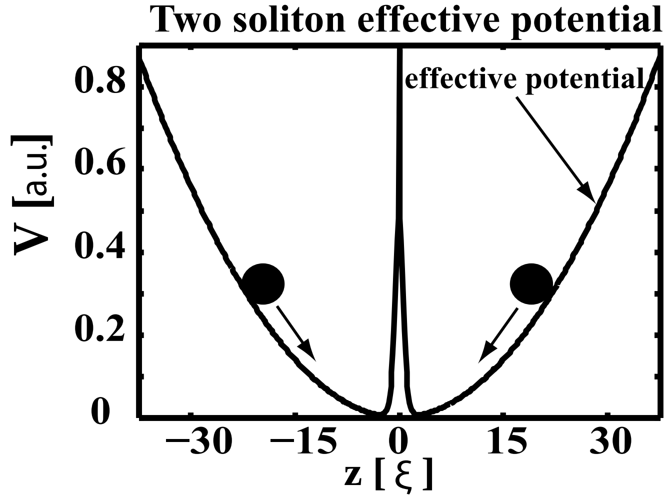

Figure 4.7: Two solitons symmetrically oscillating in a harmonically trapped BEC can be modeled by classical particles. The effective potential has to include the repulsive inter-soliton interaction. We show here a simplified plot of the effective soliton potential neglecting the velocity dependence of the interaction.

frequencies are in good agreement with the experimental data. We confirm our findings by IS simulations where we initialize two solitons in the BEC at an oscillation amplitude equal to the one obtained from the fit of the experiment. These are also marked in Fig. 4.6 and fit the experimental data as well as the results obtained by the analysis of the interaction potential. The good agreement between numerics and experiments also shows that the dynamics produced by our experimental method is well described within a two soliton approximation even though extra solitons are produced.

For a more systematic analysis of the effects which influence the oscillation frequency of dark solitons we perform extensive numerical studies using the NPSE for each experimental parameter set. Here we keep the parameters of the trap and the atom number constant but vary the oscillation amplitude of the solitons in many steps. We perform simulations for the single as well as for the two soliton case and determine the oscillation frequencies by fitting the soliton trajectories. From these simulations we can draw curves that show the behavior of the soliton oscillation frequency depending on the oscillation amplitude for both cases (see Fig. 4.8). Additionally we apply the equation of motion to all the single soliton simulations resulting in another set of curves of the type frequency vs. amplitude. As exemplified in Fig. 4.9 the agreement of the model with NPSE simulations is better than 5% in our experimentally accessible parameter range. This allows us to clearly identify the significant role of the repulsive interactions and shows that the effective repulsive potential in Eqn. (4.2) obtained in the 1D homogeneous case is a good approximation to our complex situation. We can now plot in Fig. 4.8 the range covered by all two soliton simulation curves together with the experimental data and realize that there is good agreement between the behavior of the frequency trend of the experimental measurements and the simulations. For reasons of clarity we also plot three selected

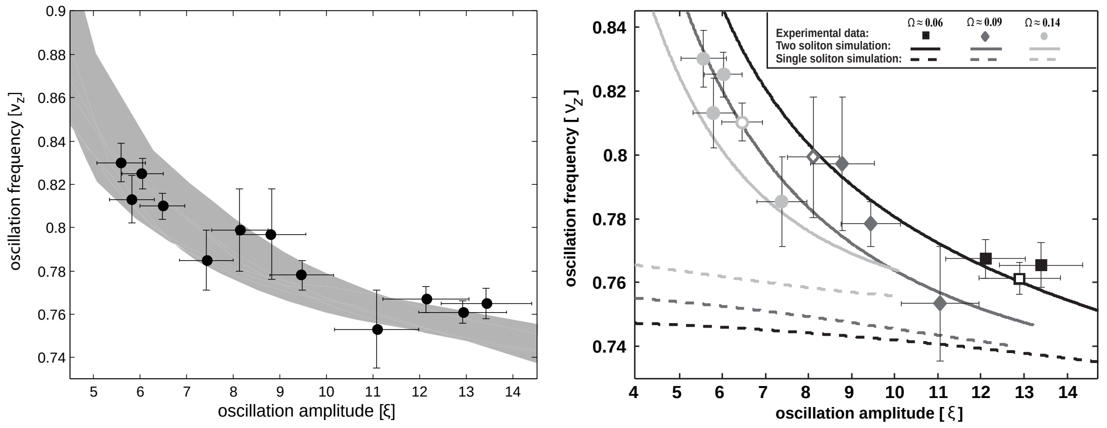

Figure 4.8: **left:** Frequency trend mainly due to the inter-solitonic interaction. As every parameter set is expected to have a slightly different dependency of its soliton oscillation frequency vs. its oscillation amplitude we show the range expected by numerical simulations for all parameter sets together as the grey shaded area. **right:** The distance between the solitons in the experiment is varied using different aspect ratios of the trap and different mean atom numbers. The experimental data points are grouped in three different ranges of the aspect ratio. For each range we plot a selected simulation curve corresponding to the parameter set of the unfilled data point. The experimental errors are estimated from the standard deviation of the calibrations for the trap frequencies and the systematic error of the atom number.

simulation curves, one for each of the three different aspect ratio ranges Ω used in the experiment and add these to the experimental data (see Fig. 4.8(right)). Eventually our investigation reveals, that dark solitons can be modeled by regarding them as classical particles with repulsive short range interaction exhibiting a length scale of the healing length. Additionally our experiments show that dark solitons can indeed survive multiple collisions, as predicted by numerical simulations of the GPE.

4.2.3 Separating the effect of interaction from the dimensionality effect in our measurements

Finally, we discuss the role of the dimensionality effect for our measurements in more detail. This effect can be decomposed into two contributions: The actual effect of dimensionality and the effect of being out of the TF-regime. For example, considering one specific parameter set with $\Omega \approx 0.06$, the upshift for a single soliton is $\approx 5\%$ (see Fig. 4.9). Predictions using the 1D GPE already give a value $\approx 2\%$ higher than the asymptotic limit because the Thomas-Fermi limit is not reached. The effect of dimensionality, i.e. the role of the transverse degrees of freedom which is captured only by the NPSE or the 3D GPE, accounts for the remaining $\approx 3\%$. To demonstrate the dimensionality effect Fig. 4.9 shows the comparison between the single soliton NPSE simulation and the $\nu_z/\sqrt{2}$-prediction for the considered parameter set.

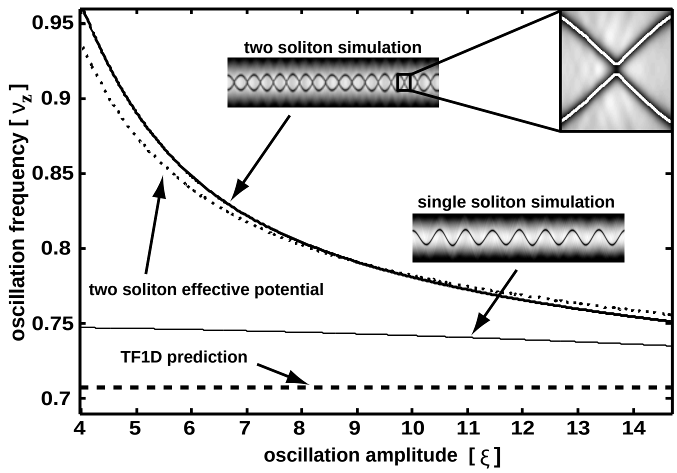

Figure 4.9: Oscillation frequencies expected for dark solitons vs. the oscillation amplitude for the example of parameter set 2 of table 4.1. Due to the dimensionality effect the frequencies obtained by numerical simulations for a single soliton (thin line) are always higher than the TF 1D frequency prediction (bold dashed line). If we apply the ODE corresponding to the effective potential of Eqn. 4.2 to the frequencies obtained by the single soliton simulations, we get upshifted to the thin dashed line. The two soliton NPSE simulation is in good agreement with this result. The deviations are smaller than 5%. Comparison between single soliton simulation, two soliton simulation and effective potential result reveals, that the strongly oscillation amplitude dependent upshift of the two soliton case is due to the repulsive inter-solitonic interaction. The insets show an example for a single and a two soliton NPSE-IS simulation. The zoom in the two soliton case shows, that the solitons do not cross in the simulations. The white lines denote the trajectories of the density minima of the two solitons.

Note that one has to be careful if trying to separate the effects of dimensionality and interaction. Since the interaction strength of the potential of Eqn. 4.2 is dependent on the chemical potential μ and is therefore itself influenced by the dimensionality of the system. This means that it is only possible to separate the effects of dimensionality and interaction, if one regards the case of single soliton and two soliton oscillation for the same set of the parameters: ν_z, $\nu_\perp$ and N. Therefore, in Fig. 4.8(right) only the single and two soliton simulation curves of equal color can be compared.

Set#	$\nu_z[Hz]$	$\nu_\perp[Hz]$	Ω	N	$N\Omega a_s/a_\perp$
1	53.85 ± 0.27	890 ± 89	0.061 ± 0.006	1372 ± 93	1.22 ± 0.15
2	53.0 ± 0.25	890 ± 89	0.060 ± 0.006	1708 ± 81	1.50 ± 0.15
3	25.7 ± 0.17	407.5 ± 40.8	0.063 ± 0.006	2079 ± 106	1.30 ± 0.15
4	32.9 ± 0.7	407.5 ± 40.8	0.081 ± 0.008	1763 ± 116	1.42 ± 0.17
5	37.0 ± 0.85	407.5 ± 40.8	0.091 ± 0.009	1603 ± 132	1.45 ± 0.19
6	37.0 ± 0.85	407.5 ± 40.8	0.091 ± 0.009	1438 ± 97	1.30 ± 0.16
7	38.9 ± 0.19	407.5 ± 40.8	0.096 ± 0.010	1536 ± 126	1.46 ± 0.19
8	54.0 ± 0.82	407.5 ± 40.8	0.133 ± 0.015	1375 ± 124	1.81 ± 0.25
9	57.65 ± 0.29	407.5 ± 40.8	0.142 ± 0.014	863 ± 134	1.21 ± 0.22
10	57.65 ± 0.29	407.5 ± 40.8	0.142 ± 0.014	945 ± 120	1.33 ± 0.22
11	57.97 ± 0.31	407.5 ± 40.8	0.142 ± 0.014	1055 ± 105	1.49 ± 0.21
12	57.0 ± 0.3	407.5 ± 40.8	0.140 ± 0.014	870 ± 120	1.21 ± 0.21

Table 4.1: Experimental parameters for the 12 measurements.

Set#	$\nu_{1s}[Hz]$	$\nu_d[Hz]$	ν_d/ν_z	$z_{max}[\xi]$	$\xi[\mu m]$
1	39.68	41.32 ± 0.26	0.767 ± 0.006	12.15 ± 0.78	0.257
2	39.03	40.32 ± 0.20	0.761 ± 0.005	12.94 ± 0.60	0.250
3	18.91	19.67 ± 0.13	0.765 ± 0.007	13.43 ± 0.66	0.377
4	24.32	24.77 ± 0.26	0.753 ± 0.018	11.09 ± 0.91	0.372
5	27.57	29.49 ± 0.34	0.797 ± 0.021	8.81 ± 0.78	0.371
6	27.63	29.55 ± 0.19	0.799 ± 0.019	8.15 ± 0.48	0.377
7	28.91	30.25 ± 0.24	0.778 ± 0.007	9.47 ± 0.40	0.371
8	40.49	42.37 ± 0.35	0.785 ± 0.014	7.44 ± 0.47	0.359
9	43.95	47.56 ± 0.29	0.825 ± 0.007	6.05 ± 0.32	0.380
10	43.78	46.70 ± 0.28	0.810 ± 0.006	6.50 ± 0.37	0.375
11	44.03	46.35 ± 0.60	0.830 ± 0.009	5.61 ± 0.62	0.369
12	43.33	48.12 ± 0.48	0.813 ± 0.011	5.84 ± 0.53	0.380

Table 4.2: Parameters characterizing the soliton oscillation.

4.3 Experimentally varying the number of solitons

As discussed in section 3.3.1 our experimental setup allows to vary the number of created solitons. Fig. 4.10 shows the example of four oscillating solitons and two additional weak solitons at the edge of the trap. In this case an increased lattice height was chosen to create a higher number of solitons. On the one hand this results in a higher collisional energy producing more solitons but on the other hand we loose the initial phase stability resulting in an early fading out of the soliton contrast (see section 3.3.1). The evolution plot is averaged over 10 runs.

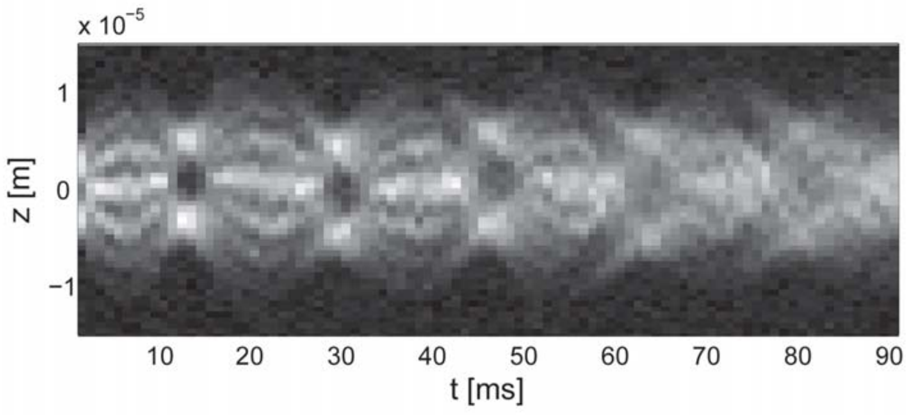

Figure 4.10: Observation of the oscillation of four dark solitons including the creation process.

4.3.1 Three oscillating solitons

Using the procedure described in section 3.3.2 we can produce an odd number of solitons. Especially interesting is the case were one soliton is standing between the others in the center of the trap. In this case the interaction potential is increased as the resting soliton is really black, meaning $B = 1$ in the potential of Eqn. 2.27. This case can be realized by a phase difference of an odd multiple of π between the wells of the initial double well. We can now set the creation process and its involved kinetic energy to produce three solitons as shown in Fig. 4.11. In analogy to the two soliton case we would now be able to probe the soliton oscillation frequency depending on the inter-soliton distance. Due to the increased interaction in this case we expect according to the simulation and effective potential results a higher frequency upshift as in the two soliton case (see section 4.11). A first measurement has been taken (Fig. 4.11) and its frequency has been deduced. In Fig. 4.13 we additionally show the corresponding ideal one soliton and three soliton simulation curves. Unfortunately the outer solitons were created with very high oscillation amplitude in the experiment, which on the one hand prevents the direct comparison with our executed two soliton measurements and on the other hand involves additionally fitting problems in the IS simulations (see caption of Fig.4.13). The reason for this is that the oscillation amplitude of the performed three soliton experiment is very close to the longitudinal size of the condensate. The solitons in the IS simulation, if put in at such large oscillation amplitude, cause a breathing of the whole atom cloud resulting in a growing oscillation amplitude and the excitation of additional weak solitons (see Fig. 4.12).

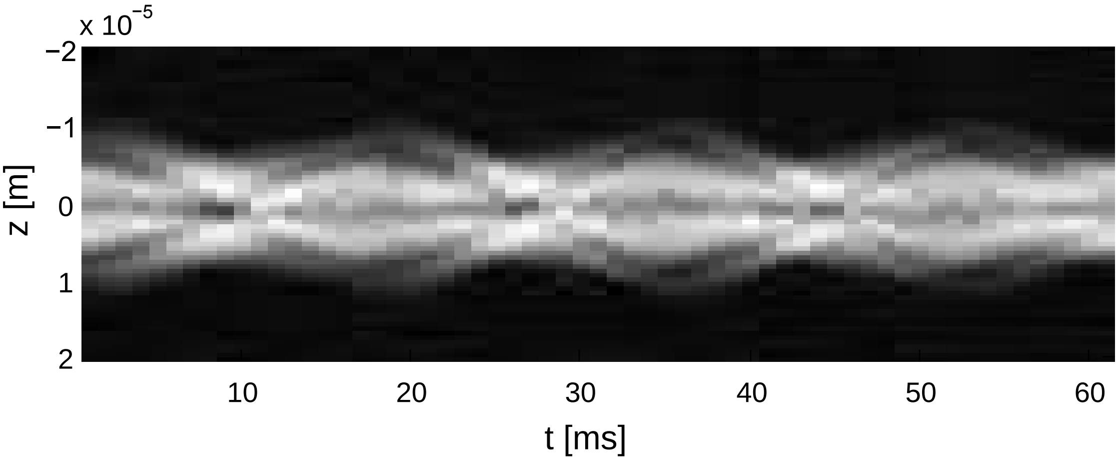

Figure 4.11: Experimental observation of three dark solitons averaged over 16 runs. The soliton in the center of the trap is at rest (black soliton) whereas the two outer ones are undergoing an oscillation with increased frequency due to the stronger interaction with the standing soliton in the middle, compared to the two soliton case. The reduction of the collisional energy and the resulting high oscillation amplitude of the outer solitons was achieved by a slow ramping down of the optical lattice on a timescale of $2\,\mathrm{ms}$ (see section 3.3.1). Parameters: $\nu_z = 36.1 \pm 0.25\,\mathrm{Hz}$, $\nu_\perp = 407.5 \pm 40.8\,\mathrm{Hz}$, $N = 1570 \pm 146$

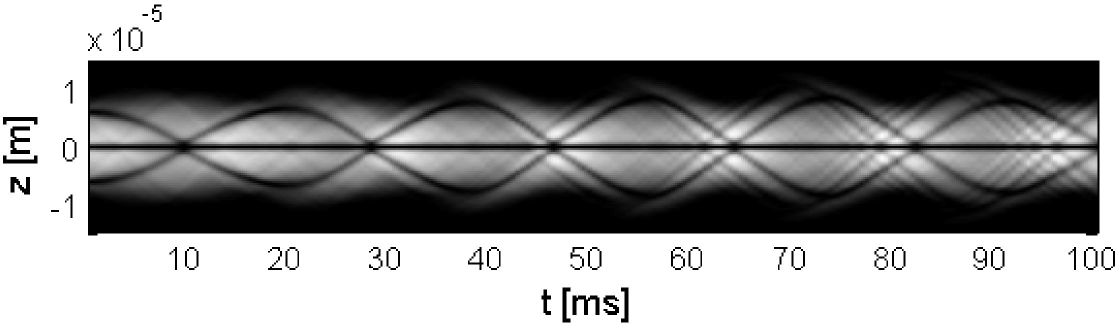

Figure 4.12: IS simulation corresponding to the parameter set of the three soliton measurement.

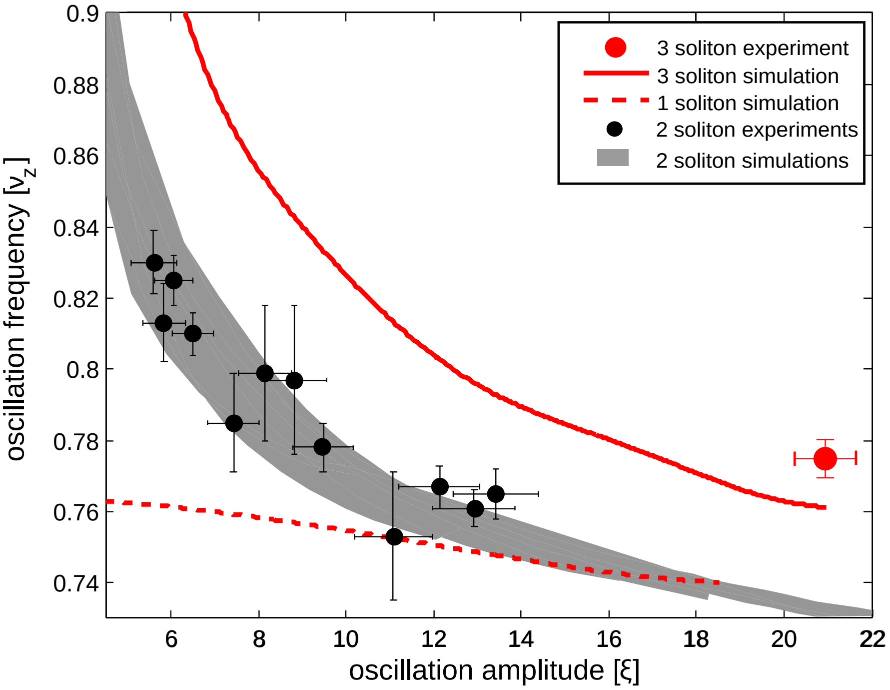

Figure 4.13: Comparison of the three soliton measurement and corresponding single and three soliton NPSE simulation curves to the two soliton results. The single soliton simulation corresponding to the parameters of the three soliton experiment is shown by the dashed line.

4.4 Experimental determination of the velocity and darkness of dark solitons

An important feature of a dark soliton is its propagation through the condensate with a velocity v_d slower than the speed of sound

$$\bar{c}_s = \sqrt{\bar{n}_0 g/m} = \sqrt{n_0 g/2m} \tag{4.3}$$

[Zar1998, Mur2002], with $\bar{n}_0$ the average density of the condensate over its cross-section. As shown in section 2.1.1 the speed of a soliton can take values between zero and the speed of sound[1] and is directly connected to its darkness. Hence, one can estimate the darkness of the soliton $\sqrt{n_d/n_0}$ from the experimental data by measuring the velocity during the collision and using

$$\frac{n_d}{n_0} = 1 - \left(\frac{v_d}{\bar{c}_s}\right)^2 . \tag{4.4}$$

If the speed of the soliton is known it is possible to get an approximation for the oscillation amplitude z_{max} of a soliton oscillating in a harmonic trap by the equation

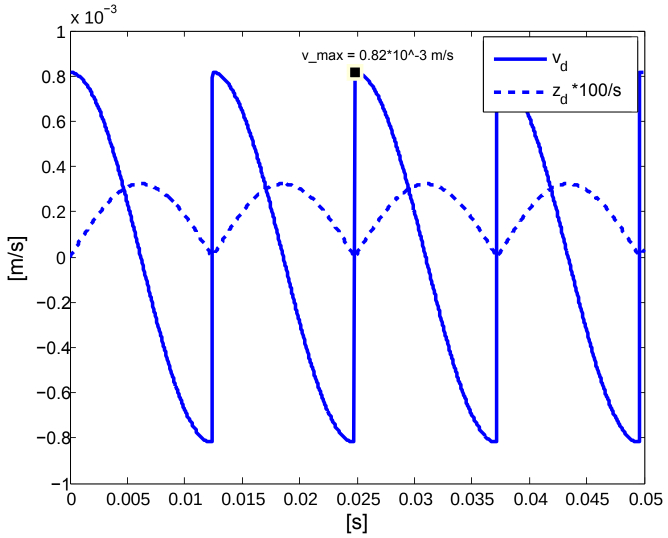

Figure 4.14: Estimation of the soliton velocity during the oscillation and collision dynamics of two solitons in a harmonic trap. The dashed line shows the fitted distance between the two solitons. The solid line represents the velocity of one of the solitons, obtained as the derivative of the fit and dividing by two. $\bar{c}_s$ has been calculated to be $2.1 \cdot 10^{-3} m/s$.

$$z_{max} = \sqrt{2} v_d/\omega_z . \tag{4.5}$$

---

[1] It has been shown in [Zar1998] that a sound wave in an elongated BEC propagates with a speed of $\bar{c}_s = c_s/\sqrt{2}$. So $\bar{c}_s$ is the speed of sound relevant to solitons in an experimental situation [Mur2002]. Whereas the Bogoliubov speed of sound c_s is the critical speed for solitons in an idealized 1D regime described by the homogeneous 1D GPE.

This result was obtained in [Kon2004] by regarding the soliton as a quasiparticle within the framework of the TF approximation. It gives reasonable results in first approximation even for our case of two solitons oscillating in the trap, see table 4.3 and compare with table 4.2.

Knowing the soliton velocity is also interesting, because it enables one to figure out in what regime a collision between two solitons occurs. As discussed in section 2.1.4 it is possible to define a critical velocity $v_d^c = 0.5c_s$, from the analytical approach of [Akh1993, Kev], which separates two regimes. At the critical velocity $v_d^c = 0.5c_s$ the minimal distance $d = 2z_0$ between the two soliton becomes zero during the collision. This behavior can be seen from the following equation (see also section 2.1.4):

$$z_0 = \frac{1}{2\sqrt{n_0 - n_{min}}} \cosh^{-1}\left(\sqrt{\frac{n_0}{n_{min}}} - 2\sqrt{\frac{n_{min}}{n_0}}\right)\xi. \tag{4.6}$$

$n_{min}/n_0 = 1 - n_d/n_0$ denotes the point of minimal density at the density notch and n_0 the background density. $\xi = \hbar/\sqrt{m\mu}$ is the healing length. For our experiments we get $v_d/\bar{c}_s = 0.4 - 0.52$ corresponding to $n_d/n_0 = 0.84 - 0.73$, see table 4.3. This suggests that most of the experiments were performed well in the regime where the minimal distance $2z_0$ is always bigger than zero and the solitons can be regarded as classical repulsive particles. Our NPSE-IS simulations confirm this result. Here we get a density different from zero between the solitons during their collision for all data sets. In our experiments the two solitons collide up to 7 times showing that dark solitons can survive several oscillation periods and collisions. In a recent experiment [Ste2008] a single collision between dark solitons has been observed. The depths of the two colliding solitons were there estimated to be $n_d/n_0 = 0.74$ and 0.69 corresponding to $v_d/\bar{c}_s = 0.51$ and 0.56, respectively.

	Set1	Set2	Set3	Set4	Set5	Set6	Set7	Set8	Set9	Set10	Set11	Set12
$\frac{v_d}{\bar{c}_s}$	0.41	0.40	0.46	0.47	0.44	0.42	0.48	0.50	0.51	0.52	0.43	0.50
$\frac{n_d}{n_0}$	0.84	0.84	0.79	0.78	0.81	0.83	0.77	0.75	0.74	0.73	0.81	0.75
$\frac{z_0}{\mu m}$	0.15	0.16	0.15	0.14	0.18	0.21	0.10	0.04	0	0	0.19	0.04
$\frac{z_{max}}{\mu m}$	3.39	3.48	5.48	4.40	3.69	3.47	3.86	2.96	2.68	2.80	2.34	2.65

Table 4.3: $v_d/\bar{c}_s$ denotes the soliton speed during collisions estimated from the fit of our experimental data. n_d/n_0 is the depth of the soliton notch calculated from the estimated speed. The approach of Ankhmediev and Ankiewicz approximates the minimal distance $2z_0$ during the collision by Eqn. 4.6. Note: In our two soliton NPSE simulations the solitons never overlap during the collision. z_{max} denotes the soliton oscillation amplitudes as estimated from Eqn. 4.5.

4.5 Stability of dark solitons in BECs

4.5.1 The snaking instability

As mentioned in section 3.4 a dark soliton as an actual 1D object is not dynamically stable in a genuinely 3D regime. It will decay through a transverse instability first

discussed for optical solitons by [Kuz1988] and [Kiv1998]. Muryshev et al. investigate the case of standing dark solitons (kink states) in a BEC, explain the decay process and find a condition under which the decay does not occur in elongated condensates [Mur1999]. The authors explain that the kink related kinetic energy $K = -\frac{1}{2}\Psi_d \frac{d^2\Psi_d}{dz^2} \sim \mu$ can be transferred by the inter-particle interaction to unstable transverse modes of the condensate. The inter-particle interaction is characterized by the chemical potential $\mu = n_0 g$, with n_0 the peak density of the condensate and g the interaction constant. In this picture the instability will not occur if the condensate is strongly enough radially confined such that the lowest possible radial excitation exceeds $K \sim \mu$. This leads to the condition: $\hbar\omega_\perp > \mu$.
In an additional more quantitative investigation the authors perform a Bogoliubov-de-Gennes analysis which can be used to find unstable modes of the condensate. These unstable modes exhibit an imaginary eigenfrequency in the Bogoliubov spectrum. The authors start their analysis with the case of no trapping field: $\nu_\perp = 0$ and $\nu_\mathbf{z} = 0$. They show that the unstable modes correspond to transverse wave vectors of $k_\perp = 2\pi/\lambda_\perp < \sqrt{m\mu}/\hbar$. Hence these modes correspond to perturbations with long wavelengths $\lambda_\perp$ in transverse direction of the condensate. If $k_\perp > \sqrt{m\mu}/\hbar$ the transverse modes are stable exhibiting a real eigenfrequency. Therefore, to prevent the instability one finds a similar condition as before. The condensate has to be radially confined such that: $\hbar\omega_\perp > (k_\perp^2\hbar^2)/(2m) = \mu/2$[2]. Due to the confinement the long wavelength modes do not fit into the radial potential.

Based on these findings Muryshev et al. further investigated the case of transversal and longitudinal trapping confinement: $\nu_\perp \neq 0$ and $\nu_\mathbf{z} \neq 0$. They calculate the critical value γ_c of the parameter

$$\gamma = \mu/(\hbar\omega_\perp), \tag{4.7}$$

for which a standing dark soliton is still dynamically stable for various values of $\omega_\perp/\omega_z$ (see Fig. 4.15). For the limit $\omega_\perp \gg \omega_z$ they find $\gamma_c \approx 2.4$. Additionally, we mark the values of γ for different experiments in this figure.

Later on Muryshev et al. [Mur2002] also considered the case of moving dark solitons and pointed out that $r \lesssim L \sim \xi$, with r the radial size of the condensate and L the width of the soliton, is a similar condition for being in the radial non-TF regime [Mur2002]. When the soliton is moving with speed v_d, L is increased and the instability border $r \sim L$ is reached at larger values of $\gamma = \mu/(\hbar w_\perp)$ than in the case of standing solitons. In other words, $w_\perp$ can be smaller. Thus, the stability condition is more relaxed for a moving soliton [Mur2002], see Fig. 4.16. To get an intuitive image of the instability process, one should remember that the local speed of sound $c_s(r) = \sqrt{n_0(r)g/m}$ is density dependent. This means that in the radial TF regime the local velocity of the soliton, which is proportional to the local speed of sound, depends on the radial coordinate, so that the soliton moves faster in the central region

---

[2] This is contrarily connected to the condition $\mu \gg \hbar\omega_\perp$ for being in the Thomas-Fermi (TF) regime for an infinitely long or homogeneous system [Men2002].

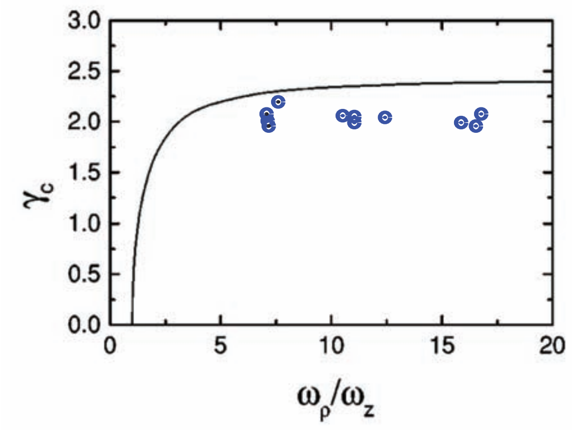

Figure 4.15: Dependence of the critical value γ_c below which standing dark solitons are still dynamically stable vs. $\omega_\perp/\omega_z$. Being the first experiment fulfilling this criterium the values of our measurements are marked by the blue dots. Diagram taken from [Mur1999] and adapted.

than at the edge of the trap and gets bend. The notch velocity increases whereas its depth decreases. Finally the soliton decays into phonon waves [Mur2002] or into a vortex-antivortex pair [Mur1999].

From numerical simulations Muryshev et al. observed that for $\gamma > 10$ imprinted phase kinks always decay, whereas they accelerate and transform into a proper soliton with a flat nodal plane for $\gamma \lesssim 5$ [Mur2002]. The decay of dark solitons into vortex-rings was observed experimentally by [And2001]. Particularly interesting is the recent experiment [Sho2008] observing a periodic soliton/vortex-ring, a soliton which transforms into a vortex-ring and back, for $\gamma = 4.95$.
Our experiments with $\gamma \approx 2$ are the first ones performed in and not only near the dynamically stable regime for all velocities between 0 and $\bar{c}_s$. This explains why we have been able to observe multiple oscillation periods of the solitons. This requires the experiment to fulfill the stability condition for a stationary soliton, because otherwise the solitons will get unstable when they come to rest on their turning point at the oscillation amplitude[3].

4.5.2 Comparison of different experiments

Table 4.4 shows the values of the parameters discussed in this section for different experiments investigating systematic measurements on dark solitons in BECs. The values for these experiments are also marked in Fig. 3.11, 4.15 and 4.16 as far as they fit in the parameter range shown there. The experiment of [Den2000] appears in none of the figures, because it is far away from the parameters that are optimal

---

[3] Note that the stability criterion for a soliton at the position of its oscillation amplitude might slightly differ from the one of a stationary soliton in the center of the trap as the local density is different there.

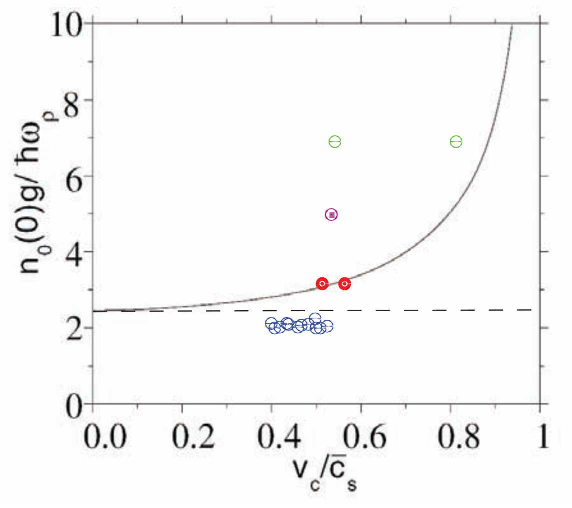

Figure 4.16: For a moving soliton the criterium for dynamical stability γ_c is more relaxed. The limit for standing solitons is given by the dashed line. v_c denotes the speed of the soliton here. Different experiments are marked by the dots. green: Burger et al. [Bur1999], magenta: Shomroni et al. [Sho2008], red: Stellmer et al. [Ste2008], blue: our experiments. Diagramm taken from [Mur2002] and adapted.

for the stability of dark solitons. The most important is the parameter $\mu/(\hbar\omega_\perp)$ (second column), describing the dynamic stability of dark solitons as discussed in section 4.5.1, and the parameter $N\Omega a_s/a_\perp$ (third column) describing the optimal dimensionality regime for dark solitons as discussed in section 3.4. The later is also related to the stability parameter. It becomes obvious that decreasing the aspect ratio of the trap Ω is not enough to get into a dynamically stable regime. Besides this the atom number has to be small enough to really fulfill the stability criteria, because it influences the dimensionality of the system as well. Note that the dissipative decay constant discussed in section 4.5.3 is not shown in table 4.4, because the temperature is not given in most articles as it is hard to estimate. An estimation of the decay time for our experiment is discussed in section 4.5.3.

4.5.3 Dissipative instability

Under the condition of dynamic stability the dark soliton is perfectly stable at $T = 0$. However, as every experiment is performed at finite temperature dissipative instabilities induced by thermal excitations will occur. To address these effects Fedichev et al. have developed a model using a Fokker-Planck approach [Fed1999, Lif1995] where they regard the dark soliton as a heavy particle in a gas of light particles. The approach describes the probability density of the particle position under the interplay of a diffusive force and a friction force transferring momentum from thermal excitations to the moving kink.

A dark soliton is an excited state with a local energy extremum. Its energy is the higher the slower the soliton is. Thermal excitations scattered by the kink can stimulate its diffusive motion and increase its mean velocity. This induces a dissipative

	Ω	$\mu/(\hbar\omega_\perp)$	$N\Omega a_s/a_\perp$	$\left(\frac{N}{\sqrt{\Omega}}\frac{a_s}{a_\perp}\right)^{1/3}$
Set 1	0.061	1.96	1.22	4.35
Set 2	0.060	2.07	1.50	4.69
Set 3	0.063	1.99	1.31	4.35
Set 4	0.081	2.04	1.42	3.95
Set 5	0.091	2.05	1.45	3.76
Set 6	0.091	1.99	1.30	3.62
Set 7	0.096	2.06	1.46	3.67
Set 8	0.133	2.19	1.81	3.35
Set 9	0.142	1.95	1.22	2.84
Set 10	0.142	2.00	1.33	2.92
Set 11	0.142	2.07	1.49	3.03
Set 12	0.140	1.95	1.21	2.85
Burger et al. [Bur1999]	0.033	6.86	50.24	20.33
Denschlag et al. [Den2000]	1.414	22.83	870.37	8.03
Shomroni et al. [Sho2008]	0.111	4.95	17.78	7.83
Stellmer et al. [Ste2008, Bec2008]	0.044	3.13	12.62	11.05

Table 4.4: Parameters relevant for the dynamical stability of dark solitons. Set 1 to Set 12 denote our measurements.

force proportional to the speed of the kink, which soon exceeds the diffusion and accelerates the kink to the speed of sound [Fed1999]. During this process the soliton state continuously transforms to the ground state of the BEC. This can be understood by regarding the expression for the energy of the kink state given in [Fed1999]: $H(\dot{z}) = \frac{1}{3}Mc_s^2\left(1-\frac{\dot{z}^2}{c_s^2}\right)^{3/2}$, with $M = 4(n_0 S\xi)m \gg m$. $-M$ can be treated as the negative mass of the kink and S is the transverse cross section of the BEC. If the kink energy is decreased by dissipation, the kink accelerates in a run-away process, because its dynamic mass $-M\left(1-\frac{\dot{z}^2}{c_s^2}\right)^{1/2}$ [Fed1999] gets smaller and smaller. In contrast to a realistic particle, where an infinite force would be necessary to accelerate its increasing mass to the speed of light, the soliton kink reaches the speed of sound and the system has decayed to the ground state of the condensate.
From their Fokker-Planck model Fedichev et al. [Fed1999] can estimate the following expressions for the diffusion time τ_D and the lifetime of the dark soliton τ for the case $k_BT \ll \mu$:

$$\begin{aligned}
\tau_D^{-1} &= 24\zeta(4)\omega_\perp(\pi n_0 a^3)^{1/2}\left(\frac{T}{\mu}\right)^4, && (4.8)\\
\tau^{-1} &= 2\tau_D^{-1}\ln^{-1}[M\mu/(mT)]. && (4.9)
\end{aligned}$$

In first approximation it can be said that the ratio of the thermal energy to the chemical potential should be $k_BT/\mu \ll 1$ to minimize thermal excitations. For our experiments we estimate the temperature to be $T = 10-20\,\mathrm{nK}$ by the method of [GatII2006]. The case of $T = 10\,\mathrm{nK}$ gives for our parameter sets with $\nu_\perp = 890\,\mathrm{Hz}$:

$k_BT/\mu \approx 0.1$ and $\tau \approx 12\,\mathrm{s}$; and for the sets with $\nu_\perp = 408\,\mathrm{Hz}$: $k_BT/\mu \approx 0.25$ and $\tau \approx 1.5\,\mathrm{s}$. The case of $t = 20\,\mathrm{nK}$ yields $k_BT/\mu \approx 0.25$, $\tau \approx 0.5\,\mathrm{s}$ and $k_BT/\mu \approx 0.5$, $\tau \approx 0.1\,\mathrm{s}$.
From Eqn. 4.9 the decay of the soliton contrast $C = 1 - v_d^2/\bar{c}_s^2$ from the initial value C_0 to C_0/e can be calculated from the relation

$$\begin{aligned}\tau_c = (0.47\ln((1 - C_0/e)/(C_0/e))/\ln(10) - \\ 0.47\ln((1 - C_0)/C_0)/\ln(10))\tau. \qquad (4.10)\end{aligned}$$

This relation has been obtained numerically in [Mur2002]. Note that it is not valid for $v \approx 0$. The soliton contrast C equals the expression n_d/n of section 2.1.1. A preliminary measurement is discussed in section 4.5.4.

4.5.4 Soliton decay in our experiment

As discussed in section 4.5.1 the solitons in our experiments obey all conditions for dynamic stability. The only decay which can still occur is the dissipative decay induced by thermal excitations which is due to the finite temperature of the experiment. As we have seen in section 4.5.3 this decay depends strongly on the ratio k_BT/μ. The rough estimation of the temperature to $T = 10 - 20nK$ provides a decay time of the order of $0.1s$ to $12s$ for our measurements. This decay time has to be observed carefully in the experiment, because it is masked by other decay effects.

Effects masking the real soliton decay in experimental images

We will show in the following why it is more sufficient to determine the experimental decay of the solitons from single shots of the experiment and not from averaged pictures.

Our analysis reveals, that for single shots of the experiment the observed loss of soliton contrast for the timescale of the measurements of 80 ms can be explained quite well by one effect alone. This effect is the convolution of the pictures due to the imaging process. As an example we observe the measurement corresponding to data set 2 (see table 4.1). We investigate this effect by simulating the experimental situation by means of the $3D$ GPE. In the simulation we see that additionally created low contrast solitons whose number seems to increase during the subsequent collisions get out of phase of the two dominating oscillating solitons. This adds noise to the dominating solitons (see Fig. 4.3b). Now applying the finite spatial as well as the temporal resolution of our imaging system to the 3D GPE evolution plot reproduces the experimentally observed loss of contrast on the time scale of 80 ms, see Fig. 4.17, 4.3c. In our example the effect seems to stop increasing further by the end of the experimentally observed timescale of 80 ms.

If in contrast averaged pictures are observed, as we did for obtaining the time evolution plots (e.g Fig. 4.3a), additional effects smear out the soliton contrast in these

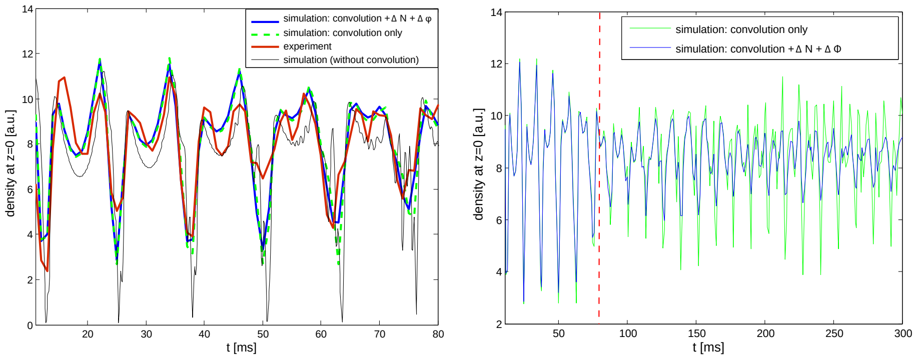

Figure 4.17: **left**: Loss of contrast of the collision point of the solitons at $z = 0$ during the time evolution. Additionally created weak solitons cross the two dominating ones and add noise to them (see also Fig. 4.3). The density at $z = 0$ during the time evolution is plotted. Black line: $3D$ GPE simulation, blue line: mean over 10 3D GPE simulations taking randomly into account a standard deviation of $\Delta N/N \approx 0.15$ and $\Delta\phi/(2\pi) = 0.07$ plus the spatial $(1\,\mu\mathrm{m})$ and temporal $(1\,\mathrm{ms})$ convolution of the imaging system, green dashed line: 3D GPE simulation plus convolution, red line: experimentally observed density. As the blue and the green dashed line do not deviate much from each other the given standard deviation of the experimental parameters does not seem to be a limiting factor. **right**: simulation for a longer evolution time of $300\,\mathrm{ms}$, the evolution time of the experiment is marked by the dashed red line. blue line and green line: same as before, but for longer evolution time. On longer timescales the slightly varying starting conditions of the experiment indeed lead to a further decrease of the contrast of averaged images. Parameters: $\nu_z = 53\,\mathrm{Hz}$, $\nu_\perp = 890\,\mathrm{Hz}$ and $N = 1700$ (parameter set 2) corresponding to Fig. 4.3a.

images. First of all the frequency of the solitons can vary from shot to shot, because of slightly different starting conditions of the experiment. This smears out the contrast of averaged images especially at long evolution times. Dominating here are the variation of the atom number which has a standard deviation of $\Delta N/N \approx 0.15$ and the noise on the initial phase which we determine to be $\Delta\phi/(2\pi) = 0.06$. Checking the decrease of soliton contrast at the coordinate $z = 0$ for the parameter set of data set 2 (see table 4.1) of our experiments we discover that this effect does not dominate the loss of soliton contrast for the observed timescale of the experiment of $80\,\mathrm{ms}$ as can be seen in Fig. 4.17(left). But for longer evolution times this effect indeed leads to a further decay of the soliton contrast as can be seen in the blue curve of Fig. 4.17(right).
Furthermore, due to the thermally induced decay the solitons will accelerate in a process of statistic nature, which would even smear out the averaged images additionally. Note, if averaging too many images per point of the time evolution, also a long term shift of the double well potential as discussed in section 5.3 might get relevant for the contrast decay of the averaged time evolution plots.

To emphasize again all these effects only lead to a technical loss of contrast of the two solitons of interest in the images. They are not a real decay of the solitons.

Temperature induced decay

We have performed a *preliminary* measurement observing the temperature induced decay (see section 4.5.3) of two[4] oscillating solitons for 200 ms with a time step of 2 ms. We determine the depth of the solitons *in single shots* of the experiment on selected points during the evolution at which the two solitons meet in the center of the trap. The contrast is determined by measuring the maximum and the minimum of the soliton notch manually in the density profiles. We drop shots where it is not possible to detect the soliton notch properly. This investigation results in Fig. 4.18. We can determine a reasonable decay time of the soliton contrast of $\tau_c = 178 \pm 44\,\mathrm{ms}$ by fitting our experimental data. The given error is the standard deviation of a least square fit. Taking the experimental parameters $\nu_z = 57\,\mathrm{Hz}$, $\nu_\perp = 408\,\mathrm{Hz}$, $N = 870$ and $C = n_d/n_0 = 0.74$ into account and assuming a reasonable temperature range of $T = 10 - 20\,\mathrm{nK}$ ($k_B T/\mu = 0.26 - 0.51$) Eqn. 4.10 results in $\tau_c = 576 - 34\,\mathrm{ms}$ which is on the same order of magnitude for τ_c as the experimental observation. (Assuming $T = 13\,\mathrm{nK}$ would yield $\tau_c = 193\,\mathrm{ms}$.) If the above mentioned decay effect due to the imaging convolution (all other discussed effects are prevented by using single shots) is involved the real decay time might be longer than the experimentally observed one. Therefore we can assume the measured time constant as a lower limit of the decay time τ_c in our experiment, so that: $\tau_c \geq 178 \pm 44\,\mathrm{ms}$. Note that this lifetime

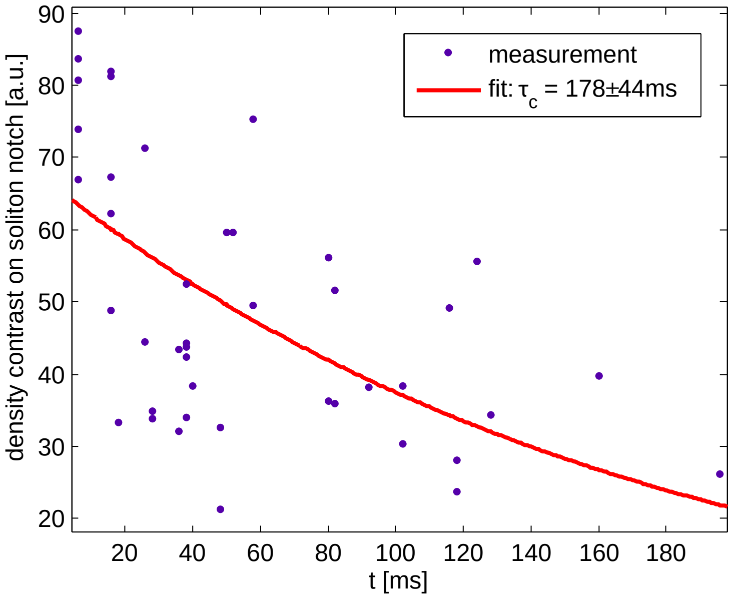

Figure 4.18: Soliton decay observed from single shots of the experiment. It can be seen that for longer evolution times not in every image a soliton can be assigned due to increasing noise.

---

[4] Note: To exclude possible dissipative effects due to the soliton collisions it might be more appropriate to observe single solitons instead of two.

is one of the shortest among our parameter sets. For one set for example we get $k_B T/\mu = 0.15$ expecting a lifetime of $2.4\,\mathrm{s}$ at $T = 13\,\mathrm{nK}$. In selected single shots of the experiment we have detected solitons after $t \approx 1\,\mathrm{s}$.

In conclusion, our measurements have revealed the inter-soliton interaction experimentally and have confirmed theoretical predictions of the oscillation frequency of dark solitons. Furthermore we have discussed that our created solitons are dynamically stable and should therefore decay due to temperature induced effects.

Chapter 5

Experimental setup

The following chapter will describe the experimental apparatus producing our BEC of ^{87}Rb atoms. We will focus on the 'next generation' changes to the setup, which have been carried out during the time of this thesis. These are especially the stabilization of the optical dipole traps as well as of the optical lattice and the installation of a new imaging system. We will start with a short description of the entire setup. A detailed description of the construction of the apparatus from scratch can be found in [Eie2004] and the first realization of the optical double well potential in [Alb2005].

5.1 General description of the setup

For the first time achieved less than 15 years ago and later awarded with the noble price of physics, the creation of Bose-Einstein Condensates of dilute atomic gases [And1995, Dav1995] has nowadays become a standard tool in atomic physics. We use an established three step technique to achieve Bose-Einstein condensation. We start by precooling ^{87}Rb atoms in a magneto-optical trap (MOT), perform further cooling in a magnetic trap and subsequently we cool the atoms below the critical temperature for Bose-Einstein condensation in an optical dipole trap. Our experimental setup (see Fig. 5.2) can be roughly separated into two parts. The first part is the area containing the vacuum chamber (denoted as 'darkened area' in Fig. 5.2) which is necessary to prepare the ultra cold atoms in a UHV environment. The second part is the laser system, which prepares narrow-line-width light at appropriately near detuning from an atomic transition as needed for laser cooling and imaging the atomic density distribution and far-detuned light for the optical dipole traps.

5.1.1 The vacuum chamber

The vacuum chamber (see Fig. 5.1) is separated into two parts by a differential pumping stage, a high vacuum (HV) chamber at a pressure of $p \approx 10^{-8}$ mbar and an ultra high vacuum (UHV) chamber at $p < 10^{-11}$ mbar. This separation is necessary to decouple the atom source and the experimental chamber where an UHV is needed to obtain a BEC. In the HV chamber the atoms are evaporated from Rubidium dispensers and precooled and collimated by a $2D+$ MOT, also called funnel [Eie2004]. The funnel exhibits two pairs of balanced counter-propagating laser beams in the transversal axes and a non-balanced pair of laser beams in the longitudinal axis. In this axis one of the beams is set to have higher intensity than the other one pushing the atoms in a slow collimated beam towards the UHV chamber. The UHV chamber provides the experimental chamber with a standard 3D MOT (see [Eie2004, Ank2005, Raa1987] for details), a magnetic time-orbiting-potential (TOP) trap and the optical dipole traps. The UHV at $p < 10^{-11}$ mbar is necessary to prevent collisions of the cooled atoms with the background gas. After precooling in the MOT on the $(F = 2 \rightarrow F' = 3)$ cycling transition the atoms are optically pumped into the $5^2S_{1/2}|F = 2, m_F = 2\rangle$ state and transferred into the TOP trap for further cooling. The TOP trap (see [Eie2004, Alb2005, Pet1995] for details) consists of a magnetic quadrupole trap whose zero-point is rotated by magnetic bias fields at a frequency of 10 kHz. This prevents the atoms from changing their spin state at the zero-point of the field and from escaping the trap. Finally, the atoms are evaporatively cooled in a far-detuned crossed optical dipole trap. This is done by decreasing the intensity of the laser beams providing the trap for a certain time, resulting in a lowered trap depth so that hot atoms can escape.

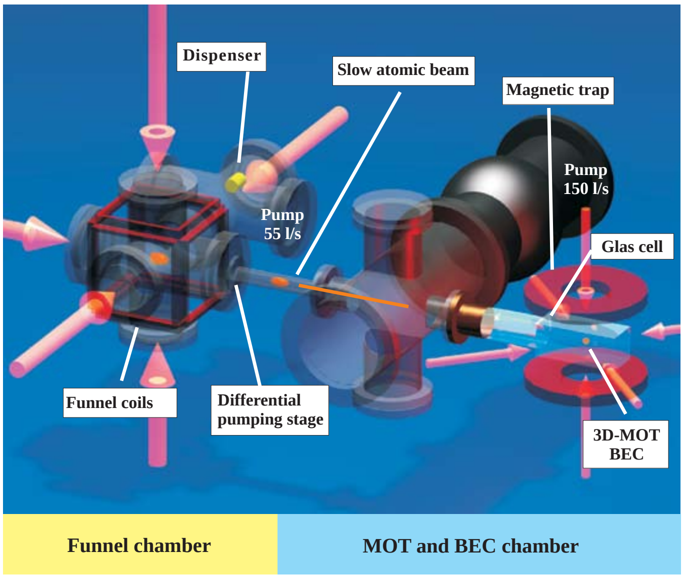

Figure 5.1: The vacuum system. The BEC chamber where the experiments are performed is located on the very right side.

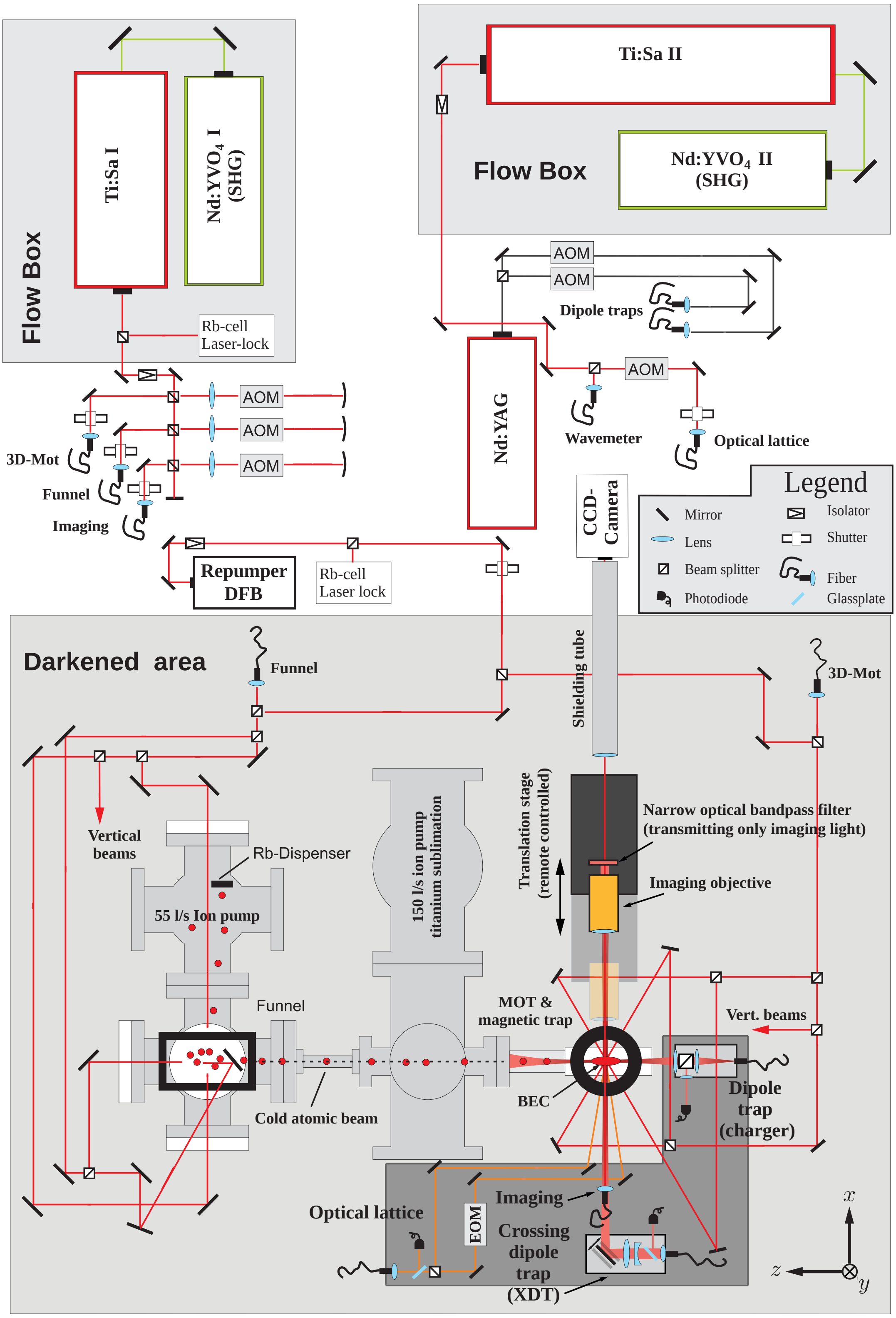

Figure 5.2: Experimental apparatus. Details see text. The L-shaped dark grey shaded area marks the aluminum block mechanically connecting the dipole traps and the optical lattice interferometer. Note that the optical lattice interferometer is actually placed below the Xdt, which is shown here differently due to simplification. The new imaging system is discussed in section 5.4.

5.1.2 The laser system

The light provided by the different lasers (except for the repumper) is coupled to optical single-mode fibres and delivered directly at the vacuum chamber. Another advantage of optical single-mode fibres is their transversal mode cleaning as only the TEM-00 mode can be coupled into these fibers. In total we operate four different lasers. The lasers Ti:Sa I and the repumper are frequency-locked by means of doppler-free absorption spectroscopy of Rubidium vapor.

Ti:Sa I This is a Titanium-Saphire (Ti:Sa) laser (Coherent, Monolitic-Block-Resonator 110) with an optical output power of $\approx 1.2\,\mathrm{W}$ (after optical isolator) and a line width of $\Delta\nu = 100\,\mathrm{kHz}$. This narrow line width is reached by the combination of an etalon lock with an external cavity lock. The Ti:Sa I is pumped by an frequency doubled Nd:YVO$_4$ laser (Coherent, Verdi V10) with an output power of 10 W. We lock this laser to the $(F = 2 \rightarrow F' = (3,1))$ transition crossover of the ^{87}Rb D_2 line near a wavelength of 780 nm (see C.1). The beam is split into three paths: magneto-optical trap (MOT), funnel and imaging. In each of the paths the laser light is shifted about 210 MHz, by means of acousto-optical modulators (AOMs) in double pass configuration, towards the $(F = 2 \rightarrow F' = 3)$ cycling transition. We keep a sufficiently small detuning for funnel and MOT and match the transition frequency for the imaging beam.

TiSa II The second Titanium-Saphire laser (Coherent, 899) delivers the light for the optical lattice. It has been operated at a wavelength of $843nm$ for the dark soliton experiments with an output power of $\approx 1.1\,\mathrm{W}$.

Repumper The repumper recollects atoms of the MOT and the funnel which have decayed to the $|5^2S_{1/2}, F = 1\rangle$ state. Although this is unlikely for a single event it is very important in a MOT because of the high number of transition processes during the lifetime of the MOT. For this purpose a Distributed-Feedback diode laser (Toptica, LD-0780-0080-DFB-1) is used, which is locked to the $(F = 1 \rightarrow F' = 2)$ transition of the D_2 line and has a line width of about 4 MHz at an output power of $\approx 25\,\mathrm{mW}$.

YAG A diode pumped Nd:YAG laser (Spectra-Physics, T40-X30-106QW) with a wavelength of 1064 nm operated at an output power of about 3 W provides the light for the far red-detuned optical dipole trap beams.

5.2 Optical dipole traps

5.2.1 The light shift potential

Before discussing the ultra stable reconstruction of the optical dipole traps and the optical lattice, we will give a short introduction to optical light shift potentials.
The interaction of a light field with an idealized two-level atom can be derived in a

semiclassical description using the steady-state solutions of the optical Bloch equations [Met1999]. The resulting force can be separated into two parts, a conservative force and a velocity dependent dissipative one. The dissipative force also called the 'radiation pressure force' allows for the different laser cooling techniques as it slows down the atoms. The conservative force, the 'dipole force' occurs in light fields with spatially varying intensity. It corresponds to an optical trapping potential for atoms [Met1999]:

$$V_{dip}(\mathbf{r}) = \frac{\hbar\delta}{2} \ln\left(1 + \frac{I(\mathbf{r})/I_s}{1 + (2\delta/\Gamma)^2}\right), \tag{5.1}$$

with the saturation intensity $I_s = \hbar\Gamma\omega_0^3/(12\pi c^2)$, $I(\mathbf{r})$ the local light intensity, Γ the natural line width of the transition and c the speed of light. The depth of this potential depends on the detuning $\delta = \omega_l - \omega_0$ of the laser frequency ω_l from the optical transition frequency ω_0. In the case of large detuning, $I(\mathbf{r})/I_s \ll 1 + (2\delta/\Gamma)^2$ and $\delta^2 \gg \Gamma^2$, the potential can be approximated by:

$$V_{dip}(\mathbf{r}) \approx \frac{\hbar\Gamma^2 I(\mathbf{r})}{8\delta I_s}. \tag{5.2}$$

In the limit of $\Omega \ll |\delta|$ Eqn. 5.2 can also be calculated directly from the coupling of a two-level atom to a light field, which is given by the Rabi frequency $\Omega(\mathbf{r}) = \Gamma^2 I(\mathbf{r})/(2I_s)$. The resulting shift $\Delta E(\mathbf{r}) = \hbar\Omega^2/(4\delta)$ of the atomic energy levels equals Eqn. 5.2 and is referred to as the light shift or ac-stark shift. The resulting force $F_{dip} = -\nabla V_{dip}$ drives the atoms to the intensity maximum of a light beam if $\delta < 0$ (red-detuned) and repels them out of the beam if $\delta > 0$ (blue-detuned).

For setting the optimal trapping frequency of a red-detuned light beam, also the rate of spontaneous emission due to the absorption of photons from the light field has to be taken into account. The spontaneous emission of photons leads to heating of the atoms and should be as small as possible. The spontaneous emission rate can be calculated to be [Met1999]:

$$\Gamma_{sp} = \frac{\Gamma I(\mathbf{r})/(2I_s)}{1 + I(\mathbf{r})/I_s + (2\delta/\Gamma)^2} \approx \frac{\Gamma^3 I(\mathbf{r})}{8\delta^2 I_s} \tag{5.3}$$

The approximation on the right hand side of Eqn. 5.3 is valid in the same limit as Eqn. 5.2. The compromise of a strong trapping force, which is $\propto \delta^{-1}$ and a low spontaneous emission rate which is $\propto \delta^{-2}$ lies in the far red-detuned range.

5.2.2 Trapping potential of a Gaussian laser beam

Optical dipole traps can be realized by laser beams. For a Gaussian beam of the TEM-00 mode, the intensity profile takes the form:

$$I(\mathbf{r}) = \frac{I_0}{1 + (z/z_0)^2} \exp\left(-2\frac{x^2 + y^2}{\sigma_0^2(1 + (z/z_0)^2)}\right) \quad \text{WITH} \quad z_0 = \frac{\pi\sigma_0^2}{\lambda_l}, \tag{5.4}$$

the Rayleigh range. On the length scale of z_0 the light intensity decays in longitudinal direction from I_0, the peak intensity of the beam, to $I_0/2$. λ_l denotes the laser wavelength and σ_0 the beam waist, which corresponds to the length scale on which the intensity decays transversally to $1/e^2$ of its maximum value I_0. Combining Eqn. 5.4 and Eqn. 5.2 leads to the light shift potential of a Gaussian beam optical dipole trap. This Gaussian potential can be approximated in its central region by a three-dimensional harmonic potential. In the case of large detunings $\delta^2/\Gamma^2 \gg I/I_s$, one gets

$$\begin{aligned} V_{harm}(\mathbf{r}) &= V_0 - \frac{1}{2}m\omega_z^2 z^2 - \frac{1}{2}m(\omega_x^2 x^2 + \omega_y^2 y^2), \quad \text{WITH} \qquad (5.5) \\ V_0 &= \frac{\hbar\Gamma^2 I_0}{8\delta I_s}. \qquad (5.6) \end{aligned}$$

The corresponding transversal and longitudinal trap frequencies are given by:

$$\omega_{x,y} = \sqrt{\frac{4|V_0|}{m\sigma_0^2}} \quad \text{AND} \quad \omega_z = \sqrt{\frac{2|V_0|}{m z_0^2}} = \omega_{x,y}\frac{\lambda_l}{\sqrt{2}\pi\sigma_0}. \qquad (5.7)$$

From Eqn. 5.7 we see that if the laser wavelength is much smaller than the beam waist $\lambda \ll \sigma_0$ the longitudinal confinement is very weak. If more than one atomic transition is of relevance, the dipole potentials stemming from all of these transitions have to be summed up. In our case of ^{87}Rb atoms in the $5^2S_{1/2}$ $|F = 2, m_F = 2\rangle$ state, the atoms can be excited to the states $5^2P_{1/2}$ $|F = 2, m_F = 2\rangle$ (D_1 line), $5^2P_{3/2}$ $|F = 2, m_F = 2\rangle$ (D_2 line) and $5^2P_{3/2}$ $|F = 3, m_F = 2\rangle$ (D_2 line) assuming linear polarized light. Hence, all of these lines have to be regarded, resulting in the following estimation:

$$V_{dip}(\mathbf{r}) = V_0\left(\frac{2}{3\delta_2} + \frac{1}{3\delta_1}\right). \qquad (5.8)$$

δ_1 and δ_2 denote the detunings to the D_1 and D_2 line respectively. The prefactors denote the corresponding Clebsch-Gordon coefficients, which are approximated to be 1/3 for each transition in our estimation.

Gravitational sag

As additionally gravity (considered to be in y direction) pulls down the atoms in an atomic trap, there is a balance between this force and the spring-like force of the trap: $mg = ky = \omega_y^2 m \cdot \Delta y$. This results in a shift of the atoms in direction of gravity: $\Delta y = g/\omega_y^2$. Hence, the trap frequency must be chosen such that $\Delta y \lesssim \sigma_0$ with σ_0 the Gaussian beam waist. out of the trap.

5.2.3 1D optical lattices

A one-dimensional optical lattice can be realized interfering two counter propagating far-detuned laser beams. This configuration results in an optical standing wave. As the light intensity varies from zero at a node to its maximum value at an antinode, the optical light shift potential is modulated on a length scale of $\lambda/4$. The so-called lattice spacing $L = \lambda/2$ denotes the distance between two intensity maxima. This offers the possibility to confine atoms in sub-micrometer regions of space [Met1999]. By letting the two laser beams cross under a certain angle θ between them it is also possible to create optical lattices with larger lattice spacing without exchanging the laser. In this configuration only the transverse (for $\theta < 90°$) components of the wave-vectors of the two beams contribute. The resulting intensity pattern and lattice spacing can be calculated as follows. We assume that the transverse size of the two crossing beams is much larger than the wavelength $\sigma_0 \gg \lambda_l$ and can therefore approximate the interference pattern in the central region as a superposition of two plane waves. Furthermore we assume the beams to be of equal intensity and equal frequency $\omega_l = \omega_1 = \omega_2$, $|\boldsymbol{k}| = |\boldsymbol{k}_1| = |\boldsymbol{k}_2|$. Thus the electric field can be described by

$$E = E_0(\cos(\omega_l t + \boldsymbol{k}_1 \boldsymbol{r}) + \cos(\omega_l t + \boldsymbol{k}_2 \boldsymbol{r} + \phi)). \tag{5.9}$$

Considering the transverse components of the wave vectors $k_{1\perp} = |\boldsymbol{k}| \sin(\theta/2)$ and $k_{2\perp} = -|\boldsymbol{k}| \sin(\theta/2)$ we get:

$$E = 2E_0 \cos(\omega_l t + \phi/2) \cos(|\boldsymbol{k}| \sin(\theta/2) z - \phi/2) \tag{5.10}$$

The trapping potential V_{OL} is proportional to the intensity I (see Eqn. 5.2), i.e. $V_{OL} \propto I \propto E^2$, which leads to:

$$V_{OL} = V_0 \left(1 + \cos\left(\frac{2\pi}{L} z - \phi\right)\right) \tag{5.11}$$

with the resulting lattice spacing

$$L = \frac{\lambda_l}{2\sin(\theta/2)}. \tag{5.12}$$

By Taylor expansion of Eqn. 5.11 we get $V \approx V_0 - \frac{1}{4} V_0 (2\pi/L)^2 z^2$ whereas we get $V \approx V_0 - \frac{1}{2} m\omega_z^2 z^2$ from Eqn. 5.6. Equating both expressions and solving to V_0 leads to:

$$V_0 = \frac{m\omega_z^2 L^2}{2\pi^2}, \tag{5.13}$$

which denotes the height of the optical lattice.

5.3 Next generation ultra stable optical dipole traps and optical lattice interferometer

We use a crossed optical dipole trap configuration consisting of the 'charger' (see section 5.3.1) and the 'Xdt' (see section 5.3.2) beam, which meet under an angle of 90°. Additionally we have the possibility to overlap a 1D optical lattice (see section 5.3.3) with that trap.

The light intensity of our optical dipole traps is set by acousto-optic modulators (AOM). An established method of stabilizing these traps is the active stabilization of the beam intensities by means of feedback control [Alb2005, Gat2006]. Reflections of the main beams detected by photodiodes serve as input in the feedback loops. Additionally the laser light is coupled to optical fibres and directly delivered close to the experimental chamber. As few optical components as possible are used after the fibre outcouplers to prevent drifts of the beams. We have now performed measurements where this high stability of the experiment was indispensable on a time scale of many hours. Therefore the stability of the experiment has been further improved. Special attention had to be paid to the relative stability of the two optical dipole traps and the optical lattice. The building of a quasi drift free setup (see Fig. 5.3) which connects all of these three components was a crucial point for both experiments [Est2008, Wel2008] performed during the time of this thesis. Therefore

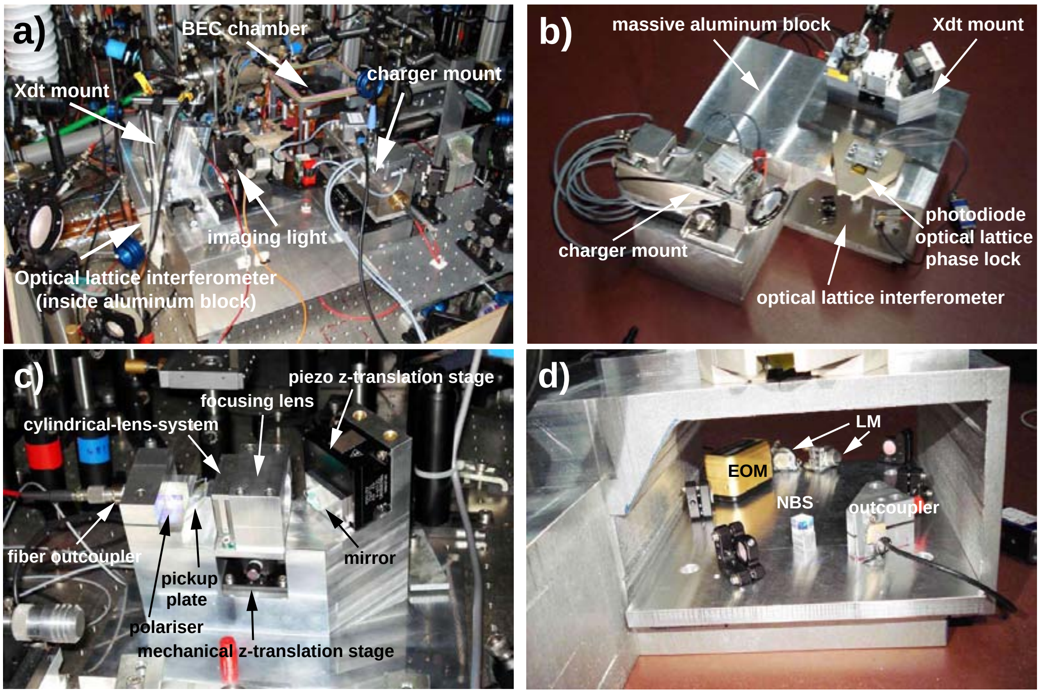

Figure 5.3: Ultra stable optical dipole trap and optical lattice setup. a) Setup integrated in the experiment. b) All parts put together after construction c) The Xdt mount. d) The optical lattice interferometer is integrated in a hole inside the massive aluminum block. NBS denotes the non-polarizing beam splitter and LM the two last mirrors directing the lattice beams to the BEC.

the fibre outcouplers of both beams of the crossed optical dipole trap have been fixed in massive aluminum mounts. All necessary optical components have been placed on the same mounts to minimize the relative movement between them. The first beam of the optical dipole trap (called 'charger') and its mount have already been characterized in [App2007]. The second beam, the crossing dipole trap (called 'Xdt') will be discussed in section 5.3.2. As we have in total four different beams ('charger', 'Xdt' and the two beams of the optical lattice) which have to overlap without drifts the key to the stability of this setup was their connection via a massive aluminum block with a mass of $\approx 40\,\mathrm{kg}$. Therefore, also the interferometer producing the optical lattice

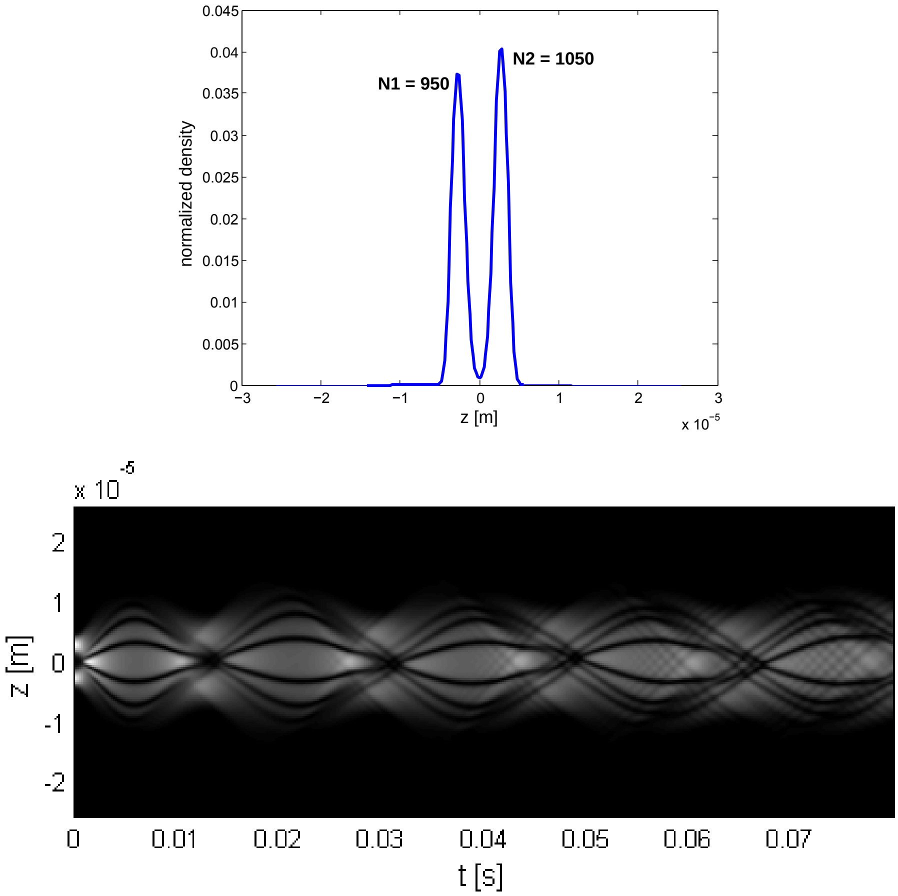

Figure 5.4: Tolerance of the double well symmetry. **top**: The change of the atom number imbalance of the left and write well $\Delta N = |N1 - N2|/(N1 + N2)$ during a measurement series of $\approx 10\,\mathrm{h}$ was checked to be typically 5%. This corresponds to a relative spatial instability between the dipole traps and the optical lattice of $\Delta z \approx 250\,\mathrm{nm}$ on this timescale. **bottom**: A spatial shift between dipole traps and optical lattice of $\Delta z = 250\,\mathrm{nm}$ leads to a small change in the symmetry of the evolution dynamics of dark solitons produced by matter wave interference.

had to be rebuilt (see section 5.3.3) to be placed into a hole inside of this aluminum block. The aluminum block is placed on the optical table on three steel balls and has no other connection to the table. This minimizes heat transfer between the block and the table. For the material we chose cast and annealed aluminum because it has little tension and exhibits only the natural coefficient of expansion of aluminum. Still this coefficient of expansion is quite high with $\alpha = 23 \cdot 10^{-}6K^{-1}$ at $20°C$. For the dark soliton experiments we set ourselves the limit that the imbalance of the atom number between both wells ΔN of the initial double well potential should be $\Delta N = |N1 - N2|/(N1 + N2) < 10\%$ during the whole measurement series, with $N1$ and $N2$ the atom number in the left and right well respectively. Otherwise the time evolution pattern of the created dark solitons would change with time in an unacceptable way. After every experimental run of $\approx 10\,\mathrm{h}$ duration ΔN was checked and was found to be typically $\Delta N \approx 5\%$. This corresponds to a stability in relative position of the optical dipole traps and the optical lattice beams of $\Delta z \approx 250nm$ resulting in a small possible shift of the symmetry of the double well potential as illustrated in Fig. 5.4. The limit of $\Delta N = 10\%$ was never exceeded.

Regarding the coefficient of expansion of aluminum this stability of $\Delta z \approx 250\,\mathrm{nm}$ corresponds to a temperature stability of the block of $\Delta T = 0.025\,\mathrm{K}$. These conditions are mainly achieved passively in our case by letting the experimental apparatus run on the measurement cycle for $\approx 10\,\mathrm{h}$. After that time the machine has reached its equilibrium temperature, so that the optical dipole trap configuration is quasi drift-free. We can then let the apparatus automatically run on its measurement cycle for $\approx 10\,\mathrm{h}$ without the need of adjustment. As evidences for this stability we show in Fig. 5.16 two long term measurements of the symmetry of our BEC in the double well potential and of the interference pattern of the two BECs out of this potential in time of flight.

5.3.1 The optical dipole trap - 'charger'

The charger has been characterized in [App2007]. It consists of a tightly focused far-detuned ($\lambda = 1064\,\mathrm{nm}$) laser beam with a Gaussian waist of $\sigma_0 = 5\,\mu\mathrm{m}$. The achievable trap frequencies lie in the range of $\nu_\perp = 400 - 1000\,\mathrm{Hz}$ corresponding to a beam power of $\approx 1 - 6\,\mathrm{mW}$. As the beam waist of the charger is small it exhibits a considerable trapping confinement in the longitudinal direction (see Eqn. 5.7), which we determined to be $\nu_z \approx \nu_\perp/20 = 20 - 50\,\mathrm{Hz}$. Therefore the charger can trap the BEC without the need of additional confinement. Like every atom trap the charger has a principle lower limit of its achievable trap frequencies via the gravitational sag $\Delta y = g/\omega_y^2$ (see Fig. 5.5). This phenomenon limits the trap depth E_{depth} and results in an experimentally observed minimal trap frequency of $\nu_\perp \approx 350\,\mathrm{Hz}$. The trap depth is also connected to the maximal temperature $T_{max} = E_{depth}/k_B$ of the atoms that can be trapped by the charger. For the starting value in the dark soliton experiments of $\nu_\perp = 408 \pm 41\,\mathrm{Hz}$ we estimate the temperature to $T = 10 - 20\,\mathrm{nK}$ using the method of [Gat2006], which should be close to the trap depth.

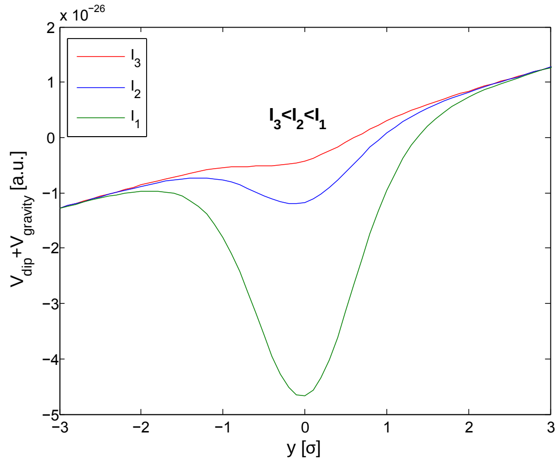

Figure 5.5: Illustrating the trap depth including gravity. Decreasing the trapping frequency, from green to the red curve, leads to a reduction of the trap depth. In the case of the red curve the trap depth gets zero so that the atoms can no longer be trapped.

5.3.2 The crossing optical dipole trap - 'Xdt'

In this section we will characterize the new crossing optical dipole trap, called 'Xdt'. It is intensity-controlled by an AOM which is placed before the optical fiber. This far-detuned ($\lambda = 1064nm$) optical trap is used to provide additional and adjustable confinement of the BEC in longitudinal (z-)direction of the trap. The 'Xdt' outcoupler and all necessary optical components are fixed to an aluminum mount (see Fig. 5.6) which stabilizes the beam passively. The outcoupler (Schäfter und Kirchhoff, 60FC-4-A18-03) delivers a collimated beam with a Gaussian waist of 1.8 mm. Directly after the outcoupler the polarization of the beam is purified by means of a polarizing beam splitter cube. A small fraction of the beam is reflected to a photodiode by a pickup plate and serves as input for a feedback control loop of the beam intensity. This feedback control sets the AOM such that the light intensity after the fibre outcoupler always has the requested value. The beam is widened up in vertical direction by a lens system of two cylindrical lenses (Thorlabs, LJ1144L1-C,$f_1 = 500\,\mathrm{mm}$; Thorlabs, LK1487L1-C, $f_2 = -400\,\mathrm{mm}$) with a combined focal length of: $f_{12} = -2200\,\mathrm{mm}$. Afterwards it is focused by a third lens (Thorlabs, LA1484-C) with a focal length of $f_3 = 303\,\mathrm{mm}$. The resulting beam has an elliptical cross-section with expected $\sigma_0^z = 57\,\mu\mathrm{m}$ and $\sigma_0^y = 266\,\mu\mathrm{m}$ (calculated by Oslo) at the position of the BEC (note that σ_0^y actually is not a waist as the beam is not focused on the position of the atoms in this axis). In two experimental tests using a beam profiler camera and applying the method of moving a razor blade through the beam (see Fig. 5.7) we get $\sigma_0^z = 60\,\mu\mathrm{m}$ and $\sigma_0^y = 240\,\mu\mathrm{m}$. Because of this elliptical cross-section of the intensity profile the 'Xdt' only provides a significant confinement in the longitudinal direction of the trap. From the ratio of σ_0^z and σ_0^y we can estimate the ratio of the trap frequencies in both axes: $\nu_z/\nu_y = \sigma_0^y/\sigma_0^z \approx 4$. In order to create a symmetric double well potential it is necessary to be able to move the

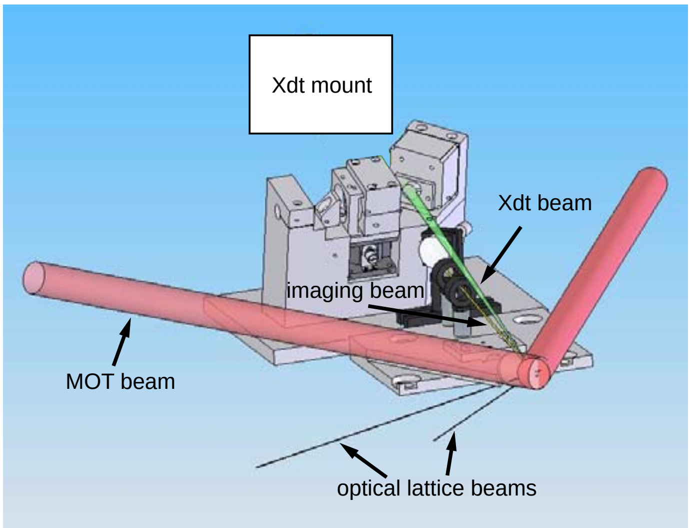

Figure 5.6: Construction drawing of the 'Xdt' mount and schematics of different beams directed onto the atoms. green line: direction of the 'Xdt' beam, yellow line: direction of the imaging beam, red lines: two of the MOT beams, black lines from below: beams of the optical lattice.

'Xdt' beam by remote control in z-direction of the combined trap to assure that an intensity maximum of the optical lattice lies in the center of the trap (see section 5.3.4). We have implemented this feature by reflecting the beam under an angle of 45° on a mirror fixed on a piezo translation-stage (Physik Instrumente, P-611.ZS), see Fig. 5.8. Thus moving the stage forth and back results in moving the 'Xdt' beam right and left (z-direction). The positioning of the piezo translation stage is feedback loop controlled by means of a strain gauge. This compensates for the hysteresis of the piezo and allows to move the 'Xdt' beam during the experimental sequence to arbitrary positions in a spatial range of $140\,\mu$m corresponding to the travel range of the piezo stage of $100\,\mu$m. The positioning noise is currently limited by electronic noise of the controlling signal of 2 mV peak to peak. The voltage resolution of our sequence control program limits the step resolution of the beam translation to 35 nm. This results in the following resolution and accuracy of the Xdt beam positioning:

$$\Delta z_{Xdt} = 35 \pm 14\,\mathrm{nm}, \tag{5.14}$$

where the positioning noise of the beam is 14 nm. By moving the laser beam with the piezo stage behind a sharp edge and detecting with a photodiode we estimate the step response of the feedback loop controlled piezo to be $4-5$ ms, see Fig. 5.9. The whole 'Xdt' mount is vertically angled, so that the beam is directed onto the atoms under an angle of 15° (see Fig. 5.6). Furthermore, the beam can also be vertically adjusted by moving the lens system up and down, which is mounted on a mechanical micrometer translation stage (Melles Griot, 07TEZ703).

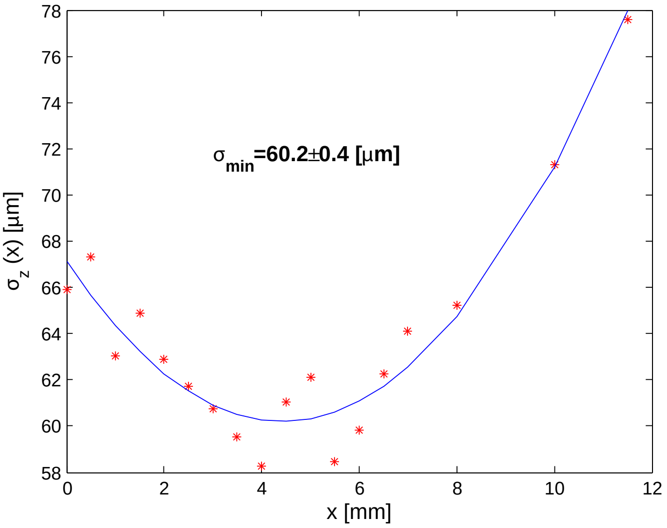

Figure 5.7: By moving a razor blade through the beam and recording the decay of the light intensity it is possible to determine the width of a gaussian laser beam. The obtained light intensity vs. time is described by the so-called error function which is the integral of a Gaussian. Fitting the error function enables one to determine the parameter σ of the corresponding Gaussian. By taking a measurement series for different positions in longitudinal direction of the beam makes it possible to find the minimal Gaussian σ, which is the waist of the beam σ_0. We get $\sigma_0^z = 60.2 \pm 0.4\,\mu$m for the 'Xdt' beam. The given error is an estimation from the fit.

Additional and adjustable longitudinal confinement by the Xdt

As the 'Xdt' beam has a much larger cross-section on the position of the BEC than the charger more optical power is needed to achieve high trap frequencies. The 'Xdt' is operated at beam powers of up to 500 mW corresponding to an additional longitudinal confinement of up to $\nu_z^{Xdt} = 70\,\text{Hz}$. Calculating the total longitudinal trap frequency in the combined trap of charger and Xdt works as follows:

$$\nu_z = \sqrt{\nu_{z\,charger}^2 + \nu_{z\,Xdt}^2} \approx \sqrt{(\nu_\perp/20)^2 + \nu_{z\,Xdt}^2}, \tag{5.15}$$

with $\nu_\perp = \nu_x = \nu_y$ the transversal frequency of the charger and $\nu_{z\,charger}$ and $\nu_{z\,Xdt}$ the longitudinal frequencies of 'charger' and 'Xdt'. Fig. 5.10 illustrates the two laser beams, 'charger' and 'Xdt', creating the crossed optical dipole trap. The isosurfaces on which the intensity has decayed transversally to $1/e^2$ of its maximum value $I_{max}(z)$ and $I_{max}(x)$ respectively are shown. These correspond to the Gaussian width $\sigma(z)$ for the charger and $\sigma_{y,z}(x)$ of the 'Xdt', respectively. Note that for simplicity we regard a coordinate system for the 'Xdt' whose x-axis is the beam axis of the 'Xdt'. As the 'Xdt' beam is directed onto the atoms at an angle of 15° to the optical table, this coordinate system is rotated to our generally used one.

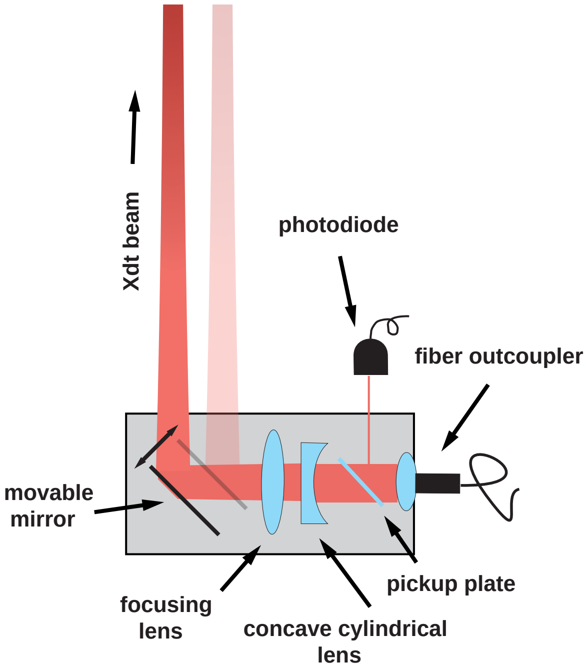

Figure 5.8: Schematics of the 'Xdt' optics. Moving the 'Xdt' beam works by moving a mirror forth and back using a piezo translation stage. The lens system is illustrated in a simplified way.

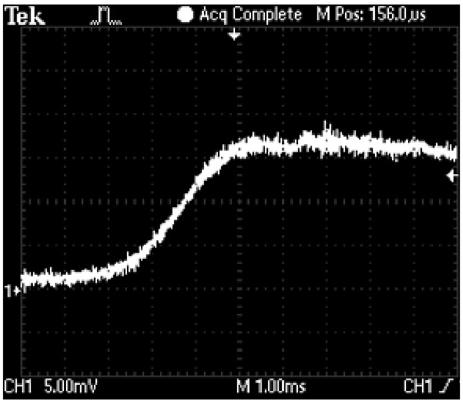

Figure 5.9: The step response of the feedback loop controlled piezo is measured to be $4-5\,\mathrm{ms}$ by means of moving a reflected laser beam.

5.3.3 The optical lattice

To create our optical double well potential we need a one-dimensional optical lattice as described in section 5.2.3. Such optical lattice can be achieved by an interferometer-like setup. To integrate the optical lattice into the new ultra stable beam configuration of the traps we had to redesign this interferometer. We kept the basic principle described in [Alb2005, Gat2006] but changed the folding of the beam path and the whole mount. The interferometer is now placed in a hole going horizontally through the massive aluminum block which also connects the two dipole traps. The idea is

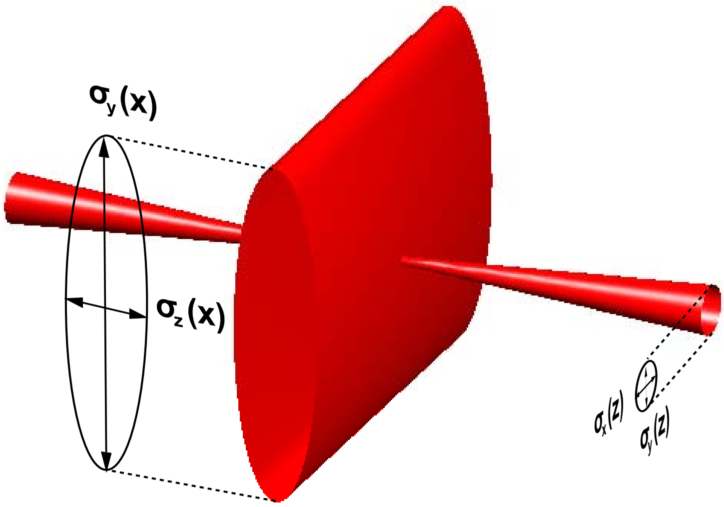

Figure 5.10: Crossing beams of charger and 'Xdt'. Isosurfaces with $I = I_{max}(z)/e^2$ and $I = I_{max}(x)/e^2$ respectively are shown. The 'Xdt' beam has an elliptic cross-section with a ratio of $\sigma_0^y/\sigma_0^z \approx 4$. For simplicity the angle of incidence of the 'Xdt' of $15°$ onto the atoms is not regarded here and we use a coordinate system whose x-axis is the beam axis of the 'Xdt' and whose z-axis is the beam axis of the charger respectively.

again to have a mechanical connection of all outcouplers of laser beams necessary for the creation of our optical double well potential, so that relative drifts are minimized. The interferometer exhibits a Mach-Zehnder type beam configuration. After the fiber outcoupler and an absorptive polarizer the beam is split into two paths by a non-polarizing beam splitter. One beam path contains an electro-optic modulator (EOM) which can shift the phase of the light field by means of the Pockels effect. The two final mirrors direct the two beams from inside the aluminum block under an angle of $22°$ upwards to the position of the BEC. There they cross and interfere (see Fig. 5.11) under an angle of $8.5°$ resulting for the applied wavelength of the laser ($\lambda_l = 843\,\text{nm}$) in an optical lattice with a lattice spacing of $5.7\,\mu\text{m}$. The lattice spacing can be directly measured with our CCD camera as shown in Fig. 5.12. By adjusting the relative phase of the two beam paths with the EOM the phase of the resulting interference pattern can be changed shifting the lattice. The intensity and the phase of the optical lattice are feedback-loop-controlled. The intensity lock is similar to the ones of the dipole traps, using an AOM. Pickup plate and photodiode to detect the intensity of a small fraction of the main beam are integrated directly into the mount of the fiber outcoupler. To be able to lock the phase of the lattice, reflections of the two lattice beams from a pickup plate close to the experimental chamber are directed to a photodiode with a micrometer slit in front of it. There they create an image of the interference pattern at the BEC. The feedback loop adjusting the phase by the mentioned EOM locks an intensity maximum of the interference pattern in front of the slit. As the signal is noisy a lock-in amplifier is employed.

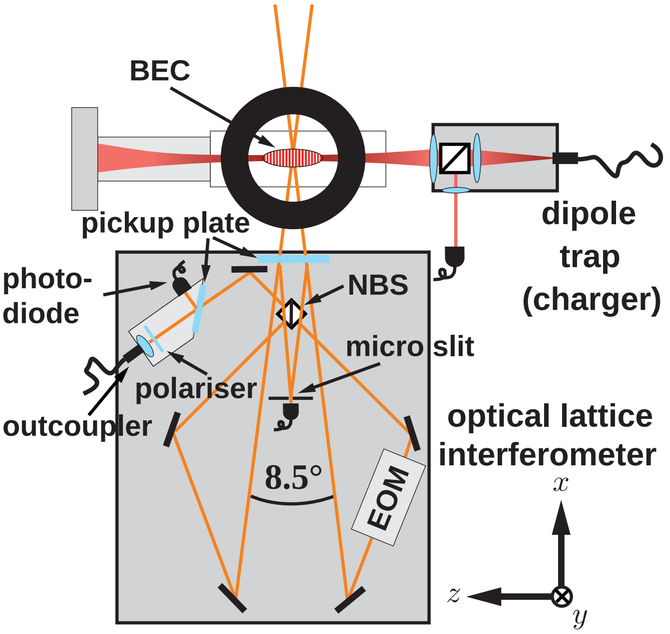

Figure 5.11: Scheme of the optical lattice interferometer. The interferometer is placed in a hole of the massive aluminum block which connects all optical dipole traps. The two lattice beams are directed onto the BEC from below under an angle of 22° in the x-y-plane (not illustrated in this simplified scheme). Details see text.

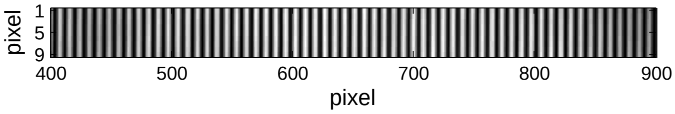

Figure 5.12: Image of the interference pattern created by the optical lattice interferometer. The lattice spacing L was measured directly on the CCD camera to be $L = 5.7\,\mu$m.

For this purpose, the light of the two lattice beams is modulated by a frequency of 60 kHz on the AOM. The two lattice beams have a diameter of $\approx 500\,\mu$m at a wavelength of $\lambda = 843$ nm. Thus the condition $\sigma \gg \lambda$ is fulfilled so that the interference pattern at the position of the atoms can be well approximated as an interference of two plane waves. Also the spatial extension of the whole BEC in the dipole trap is much smaller than the beam diameter by approximately a factor of 10. The lattice can be operated with optical powers of up to ≈ 100 mW in each beam. This results in a typical lattice height of the order of up to $V_0/h \approx 4000$ Hz. The different angles under which 'Xdt' and optical lattice beams are directed onto the BEC are illustrated in Fig. 5.13.

5.3.4 The ultra stable optical double well potential

As described above we have mechanically connected the three components (see sections 5.3.1, 5.3.2 and 5.3.3) that create our optical double well potential in a new

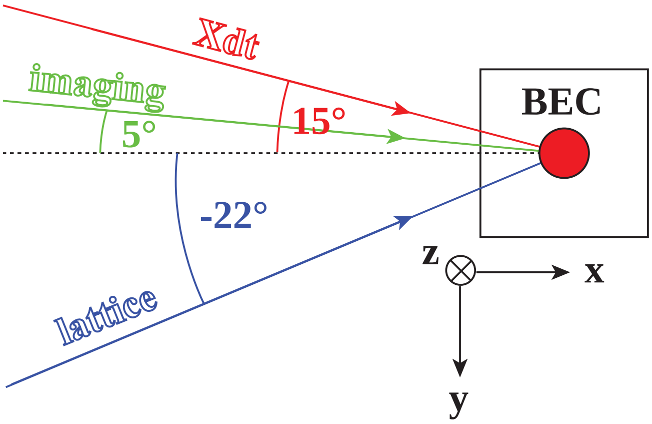

Figure 5.13: Scheme of different beams directed onto the BEC in view from the side.

quasi drift-free setup. This double well potential is created by superimposing the crossed optical dipole trap (consisting of the 'charger' and the 'Xdt') with the 1D optical lattice. An example for such a potential is shown in Fig. 5.14. To give evidence for the claimed stability of our setup we show two long term measurements of the BEC in our double well potential. We illustrate the drift freeness of the density distribution as well as the stability of the relative phase between the two wells measured in time of flight [And1997] (see Fig. 5.16).

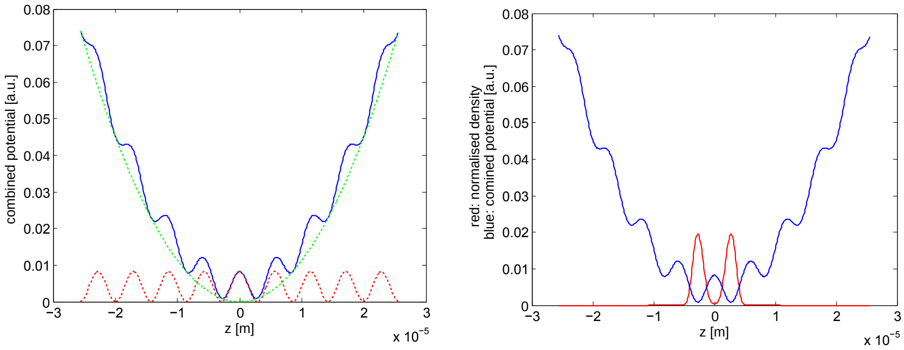

Figure 5.14: **left**: We create a double well potential (blue curve) by superimposing a harmonic optical dipole trap (green dashed curve) and a one-dimensional optical lattice (red dashed curve). **right**: Ground state density (red curve) of a BEC in the double well potential (blue curve).

This stability has enabled us to perform measurements of the full evolution dynamics of dark solitons in a BEC like shown in Figs. 4.3a,4.4, 4.10 and Fig. 4.11, where additionally the 'Xdt' beam had to be moved several hundred times during the measurement series to obtain a phase difference of π between the two wells of the initial double well potential.

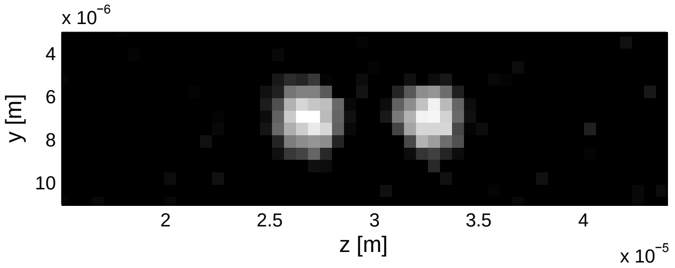

Figure 5.15: Experimental image of a BEC trapped in the double well potential.

5.4 Imaging the density distribution of the BEC

One of the key points of our experiments is the detection of the density distribution of a BEC. We use the technique of high power absorption imaging, which is well suited for imaging large optical density clouds. To do so, a resonant laser beam is directed onto the atoms, captured by an imaging objective and detected on a CCD camera. Thereby the shadow of the BEC is imaged onto the chip of the camera. As the laser beam is resonant to an atomic transition the absorption imaging technique [Ket1999] is of destructive nature. In our experiment we use a σ^+ polarized Gaussian laser beam (waist 1.9 mm) resonant on the $F = 2 \to F' = 3$ transition of the D_2 line of ^{87}Rb at a pulse duration of $5\,\mu$s and a CCD camera (Q-Imaging, Retiga EXi) with a quantum efficiency of 15% and a pixel size of $6.45\,\mu$m. The camera has been tested to be shot noise limited (see [Ott2006] for details). A new objective with a resolution of $\approx 1\,\mu$m (see Fig. 5.17) has been built into the imaging system. The total imaging system including an additional imaging lens has a magnification of $M = 11.2$.
To determine the density distribution of the BEC we take two pictures. The first picture is the one where the imaging beam shines onto the atoms. From this we can retrieve the intensity distribution I_{pic}. The second picture is a reference picture, where the imaging beam is switched on, but without any atoms. This picture provides the intensity distribution I_{refpic}. Our camera has a negligible dark count rate for the applied imaging pulse duration of $5\,\mu$s. Therefore, the intensity profiles of the imaging beam before going through the atoms I_{in} and after going through I_{out} are directly given by:

$$I_{in} = I_{refpic} \quad and \quad I_{out} = I_{pic} \tag{5.16}$$

We now have the task to calculate the atomic density distribution from the two measured quantities I_{in} and I_{out}. To do so, we consider the reduction of the intensity of a laser beam profile going through an absorptive medium. This process is described by the following differential equation (see also [Gat2006]):

$$\frac{dI(\mathbf{r})}{dx} = -\sigma_{sc}(I(\mathbf{r}))n(\mathbf{r})I(\mathbf{r}) \tag{5.17}$$

with $n(\mathbf{r})$ the local atomic density distribution, $I(\mathbf{r})$ the intensity profile of the laser beam and σ_{sc} the scattering cross-section,

$$\sigma_{sc}(I(\mathbf{r})) = \sigma_{sc}^0 \left(1 + \frac{I(\mathbf{r})}{I_s}\right)^{-1} \quad with \quad \sigma_{sc}^0 = \frac{\Gamma\hbar\omega_l}{2I_s} \tag{5.18}$$

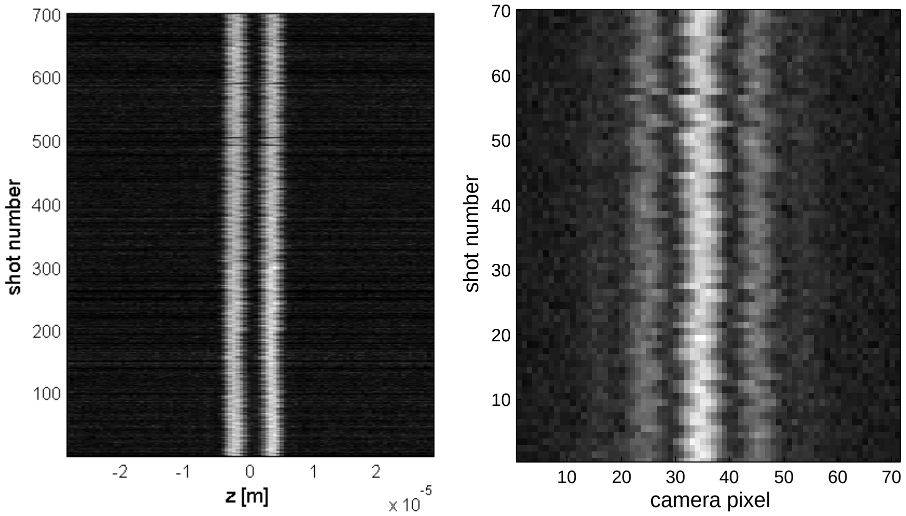

Figure 5.16: Testing the stability of the setup. **left**: Spatial stability of the double well. No significant symmetry shifts are observed on the checked timescale of $\approx 11\,\mathrm{h}$ corresponding to 700 shots of the experiment. The small spatial jitter of $\approx 1\,\mu\mathrm{m}$ from shot to shot is due to the movement of the imaging objective and the corresponding reproducibility in positioning. This effect does not change the symmetry of the double well. **right**: Stability of the phase difference between the two wells $\Delta\phi$, measured in time of flight for a time scale of $\approx 1\,\mathrm{h}$ corresponding to 70 shots. We determine the phase stability to be $\Delta\phi = 0 \pm 0.06$.

at the applied laser frequency, which is proportional to the rate of spontaneous emission given by Eqn. 5.3. As only the column density $N(y_0, z_0)$ [Gat2006] of the atom cloud in x-direction (beam direction),

$$N(y_0, z_0) = \int_{y_0-d_y/2}^{y_0+d_y/2} \int_{z_0-d_z/2}^{z_0+d_z/2} \int_{-\infty}^{+\infty} n(x, y, z)dxdydz, \tag{5.19}$$

is accessible to the experiment we have to express this quantity in terms of the intensity decay described by Eqn. 5.17. We assume that the column density is locally homogeneous around (y_0, z_0), the center of each camera pixel. The effective pixel size can be expressed as $dy \cdot dz = P/M^2$, with the real pixel size P and the magnification of the imaging system M. Integration over the pixel size and inserting dx of Eqn. 5.17 into Eqn. 5.19 leads to:

$$N(y_0, z_0) = -\frac{P}{M^2}\frac{1}{\sigma_{sc}^0}\int_{I_{in}(y_0,z_0)}^{I_{out}(y_0,z_0)} \frac{1+\frac{I(\mathbf{r})}{I_s}}{I(\mathbf{r})}dI. \tag{5.20}$$

Performing this integration we finally get an equation allowing to reconstruct the atomic column density corresponding to each effective camera pixel. This equation only needs the measured beam intensity (more precisely irradiance $[W/m^2]$) profile with and without atoms, and is given by

$$N(y_0, z_0) = \frac{P}{M^2}\frac{1}{\sigma_{sc}^0}\left(\frac{I_{in}(x_0, y_0)}{I_s} - \frac{I_{out}(y_0, z_0)}{I_s} + \ln\frac{I_{in}(y_0, z_0)}{I_{out}(x_0, y_0)}\right). \tag{5.21}$$

In order to apply Eqn. 5.21 to the experimental case one has to consider and calibrate the offsets due to the measurement procedure. First of all the experimental imperfection of the used σ^+ light leads to the correction factor p_{cor} of the saturation intensity I_s as due to this effect not every photon can excite the transition: $I_s \rightarrow I_s/p_{cor}$, with $p_{cor} \leq 1$. As the light intensity is measured by a CCD camera the detection efficiency C_{cor} of this camera has to be taken into account: $C_{cor} = (\hbar\omega_l)/(Q_E\eta)$, with Q_E the quantum efficiency and η the gain of the camera (conversion of photons to electrons). Finally, there can be an offset of the absolute intensity of the imaging beam: $I \rightarrow I \cdot I_{cor}$. As these last two calibration factors are only important for the absolute intensity they only appear in the first term of Eqn. 5.22. Besides this the CCD camera does not measure an intensity, but the integration of a light intensity profile over a certain duration τ of an imaging pulse: $I[W/m^2] \rightarrow E[J/m^2]$. Regarding all these experimental calibration factors Eqn. 5.21 converts to:

$$\begin{aligned} N(y_0, z_0) = \frac{P}{M^2}\frac{1}{\sigma_{sc}^0}(&\left(\frac{E_in(x_0, y_0)}{E_s\tau} - \frac{E_{out}(y_0, z_0)}{E_s\tau}\right) I_{cor}C_{cor} + ... \\ &... + \frac{1}{p_{cor}}\ln\frac{E_{in}(y_0, z_0)}{E_{out}(x_0, y_0)}). \end{aligned} \tag{5.22}$$

5.4.1 The imaging system

A new imaging objective has been characterized in [Ott2006] and has been built into the experiment during the time of this thesis. The theoretically expected resolution by the Rayleigh criterium,

$$\Delta r = 0.61\frac{\lambda}{NA} = 1.1\,\mu\mathrm{m}, \tag{5.23}$$

at $\lambda = 780\,\mathrm{nm}$ and a numerical aperture of $NA = 0.45$ was experimentally tested in [Ott2006] and reproduced very well. Hence, the imaging objective can be regarded as diffraction limited. Directly in the experiment the resolution has been tested again by creating an elongated BEC with a transverse width of δy below the optical resolution of $1\mu m$. Due to the limited resolution such a small transverse width is blurred up to the resolution limit. Indeed the smallest width of a BEC which could be observed was $\approx 1\,\mu$m which confirms the tests outside the experimental apparatus.

To create such a system the atom number of the BEC must be small so that the following condition is fulfilled: $\mu/(\hbar\omega_\perp) < 1$, transverse non-TF regime (see section 3.11). In this case the transverse width of the BEC is given by the transverse harmonic oscillator length $a_\perp$. The atom number in the charger trap to realize this situation lies in the range of $N \leq 500$ for $\nu_\perp = 1000\,\mathrm{Hz}$ and $\nu_z = 50\,\mathrm{Hz}$, resulting in $a_\perp < 350\,\mathrm{nm}$.

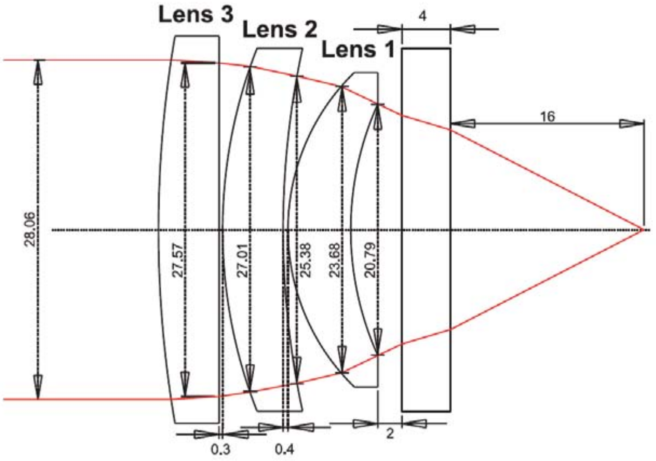

Figure 5.17: The imaging objective consists of a system of three lenses. It exhibits a working distance of $2.2\,\mathrm{cm}$ including the wall of the BEC chamber (glass cell). Therefore it has to be placed $2\,\mathrm{mm}$ away from the glass surface (very right component) of this chamber for imaging. The objective is optimized for $\lambda = 780\,\mathrm{nm}$ and has an optical aperture of $NA = 0.45$.

As the objective has a working distance of $2.2\,\mathrm{cm}$ it has to be placed only $2\,\mathrm{mm}$ away from the glass surface of the BEC chamber for imaging. As it blocks two MOT beams in this position the objective has to be moved in and out for every experimental cycle. It is therefore placed on a remote controlled micrometer precision translation stage (Micos, LS-110), see Figs. 5.2 and 5.18. Behind the objective two narrow bandpass filters (Semrock, BrightLine HC 780/12) are placed. These filters block the beams of

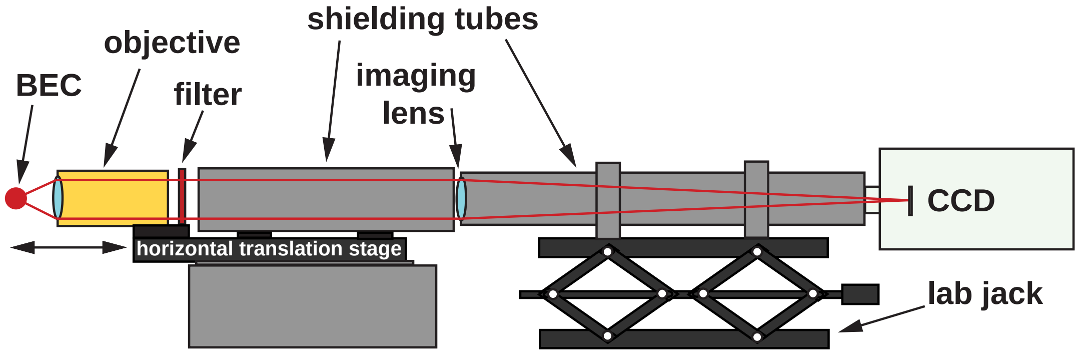

Figure 5.18: Schematics of the imaging system. The objective is placed on a remote controlled horizontal translation stage and has to be moved forth and back during every experimental cycle in order not to block two MOT beams. A narrow band pass filter blocks the light of the Xdt and the optical lattice and transmits only the imaging light at $\lambda = 780nm$. An additional lens images the picture of the BEC to the chip of a CCD camera. Shielding tubes prevent possible scattered light from reaching the CCD camera.

the 'Xdt' and the optical lattice at an optical density of $od > 10^{12}$ and transmit the imaging beam at an efficiency of $T \approx 0.95$. An additional imaging lens focuses the light coming from the objective onto the CCD camera. A shielding tube prevents scattered light from affecting the imaging.

5.5 Calibration of the experimental parameters

5.5.1 Calibration of the trap frequencies

Calibration of the longitudinal trap frequency ν_z

By moving the 'Xdt' beam as fast as possible to the side and back (z-direction) the BEC ground state of the crossed harmonic optical dipole trap can be displaced from the trap center. To prevent leaving the harmonic region of the trap this displacement should be small. As a displaced ground state in a harmonic trap does not disperse during its oscillation in the trap the trapping frequency can be directly measured from the propagation path of the BEC (see Fig. 5.19). The resulting relative error of the longitudinal trapping frequency is $\Delta\nu_z/\nu_z \approx 0.01$.

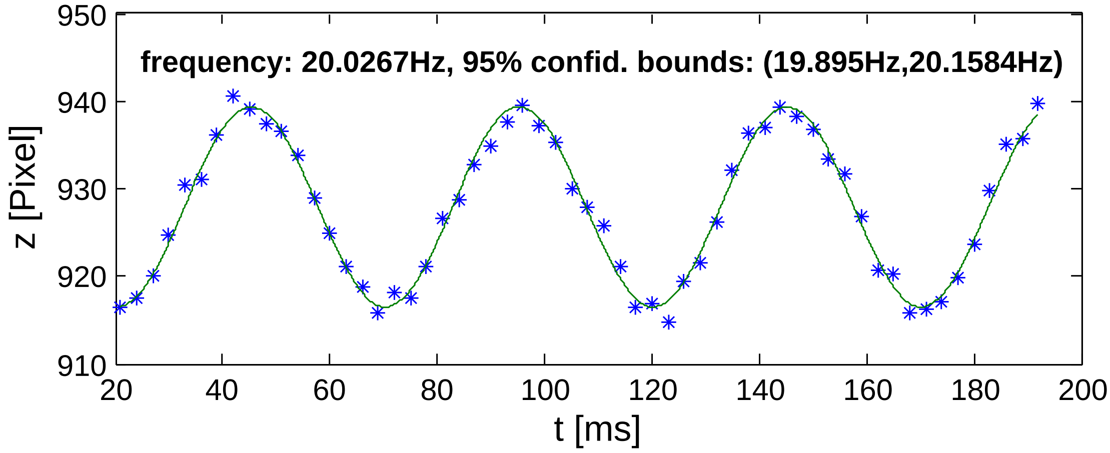

Figure 5.19: Measureing ν_z. By exciting the dipolar motion of the harmonic ground state of the BEC in the trap the trap frequency can be directly measured. The fit reveals the high grade of harmonicity of the longitudinal direction of our trap.

Calibration of the transverse trap frequency $\nu_\perp$

As the BEC in the charger trap is tightly confined transversally the resolution of the imaging system is not sufficient to monitor a transverse dipole oscillation of the atom cloud. Therefore we have to use a different technique for the calibration of the transverse frequency than for the longitudinal frequency. The parametric heating effect offers a possibility to calibrate the transverse frequency in this case. If the light intensity of the trap is modulated by means of the intensity controlling AOM with a frequency of $\nu = 2\nu_\perp$, the BEC is excited strongly which leads to heating and a subsequent particle loss. This means that by scanning the modulation frequency around the expected frequency $2\nu_\perp$ an atom loss curve can be obtained (see Fig. 5.20) which by fitting allows the determination of the trap frequency. The relative error for this method is on the order of $\Delta\nu_\perp/\nu_\perp = 0.1$.

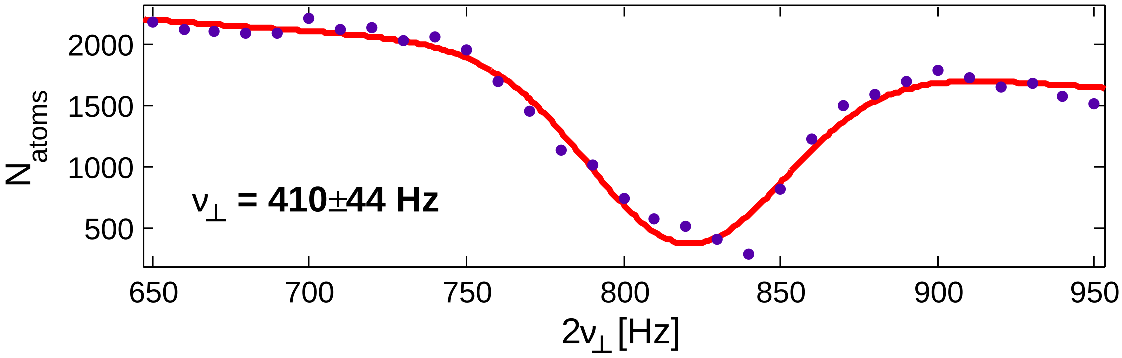

Figure 5.20: Measuring $\nu_\perp$. The transverse trap frequency can be measured by parametric heating and subsequent fitting of the atom loss curve around $2\nu_\perp$.

5.5.2 Calibration of the optical lattice height

The optical lattice can be calibrated by loading a BEC into a double well potential with low barrier and afterwards suddenly increasing the barrier height by increasing the lattice height. This will excite an oscillation of the BECs in the two wells. As the two wells are small in elongation the oscillation amplitude of the two BECs exceeds the range which can be described by the harmonic approximation. Therefore, the oscillation trajectory is inharmonic and quite complex making it impossible to fit the data by a simple sin-function. To solve this problem we compare the obtained oscillation data with 3D GPE simulations of the whole process for different lattice heights. We chose the simulation with the smallest standard deviation from the measured data points. By doing so we determine the lattice height including a relative error of $\Delta V_0/V_0 \approx 0.15$. A more detailed description of the method can be found in [Gat2006].

5.5.3 Calibration of the atom number

To obtain an exact value for the number of atoms composing a BEC from Eqn. 5.22 it is necessary to calibrate two experimental offsets, as discussed in section 5.4. How these can be obtained will be discussed in the following. The factor p_{cor} can be estimated by measuring the atom number of a BEC at two different intensities. At high intensity the first term completely dominates Eqn. 5.22 and therefore the atom number obtained can be regarded as correct. For low light intensities Eqn. 5.22 is

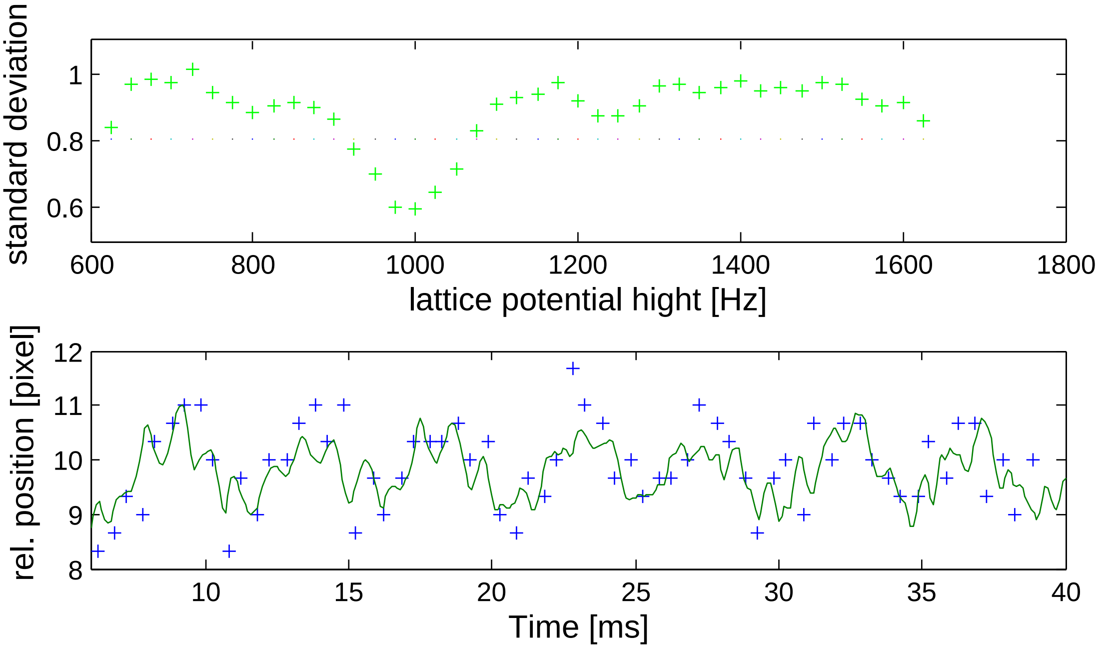

Figure 5.21: By exiting the dipolar motion of the two BECs in the double well potential and subsequent comparison with 3D GPE simulations the height of the optical lattice can be estimated. **top**: Determination of the standard deviation of the experimental data from 3D GPE simulations varying the height of the optical lattice and keeping all other experimental parameters fixed. We see a minimum in the standard deviation indicating the correct lattice height. **bottom**: Distance between the two oscillating BECs vs. time for the chosen lattice height. For the current double well setting the motion is quite complex and inharmonic.

dominated by the second term. The factor p_{cor} corrects the atom number values obtained at low intensity to the value obtained at high intensity. As there might still be an uncertainty in the absolute value of the intensity Eqn. 5.22 can be cross-checked by an independent method of estimating the atom number. For that an elongated BEC in the longitudinal TF-regime (see section 3.11) is created in a harmonic trap. In this regime the longitudinal width and density profile is dominated by the interparticle interaction, which is proportional to the number of atoms. By comparing the experimentally measured widths in longitudinal and transverse direction of the BEC with the corresponding values obtained by 3D GPE simulations one can estimate the factor I_{cor} compensating an eventual uncertainty in the absolute beam intensity. A more detailed explanation of this method can be found in [Gat2006]. The atom number calibration results in an estimated final offset of $\Delta N/N \approx \pm 0.15$.

We have characterized our experimental setup focusing on the changes made during the time of this thesis. We have seen that an advantage of this setup is the combination of ultra stable optical dipole traps with a high-resolution imaging system. This enables one to perform experiments requiring a high rate of reproducibility as well as a high optical resolution, like the observations of dark solitons which we have discussed in this thesis. The setup also has enabled the observation of squeezing and entanglement in a BEC [Est2008]. This will be the content of [Gro].

Chapter 6

Conclusion and outlook

We have created pairs of dark solitons in a harmonically confined Bose-Einstein condensate (BEC) in the crossover regime between 1D and 3D. To create the solitons we apply the method of matter wave interference of two BECs initially separated in a double well potential. Due to the chosen trap geometry and the low atom number of the order of $N \approx 1500$ the solitons are for the first time stable against the so-called snaking instability [Mur1999, Mur2002] for arbitrarily small velocities. We have observed multiple collisions and oscillation periods of the solitons in the harmonically confined BEC. This has enabled us to measure the frequency of the solitons and to show their repulsive inter-soliton interaction by probing the frequency vs. the mean distance between the two solitons. Besides this we have compered our findings to numerical simulations of the Gross-Pitaevskii equation and effective 1D equations and observe good agreement between experiment and numerics. We have thereby confirmed theoretical predictions which could not be observed in earlier dark soliton experiments where the solitons suffered from the snaking instability and their resulting short lifetime. Our two most important findings are first the confirmation of the prediction that the frequency of dark solitons ν_d in the crossover regime between 1D and 3D lies in the range $1/\sqrt{2} < \nu_d < \nu_z$ [Bus2000, The2007], with ν_z the longitudinal trap frequency, and second the experimental demonstration of the repulsive inter-soliton interaction from frequency measurements. Besides this we have developed an effective potential for dark solitons confined in a harmonic trap based on an inter-soliton interaction potential given in [Kiv1995]. Within this model the solitons can be described as classical particles with repulsive interaction for the case of small soliton velocities. This model also helps us to distinguish between the effects of dimensionality and of the inter-soliton interaction on the soliton oscillation frequency.

In a planned future experiment we will show the soliton frequency trend for the case of one standing soliton in the middle of the trap and on each half of the trap an additional oscillating soliton. In this symmetric three soliton system the inter-soliton interaction is increased due to the non-moving soliton in the middle resulting in higher oscillation frequencies. The method of creating this system is described in chapter 3.3.2 and has already been demonstrated in a first experiment.
As our solitons are stable against the snaking instability they can only decay by tem-

perature induced effects [Fed1999]. Another future task of our studies on dark solitons would therefore be the performance of long term measurements on a timescale of the evolution dynamics of $t > 100ms$. In such measurements the temperature induced soliton decay could be observed as a decay in the contrast of the solitons and could be compared to theoretical predictions. This would for the first time give an experimental insight into the decay process of dark solitons.

Appendix A

Proposal for the creation of a fundamental discrete bright soliton by the method of [Mat2006] in our experimental setup

In this chapter we discuss the applicability to our setup of a new method for creating a bright soliton as proposed by Matuszweski et al. [Mat2006]. The method has a strong analogy to the creation of spatial optical solitons in discrete waveguide arrays [Eis1998].

A.1 Bright solitons in repulsive BECs

Since a repulsive BEC does not naturally support bright solitons but dark solitons one has to use a trick to create such solitons there. One possible method consists of putting the BEC into an optical lattice. Atoms in an optical lattice obey a periodic dispersion relation similar to electrons in a solid state body leading to an energy band structure [Eie2004]. If one can manage to create a wave packet consisting of momenta near the edge of the first Brillouin zone the repulsive inter-atomic interaction can be compensated by the dispersive term through a negative effective mass, allowing for bright solitons. The effective mass formalism is valid in the approximation of weak potentials, where $V_0 < 2E_r$ [Eie2004], with V_0 the depth of the lattice potential and $E_r = \hbar^2 k^2/(2m)$ the photon recoil energy. In this approximation the effective mass on the edge of the first Brillouin zone can be estimated as:

$$m_{eff}(k_r) = \frac{s}{s-8} m, \tag{A.1}$$

with $s = V_0/E_r$ and $k_r = \sqrt{(2mE_r)/\hbar^2}$ [Eie2004]. A bright soliton in a repulsive BEC was realized for the first time in [EieII2004] where the negative effective mass of the wave packet was achieved by creating a relative momentum between the optical lattice and the BEC. As shown in [Eie2004] the atom number N of the soliton is fixed by:

$$N = \frac{\hbar}{|m_{eff}|\omega_{\perp}\alpha_{NL}a_s x_0}, \tag{A.2}$$

with the effective mass m_{eff}, x_0 the width of the soliton and $a_{NL} = 1.5$. If Eqn. A.2 is fulfilled the effects of dispersion and nonlinear repulsive interaction compensate each other.

A.2 The creation method of Matuszewski et al.

The method of [Mat2006] suggests the creation of a bright soliton without the necessity of accelerating the lattice or the BEC. With the experimental parameters adapted to our setup, the procedure works as follows. One starts with the BEC of $N = 200$ atoms confined in only one well of an optical lattice with a height of $V_0 = 15E_r$ and a lattice spacing of $L = 5.7\,\mu$m. The confinement is achieved by a harmonic trap of the frequencies $\nu_{\perp} = 125\,$Hz and $\nu_z = 65\,$Hz. In the next step ν_z is switched off as fast as possible (e.g. in 1 ms) and the intensity of the optical lattice is ramped down linearly on a time scale of $t_{ramp} = 0.5\,$s to the final value of $V_{fin} = 2E_r$ (parameters estimated by [Mat]). This results in a fundamental (stationary) discrete bright soliton as can be seen in Fig. A.1.

Using this method and assuring that the chosen parameters fulfill Eqn. A.2 the soliton creates itself. Starting from a single occupied lattice site the atoms will at

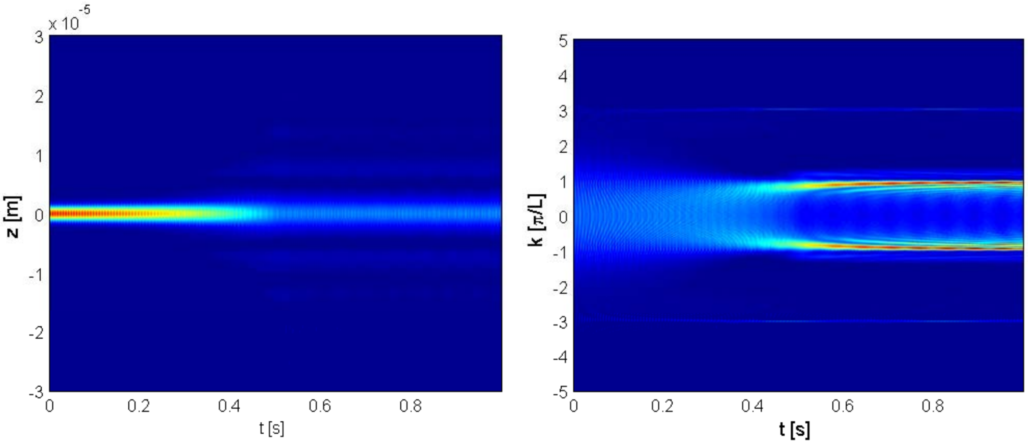

Figure A.1: Numerical simulation using the MDE of the creation of a bright soliton by the method of Matuszewski et al.. **left**: Time evolution of the atomic density in real space. At $t = 0.5\,$s the soliton has been created. **right**: Time evolution of the atomic density in momentum space. The momenta accumulate at the edges of the first Brillouin zone at $k = \pi/L$. Parameters: See text first spread in momentum space and then accumulate at the edge of the first Brillouin zone as can be seen in Fig. A.1(right). Note that in the case of a discrete lattice soliton not the wave function itself has the characteristic form of the soliton (see Eqn. 1.2) but its envelope. This can be seen in Fig. A.2(left) where we fit the envelope of the wave function with a sech-function. In Fig. A.2(right) we check by numeric simulation that our system obeys Eqn. A.2. To do so we change certain parameters according to Eqn. A.2 in a way that preserves the width of the soliton x_0. In our example we keep the product $N\nu_\perp$ fixed which as we see in Fig. A.2(right) does not change the shape of our soliton significantly. We see that our setup in principle allows the creation of the Matuszewski soliton as we have used applicable parameters in our simulation. One problem will occur as we will see in chapter A.3: The chemical potential μ of the condensate is higher than the lattice depth V_0. This means that the optical dipole trap has to be balanced extremely well perpendicular to the direction of gravity. Otherwise the atoms would flow away to the side.

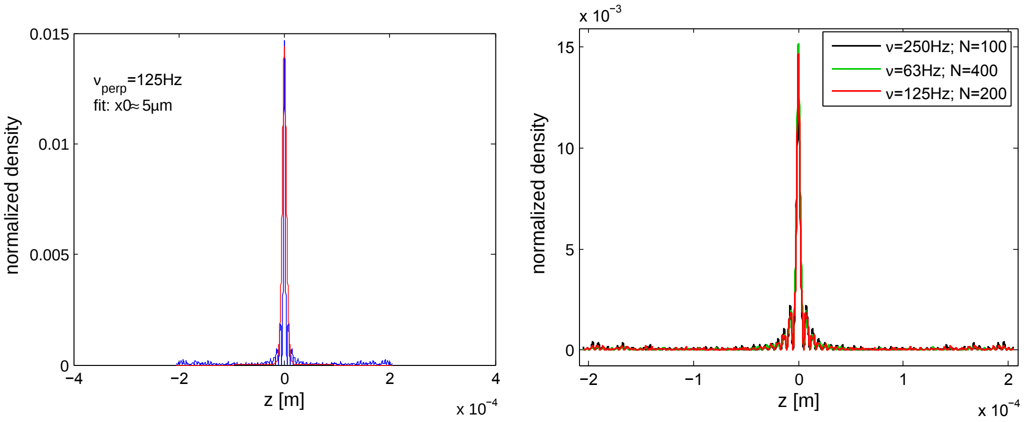

Figure A.2: **left**: Density distribution of the soliton (blue) and fit by a sech-function (red). The width of the soliton is $x_0 \approx 5\,\mu\mathrm{m}$. **right**: The shape of the soliton does not significantly change if N and $\nu_\perp$ are changed preserving $N \cdot \nu_\perp$.

A.3 The Peierls-Nabarrow potential barrier

Until now we have considered only the case of a discrete lattice soliton with its center on a lattice site, the so called on-site soliton. But it is in principle also possible to create a soliton with its center between two lattice sites, the so called inter-site soliton (see Fig. A.3). The inter-site soliton exhibits a higher energy than the on-site one [Ahu2004]. Therefore if one wants to move an on-site soliton the energy difference between the two states ΔE_{PN}, the so called Peierls-Nabarrow potential barrier, has to be overcome. Using the parameters of chapter A.2 we can create both kinds of solitons by numerical simulation and estimate their corresponding energies (see Fig. A.4). We create the inter-site soliton in the simulation by starting with two occupied lattice sites and imprinting a phase difference of π between the two sites. Determining the energies of the on-site and the inter-site soliton numerically enables

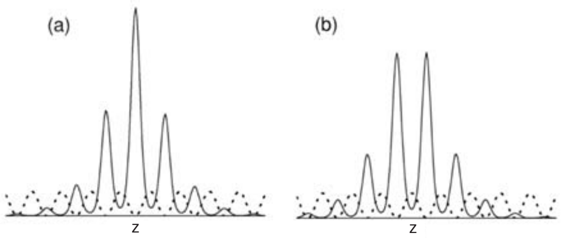

Figure A.3: **left**: On-site soliton, **right**: Inter-site soliton. The dashed line indicates the optical lattice. Figure taken from [Ahu2004].

us to estimate the Peierls-Nabarrow potential barrier ΔE_{PN}. The next question is: how could this barrier be estimated in an experiment?

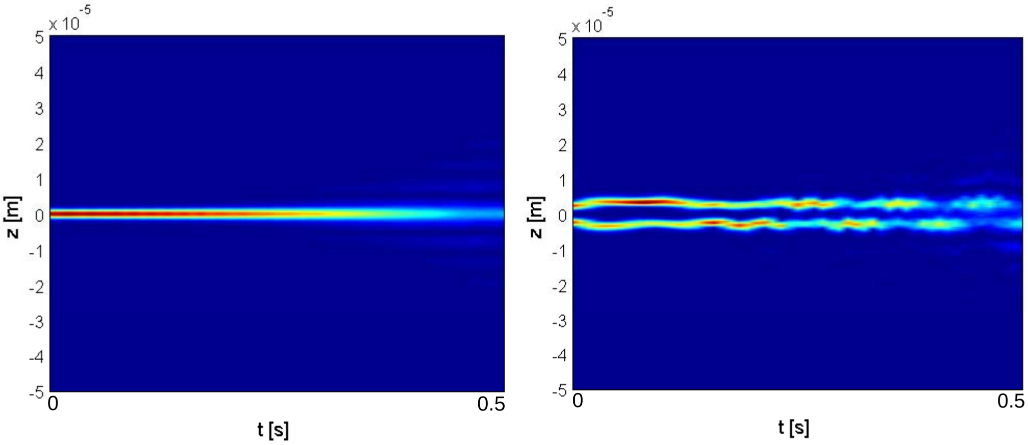

Figure A.4: Simulating the creation of the on-site (**left**) and inter-site (**right**) soliton. The inter-site soliton is undergoing a continuous oscillation.

Following a suggestion of [Ahu2004] one could do this by adding another external potential to the system, e.g. a linear or also a harmonic one. As e.g. the slope of a linear potential is increased step by step, from a certain slope on it is possible for an on-site soliton to overcome ΔE_{PN} and start moving.
We first consider the case of adding a harmonic potential as this would be easier to realize in our experiment. To realize a slope on the position of the on-site soliton we assume the center of the harmonic potential to be shifted away from the center of the soliton by: $\Delta z = 60\,\mu$m. Varying the frequency ν_z of the trap we can vary the slope of the potential. Unfortunately we cannot use the parameter set of chapter A.2 as the chemical potential of the condensate in this case is higher than the lattice depth $\mu \approx 5.3V_0$, with $V_0 = 2E_r$ (see chapter A.2). This means that if adding a potential slope the atoms will immediately flow away. So the first thing we have to do is making μ smaller than V_0 in a way that Eqn. A.2 is still fulfilled. We keep the atom number fixed on $N = 200$, because this is already a quite small number for an experiment. The remaining possibility is to directly increase V_0. We increase the lattice potential to $V_0 = 7E_r$ implementing $\mu \approx 0.5V_0$. By doing so we also increase the effective mass from $m_{eff} = -1/3$ in the case of $V_0 = 2E_r$ to

$m_{eff} = -7$ in the case of $V_0 = 7E_r$ (see Eqn. A.1)[1]. To compensate for this increase of effective mass we have to lower the transverse trap frequency from $\nu_\perp = 125\,\mathrm{Hz}$ to $\nu_\perp = 6\,\mathrm{Hz}$. Unfortunately such small transverse trap frequency cannot be achieved with our optical dipole trap. Therefore the following is a principle discussion of how the Peierls-Nabbarow potential barrier could be measured, but is not applicable to our experiment.

We assume the same parameters and ramping times to create the soliton as in chapter A.2, except the following parameters which we set to: $V_0 = 7E_r$ and $\nu_\perp = 6\,\mathrm{Hz}$. The soliton is created after $t_{ramp} = 0.5\,\mathrm{s}$. 50 ms later we switch on a harmonic trap shifted away from the center of the soliton by $\Delta z = 60\,\mu\mathrm{m}$. We perform several numerical simulations increasing the trap frequency step by step and calculate the difference in potential energy $\Delta V/L$ which the harmonic trap induces on the length scale of the lattice spacing L. If $\Delta V/L > E_{PN}$ the soliton should start moving. In Fig. A.5(left) we show the momentum $k_{\Delta E}$ in units of k_r which the solitons can maximally gain from the potential difference $\Delta V/L$ for traps of different frequencies ν_z. We additionally plot different important thresholds. The most important threshold is E_{PN} which corresponds in the regarded case to a momentum of $2.58k_r$,

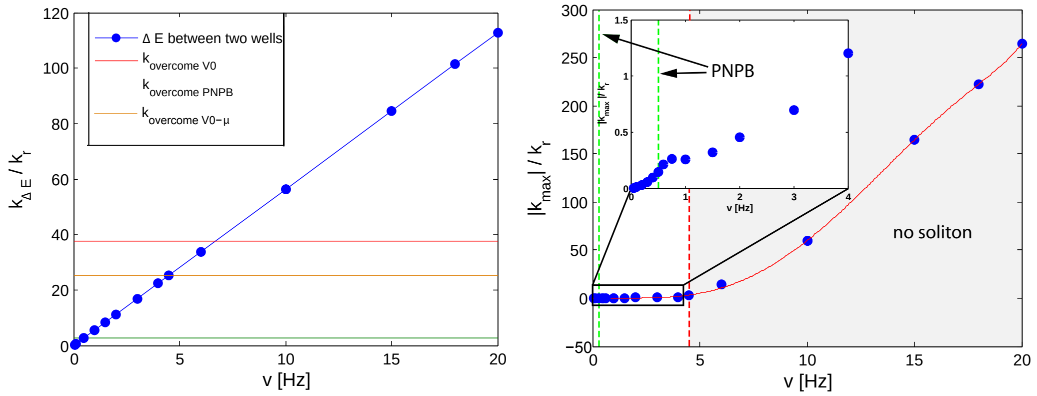

Figure A.5: **Left**: Possible momentum $k_{\Delta E}/k_r$ which can be gained from the difference in potential energy $\Delta V/L$ for different values of the transverse trap frequency $\nu_\perp$. The critical momenta to overcome different thresholds are shown by the horizontal lines. **Right**: Maximal effective momenta gained by the whole atom cloud during the time evolution for different values of ν_z. The red line is a fit to the data. The zoom shows the area important for the observation of the Peierls-Nabarrow potential barrier (PNPB) ΔE_{PN}. The value of ΔE_{PN} has been obtained by numerical simulations. Below the value $k_{overcome\ PNPB}$ of the momentum corresponding to ΔE_{PN} the soliton cannot move. This momentum is reached at $\nu_z \approx 0.5\,\mathrm{Hz}$ shown by the green dashed line. When $\Delta V/L \gtrsim V_0 - \mu$ the atoms leak out of the lattice sites and the soliton is destroyed. This area where no soliton can exist is found on the right hand side of the red dashed line corresponding to $\nu_z \approx 4.5\,\mathrm{Hz}$. If $\Delta V/L \gtrsim V_0$ the atom cloud undergoes a free dipole oscillation in the trap demonstrated by the high accumulated effective momenta above this threshold.

---

[1] Note that the effective mass formalism is a less good approximation for the case of $V_0 = 7E_r$ than for the case of $V_0 = 2E_r$.

as obtained numerically. In our example we exceed this barrier for $\nu_z \gtrsim 0.5\,\mathrm{Hz}$. Exceeding this threshold makes the soliton move[2] in our simulations as shown in Figs. A.7 and A.6(top right) for the case of $\nu_z = 1\,\mathrm{Hz}$. Particularly interesting, the soliton moves up the potential slope. This is due to its negative effective mass. If $\Delta V/L$ exceeds the value of $\approx V_0 - \mu$ corresponding to $k_{\Delta E} = 25.3k_r$ and $\nu_z \approx 4.5\,\mathrm{Hz}$ the atoms start leaking out of the lattice sites down the potential slope and the soliton gets destroyed. As an example we show the case of $\nu_z = 5\,\mathrm{Hz}$ in Fig. A.6(bottom left). For $\Delta V/L > V_0$ the soliton is destroyed immediately and the atom cloud is undergoing a free dipolar oscillation in the harmonic trap, as shown for the example of $\nu_z = 10\,\mathrm{Hz}$ in Fig. A.6(bottom right). In Fig. A.5(right) we show the maximal momentum which the atom cloud effectively has gained during the time evolution for the different values of ν_z. We estimate this maximal momentum of the whole atom cloud by integrating over the momentum space. The result confirms our findings before.

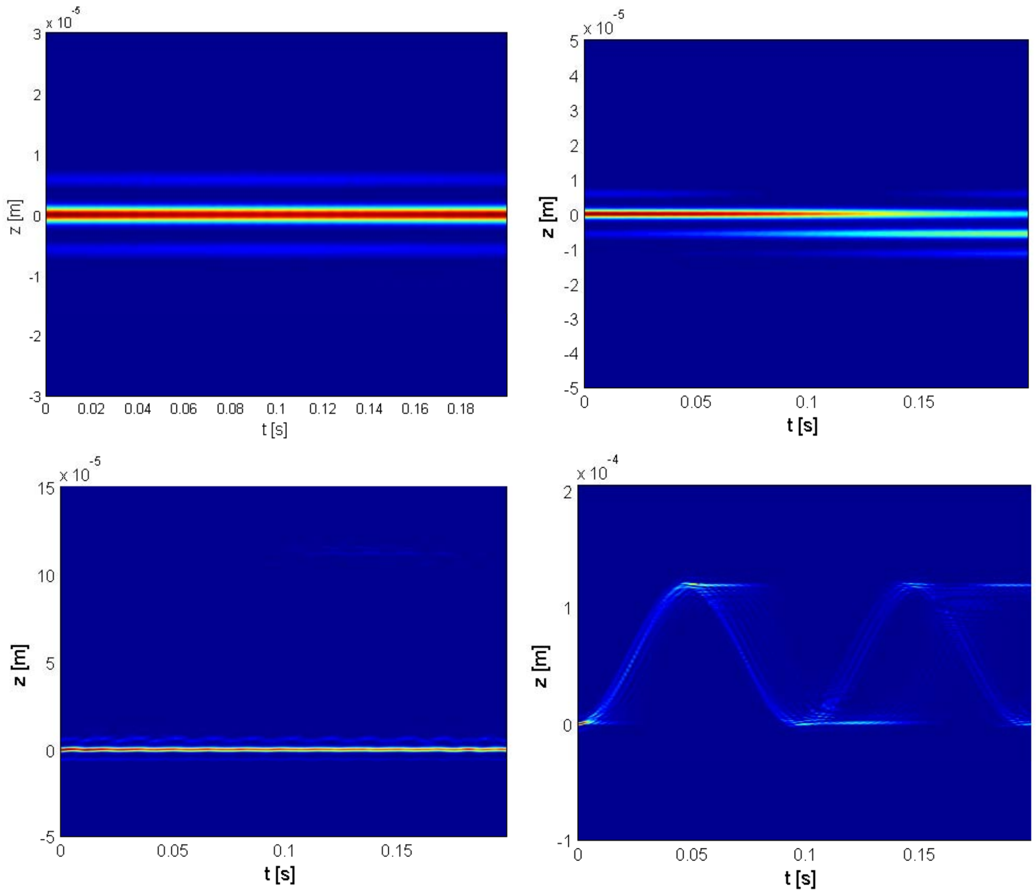

Figure A.6: Numerical simulations corresponding to different points of Fig. A.5(right). **top left**: $\nu_z = 0.1\,\mathrm{Hz}$, **top right**: $\nu_z = 1\,\mathrm{Hz}$, **bottom left**: $\nu_z = 4.5\,\mathrm{Hz}$ and **bottom right**: $\nu_z = 10\,\mathrm{Hz}$.

---

[2] Note that integrating the momentum space already leads to a finite momentum of the whole atom cloud for cases below the PNPB (see Fig A.5(right)). In these cases the soliton gets asymmetrically deformed but cannot move away.

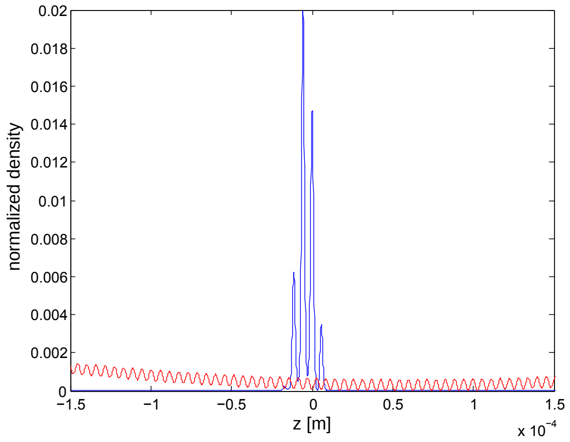

Figure A.7: If the Peierls-Nabarrow potential barrier is overcome the soliton moves "up the hill".

A check of our simulations using a linear potential slope instead of a harmonic one results in a similar behavior at the different thresholds as shown in Fig. A.8.

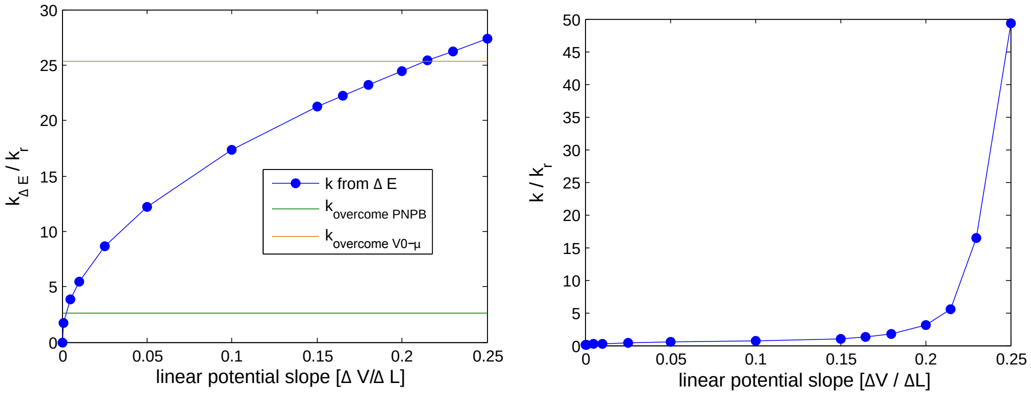

Figure A.8: **left**: Possible momenta which the soliton can gain from a linear potential slope, otherwise similar to Fig. A.5(left). **right**: Effectively gained momenta of the atom cloud. Similarly to the case of a harmonic slope the atoms starts leaking out of the lattice sites for $\Delta V/L \gtrsim V_0 - \mu$. In this case the soliton is destroyed and the atom cloud can gain a high overall momentum down the slope.

A.4 Conclusion

In conclusion we can say that it should be possible to create a fundamental discrete bright soliton by the method of [Mat2006] in our setup. Measuring the Peierls-Nabarrow potential barrier is in principle possible, but not with the experimental parameters achievable in our setup.

Appendix B

The Gross-Pitaevskii equation [Kev2008]

The many body Hamiltonian for N interacting bosons in the form of second quantization is given by:

$$\hat{H} = \int d\mathbf{r}\hat{\Psi}^\dagger(\mathbf{r}) \left[-\frac{\hbar^2}{2m}\nabla^2 + V_{ext}(\mathbf{r}) \right] \hat{\Psi}(\mathbf{r}) + ... \tag{B.1}$$

$$... + \frac{1}{2} \int d\mathbf{r}d\mathbf{r}'\hat{\Psi}^\dagger(\mathbf{r})\hat{\Psi}^\dagger(\mathbf{r}')V(\mathbf{r}-\mathbf{r}')\hat{\Psi}(\mathbf{r}')\hat{\Psi}(\mathbf{r}), \tag{B.2}$$

with the external potential $V_{ext}(\mathbf{r})$, the bosonic annihilation and creation field operators $\hat{\Psi}(\mathbf{r})$ and $\hat{\Psi}^\dagger(\mathbf{r})$ and the two-body interatomic potential $V(\mathbf{r}-\mathbf{r}')$. Using the Heisenberg equation $i\hbar(\partial\hat{\Psi}/\partial t) = [\hat{\Psi}, \hat{H}]$ for the field operator $\hat{\Psi}(\mathbf{r})$ we obtain

$$i\hbar\frac{\partial}{\partial t}\hat{\Psi}(\mathbf{r},t) = \left[-\frac{\hbar^2}{2m}\nabla^2 + V_{ext}(\mathbf{r}) + \int d\mathbf{r}'\hat{\Psi}^\dagger(\mathbf{r}',t)V(\mathbf{r}'-\mathbf{r})\hat{\Psi}(\mathbf{r}',t) \right] \hat{\Psi}(\mathbf{r},t) \tag{B.3}$$

As the interatomic interaction of a dilute ultracold gas is completely dominated by low energetic binary collisions the interatomic interaction potential can well approximated by a delta-function potential [Pet2004]: $V(\mathbf{r}'-\mathbf{r}) \approx g\delta(\mathbf{r}'-\mathbf{r})$. The interaction constant g is given by

$$g = \frac{4\pi\hbar^2 a_s}{m}, \tag{B.4}$$

with a_s the s-wave scattering length. Applying the mean field approximation the field operator can be approximated by a complex function

$$\hat{\Psi}(\mathbf{r},t) \approx \Psi(\mathbf{r},t), \tag{B.5}$$

which is commonly referred to as the macroscopic wave function of the condensate. This yields the Gross-Pitaevskii equation (GPE) [Gro1961, Pit1961]:

$$i\hbar\frac{\partial}{\partial t}\Psi(\mathbf{r},t) = \left[-\frac{\hbar^2}{2m}\nabla^2 + V_{ext}(\mathbf{r}) + g|\Psi(\mathbf{r},t)|^2 \right] \Psi(\mathbf{r},t). \tag{B.6}$$

Note that the wave function is normalized to the total atom number $N = \int |\psi(\mathbf{r},t)|^2 d\mathbf{r}$. The complex function Ψ can be expressed by: $\sqrt{n(\mathbf{r},t)}\exp(i\phi(\mathbf{r},t))$, where $n(\mathbf{r},t) = |\Psi(\mathbf{r},t)|^2$ denotes the density of the condensate and $\phi(\mathbf{r},t)$ the phase of the wave function respectively. From the expression of the current density $\mathbf{j} = \frac{\hbar}{2m}(\Psi^\star\nabla\Psi - \Psi\nabla\Psi^\star) = n\mathbf{v}$ it becomes obvious, that the velocity of the condensate is fixed by the phase $\phi(\mathbf{r},t)$ and can be expressed as:

$$\mathbf{v}(\mathbf{r},t) = \frac{\hbar}{m}\nabla\phi(\mathbf{r},t). \tag{B.7}$$

In the case of harmonically trapped BECs relevant to our experiments the external potential is given by:

$$V_{ext}(\mathbf{r}) = \frac{m}{2}(\omega_x x^2 + \omega_y y^2 + \omega_z z^2). \tag{B.8}$$

Appendix C

Term scheme of ^{87}Rb

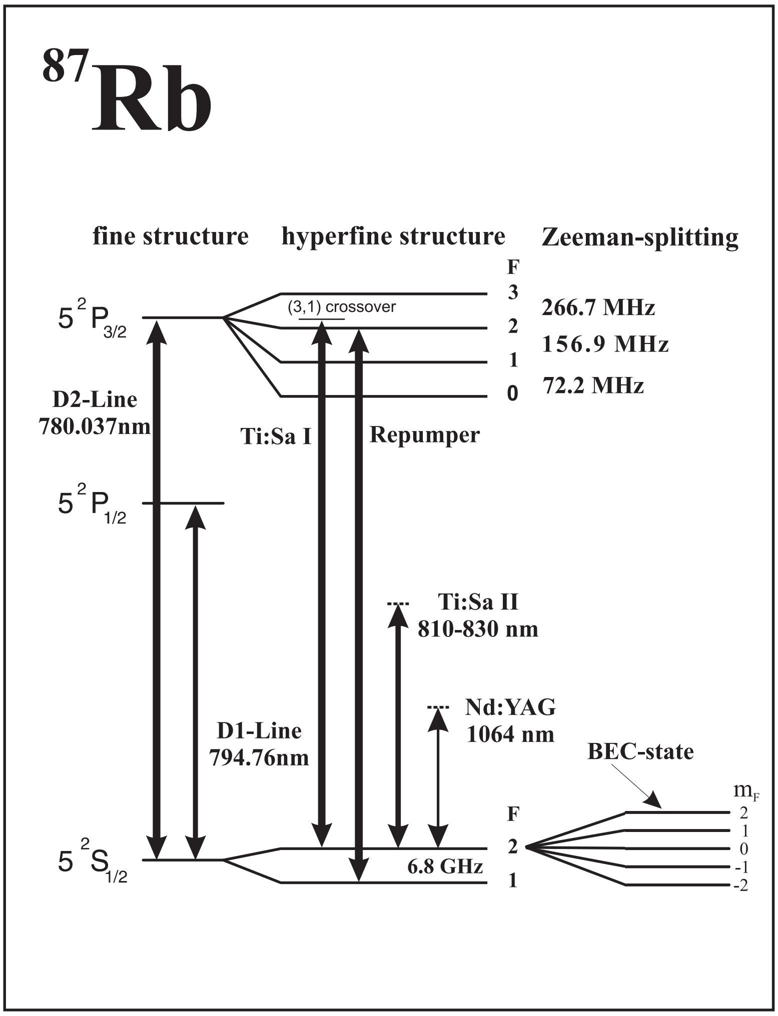

Figure C.1: Term scheme of ^{87}Rb. The transitions addressed by our laser system (see chapter 5.1.2) are marked.

Bibliography

[Ahu2004] V. Ahufinger, A. Sanpera, P. Pedri, L. Santos, and M. Lewenstein:
Creation and mobility of discrete solitons in Bose-Einstein condensates.
Phys. Rev. A, 69, 053604 (2004).

[Akh1993] Nail Akhmediev and Adrian Ankiewicz:
First-order exact solutions of the nonlinear Schrödinger equation in the normal-dispersion regime.
Phys. Rev. A, 47, 3213 (1993).

[Alb2005] Michael Albiez:
Observation of nonlinear tunneling of a Bose-Einstein condensate in a single Josephson junction.
PhD thesis, Faculty of Physics and Astronomy, University of Heidelberg (2005).

[And2001] B.P. Anderson, P.C. Haljan, C.A. Regal, D.L. Feder, L.A. Collins, C.W. Clark, and E.A. Cornell:
Watching Dark Solitons Decay into Vortex Rings in a Bose-Einstein Condensate.
Phys. Rev. Lett., 86, 2926 (2001).

[And1995] M.H. Anderson, J.R. Ensher, M.R. Matthews, C.E. Wieman, and E.A. Cornell:
Bose-Einstein Condensation in a Gas of Sodium Atoms.
Science, 269, 198 (1995).

[And1997] M.R. Andrews,C.G. Townsend, H.-J. Miesner, D.S. Durfee, D.M. Kurn, and W. Ketterle:
Observation of interference between two Bose condensates.
Science, 275, 637 (1997).

[Ank2005] Thomas Anker:
Ultracold quantum gases in one-dimensional optical lattice potentials - nonlinear matter wave dynamics -.
PhD thesis, Faculty of Physics and Astronomy, University of Heidelberg (2005).

[App2007] Jens Appmeier:
Bose-Einstein condensates in a double well potential: A route to quantum interferometry.

Diploma thesis, Faculty of Physics and Astronomy, University of Heidelberg (2007).

[Bec2008] Christoph Becker, Simon Stellmer, Parvis Soltan-Panahi, Sören Dörscher, Mathis Baumert, Eva-Maria Richter, Jochen Kronjäger, Kai Bongs, and Klaus Sengstock:
Oscillations and interactions of dark and dark-bright solitons in Bose-Einstein condensates.
Nature Physics, 4, 496 (2008).

[Blo1985] K.J. Blow and N.J. Doran:
Multiple dark soliton solutions of the Nonlinear Schrödinger Equation.
Phys. Lett. A, 107(2), 55 (1985).

[Bra2006] V.A. Brazhnyi, V.V. Konotop, and L.P. Pitaevskii:
Dark Solitons as Quasiparticles in Trapped Bose-Einstein Condensates.
Phys. Rev. A, 73, 053601 (2006).

[Bur1999] S. Burger, K. Bongs, S. Dettmer, W. Ertmer, K. Sengstock, A. Sanpera, G.V. Shlyapnikov, and M. Lewenstein:
Dark Solitons in Bose-Einstein Condensates.
Phys. Rev. Lett., 83, 5198 (1999).

[Bur2002] S. Burger, L.D. Carr, P. Öhberg, K. Sengstock, and A. Sanpera:
Generation and interaction of solitons in Bose-Einstein condensates.
Phys. Rev. A, 65, 043611 (2002).

[Bus2000] Th. Busch and J.R. Anglin:
Motion of Dark Solitons in Trapped Bose-Einstein Condensates.
Phys. Rev. Lett., 84, 2298 (2000).

[Che1993] M. Chen, M.A. Tsankov, J.M. Nash, and C.E. Patton:
Microwave magnetic-envelope dark solitons in yttrium iron garnet thin films.
Phys. Rev. Lett, 70, 1707 (1993).

[Dav1995] K.B. Davis, M.-O. Mewes, M.R. Andrews, N.J. van Druten, D.S. Durfee, D.M. Kurn, and W. Ketterle:
Bose-Einstein Condensation in a Gas of Sodium Atoms.
Phys. Rev. Lett., 75, 3969 (1995).

[Den1990] B. Denardo, W. Wright, S. Putterman, and A. Larraza:
Observation of a kink soliton on the surface of a liquid.
Phys. Rev. Lett., 64, 1518 (1990).

[Den1992] B. Denardo, B. Galvin, A. Greenfield, A. Larraza, S. Putterman, and W. Wright:
Observations of localized structures in nonlinear lattices: Domain walls and kinks.
Phys. Rev. Lett, 68, 1730 (1992).

[Den2000] J. Denschlag, J.E. Simsarian, D.L. Feder, Charles W. Clark, L.A. Collins, J. Cubizolles, L. Deng, E.W. Hagley, K. Helmerson, W.P. Reinhardt,

S.L. Rolston, B.I. Schneider, and W.D. Phillips:
Generating Solitons by Phase Engineering of a Bose-Einstein Condensate.
Science, Vol. 287, 97 (2000).

[Dut2001] Zachary Dutton, Michael Budde, Christopher Slowe, Lene Vestergaard Hau:
Observation of Quantum Shock Waves Created with Ultra-Compressed Slow Light Pulses in a Bose-Einstein Condensate.
Science, 293, 663 (2001).

[Eie2004] Bernd Eiermann:
Kohärente nichtlineare Materiewellendynamik- Helle atomare Solitonen.
PhD thesis, Faculty of Physics, University of Konstanz (2004).

[EieII2004] B. Eiermann, Th. Anker, M. Albiez, M. Taglieber, P. Treutlein, K.-P. Marzlin,and M. K. Oberthaler:
Bright Bose-Einstein Gap Solitons of Atoms with Repulsive Interaction.
Phys. Rev. Lett., 92, 230401 (2004).

[Eis1998] H. S. Eisenberg, Y. Silberberg, R. Morandotti, A. R. Boyd, and J. S. Aitchison:
Discrete Spatial Optical Solitons in Waveguide Arrays.
Phys. Rev. Lett., 81, 3383 (1998).

[Emp1987] P. Emplit, J. P. Hamaide, F. Reynaud, C. Froehly and, A. Barthelemy:
Picosecond steps and dark pulses through nonlinear single mode fibers.
Opt. Comm, 62, 374 (1987).

[Eng2007] P. Engels and C. Atherton:
Stationary and Nonstationary Fluid Flow of a Bose-Einstein Condensate Through a Penetrable Barrier.
Phys. Rev. Lett., 99, 160405 (2007).

[Est2008] J. Estève, C. Gross, A. Weller, S. Giovanazzi and M.K. Oberthaler:
Squeezing and entanglement in a Bose-Einstein condensate.
Nature, 455, 1216 (2008).

[Fed1999] P.O. Fedichev, A.E. Muryshev, and G.V. Shlyapnikov:
Dissipative dynamics of a kink state in a Bose-condensed gas.
Phys. Rev. A, 60, 3220 (1999).

[Fei1982] M.D. Feit J.A. Fleck Jr., and A. Steiger:
Solution of the Schrödinger equation by a spectral method.
J. Computational Phys., 47, 412 (1982).

[Gas1987] P. De Gasperis, R. Marcelli, and G. Miccoli:
Magnetostatic Soliton Propagation at Microwave Frequency in Magnetic Garnet Films.
Phys. Rev. Lett., 59, 481 (1987).

[Gat2006] Rudolf Gati:
Bose-Einstein Condensates in a Single Double-Well Potential.
PhD thesis, Faculty of Physics and Astronomy, University of Heidelberg (2006).

[GatII2006] R. Gati, B. Hemmerling, J. Fölling, M. Albiez, and M.K. Oberthaler:
Noise Thermometry with Two Weakly Coupled Bose-Einstein Condensates.
Phys. Rev. Lett., 96, 130404 (2006).

[Gro1961] E.P. Gross:
Structure of a quantized vortex in boson systems.
Nuovo Cimento, 20, 454 (1961).

[Gro] C. Groß:
PhD thesis, Faculty of Physics and Astronomy, University of Heidelberg (to be published).

[Hel2001] D. Hellweg, S. Dettmer, P. Ryytty, J.J. Arlt, W. Ertmer, K. Sengstock, D.S. Petrov, G.V. Shlyapnikov, H. Kreutzmann, L. Santos, and M. Lewenstein:
Phase fluctuations in Bose-Einstein condensates.
Appl. Phys. B, 73, 781 (2001).

[Ket1999] W. Ketterle, D.S. Durfee, and D.M. Stamper-Kurn:
Making, probing and understanding Bose-Einstein condensates.
Bose-Einstein Condensation in Atomic Gases, Editors: M. Inguscio, S. Stringari, and C. Wieman.
IOS Press, Amsterdam, ISBN: 978-0-96733-555-1 (1999).

[Kev] P.G. Kevrekidis:
Private communication.
University of Massachusetts, Amherst, USA.

[Kev2008] P.G. Kevrekidis, D.J. Frantzeskakis and R. Carretero-González:
The Gross-Pitaevskii (GP) Mean-Field Model.
Emergent Nonlinear Phenomena in Bose-Einstein Condensates, Editors: P.G. Kevrekidis, D.J. Frantzeskakis and R. Carretero-González.
Springer-Verlag, Berlin Heidelberg New York, ISBN: 978-3-540-73590-8 (2008).

[Kiv1993] Yuri S. Kivshar:
Dark Solitons in Nonlinear Optics.
Quantum Electron., 29, 250 (1993).

[Kiv1995] Yuri S. Kivshar, Wieslaw Królikowski:
Lagrangian approach for dark solitons.
Opt. Comm., 114, 353 (1995).

[Kiv1998] Y.S. Kivshar and B. Luther-Davies:
Dark Optical Solitons: Physics and Applications.
Phys. Rep., 298, 81 (1998).

[Kon2004] Vladimir Konotop and Lev Pitaevskii:
Landau Dynamics of a Grey Soliton in a Trapped Condensate.
Phys. Rev. Lett., 93, 240403 (2004).

[Kor1895] D.J. Korteweg and F. de Fries:
On the Change of Form of Long Waves Advancing in a Rectangular Canal, and on a New Type of Long Stationary Waves.
Philosophical Magazine, 39, 422 (1895).

[Kro1988] D. Krökel, N. J. Halas, G. Giuliani, and D. Grischkowsky:
Dark-Pulse Propagation in Optical Fibers.
Phys. Rev. Lett, 60, 29 (1988).

[Kuz1988] E.A. Kuznetsov and S.K. Turitsyn:
Instability and collapse of solitons in media with a defocusing nonlinearity.
Sov. Phys. JETP, 67, 1583 (1988).

[Lif1995] E.M. Lifshitz and L. Pitaevskii:
Physical Kinetics.
Butterworth-Heinemann Ltd., Oxford (1995).

[Mat] M. Matuszewski:
Private communication.
Australian National University, Canberra, Australia.

[Mat2006] M. Matuszewski, W. Królikowski, M. Trippenbach, and Y.S. Kivshar:
Simple and efficient generation of gap solitons in Bose-Einstein condensates.
Phys. Rev. A, 73, 063621 (2006).

[Mat2008] A. Muñoz Mateo and V. Delgado:
Effective mean-field equations for cigar-shaped and disk-shaped Bose-Einstein condensates.
Phys. Rev. A, 77, 013617 (2008).

[Mat2009] A. Muñoz Mateo and V. Delgado:
Effective one-dimensional dynamics of elongated Bose-Einstein condensates.
Ann. Phys, 324, 709 (2009).

[Men2002] Chiara Menotti and Sandro Stringari:
Collective oscillations of a one-dimensional trapped Bose-Einstein gas.
Phys. Rev. A, 66, 043610 (2002).

[Met1999] Harold J. Metcalf and Peter van der Straten:
Laser Cooling and Trapping.
Springer-Verlag, New York, ISBN: 0-387-98728-2 (1999).

[Mol1980] L.F. Mollenauer, R.H. Stolen, and J.P. Gordon:
Experimental Observation of Picosecond Pulse Narrowing and Solitons in Optical Fibers.
Phys. Rev. Lett., 45, 1095 (1980).

[Mor1997] S.A. Morgan, R.J. Ballagh, and K. Burnett:
Solitary-wave solutions to nonlinear Schrödinger equations.
Phys. Rev. A, 55, 4338 (1997).

[Mur1999] A.E. Muryshev, H.B. van Linden van den Heuvell, and G.V. Shlyapnikov:
Stability of standing matter waves in a trap.
Phys. Rev. A, 60, R2665 (1999).

[Mur2002] A. Muryshev, G.V. Shlyapnikov, W. Ertmer, K. Sengstock, and M. Lewenstein:
Dynamics of Dark Solitons in Elongated Bose-Einstein Condensates.
Phys. Rev. Lett., 89, 110401 (2002).

[Ott2006] Timo B. Ottenstein:
A new Objective for High Resolution Imaging of Bose-Einstein Condensates.
Diploma thesis, Faculty of Physics and Astronomy, University of Heidelberg (2006).

[Pet1995] W. Petrich, M. Anderson, J. Ensher, and E. Cornell:
Stable, Tightly Confining Magnetic Trap for Evaporative Cooling of Neutral Atoms.
Phys. Rev. Lett., 74, 3352 (1995).

[Pet2004] C.J. Pethick and H. Smith:
Bose Einstein Condensation in Dilute Gases.
Cambridge University Press, Camebridge (2004).

[Pit1961] L.P. Pitaevskii:
Vortex lines in an imperfect bose gas.
Sov. Phys. JETP, 13, 451 (1961).

[Raa1987] E.L. Raab, M. Prentiss, A. Cable, S. Chu, and D.E. Pritchard:
Trapping of Neutral Sodium Atoms with Radiation Pressure.
Phys. Rev. Lett., 59, 2631 (1987).

[Ron2008] J.P. Ronzheimer:
Interactions of Dark Solitons in cigar shaped Bose-Einstein Condensates.
Diploma thesis, Faculty of Physics and Astronomy, University of Heidelberg (2008).

[Rus1844] J.S. Russel:
Report on waves.
Fourteenth meeting of the British Association for the Advancement of Science (1844).

[Sal2002] L. Salasnich, A. Parola, and L. Reatto:
Effective wave equations for the dynamics of cigar-shaped and disk-shaped Bose condensates.
Phys. Rev. A, 65, 043614 (2002).

[Sco1998] T.F. Scott, R.J. Ballagh, and K. Burnett:
Formation of fundamental structures in Bose-Einstein condensates.
J. Phys. B, 31, L329 (1998).

[Sho2008] I. Shomroni, E. Lahoud, S. Levy, and J. Steinhauer:
Evidence for an oscillating soliton/vortex ring by density engineering of a Bose-Einstein condensate.
Nature Physics, 5, 193 (2009).

[Ste2008] S. Stellmer, C. Becker, P. Soltan-Panahi, E.-M. Richter, S. Dörscher, M. Baumert, J. Kronjäger, K. Bongs, and K. Sengstock:
Collisions of Dark Solitons in Elongated Bose-Einstein Condensates.
Phys. Rev. Lett., 101, 120406 (2008).

[The] G. Theocharis:
Private communication.
University of Massachusetts, Amherst, USA.

[The2007] G. Theocharis, P.G. Kevrekidis, M.K. Oberthaler, and D.J. Frantzeskakis:
Dark matter-wave solitons in the dimensionality crossover.
Phys. Rev. A, 76, 045601 (2007).

[Vri1986] P.L. De Vries:
Application of the Split Operator Fourier Transform Method to the Solution of the Nonlinear Schŕodinger Equation.
AIP Conference Proceedings, 160, 269 (1986).

[Wei1988] A. M. Weiner, J. P. Heritage, R. J. Hawkins, R. N. Thurston, E. M. Kirschner, D. E. Leaird, and W. J. Tomlinson:
Experimental Observation of the Fundamental Dark Soliton in Optical Fibers.
Phys. Rev. Lett, 61, 2445 (1988).

[Wel2008] A. Weller, J.P. Ronzheimer, C. Gross, J. Esteve, M.K. Oberthaler, D. J. Frantzeskakis, G. Theocharis, and P. G. Kevrekidis:
Experimental Observation of Oscillating and Interacting Matter Wave Dark Solitons.
Phys. Rev. Lett., 101, 130401 (2008).

[Zak1972] V.E. Zakharov and A.B. Shabat:
Exact theory of two-dimensional self-focusing and onedimensional self-modulation of waves in nonlinear media.
Sov. Phys. JETP, 34, 62 (1972).

[Zak1973] V.E. Zakharov and A.B. Shabat:
Interaction between solitons in a stable medium.
Sov. Phys. JETP, 37, 823 (1973).

[Zar1998] E. Zaremba:
Sound propagation in a cylindrical Bose-condensed gas.
Phys. Rev. A, 57, 518 (1998).

Acknowledgements / Danksagung

I would like to thank all people who supported me during the time of my thesis, who contributed to this work and without whom this work would not exist in the current form:

I would like to thank Prof. Markus Oberthaler for having given the chance to me to work on a very interesting topic in one of the most flourishing fields in current physical research. I have gained a deeper insight into physics in his group, on the experimental side as well as on the theoretical side. His enthusiasm and motivation made the team reach for high goals and finally get them. I also thank him for his patience with me, as I came from a very different field and had to learn a lot of things from the scratch. Especially, I thank him for always having found the right words in critical situations not only concerning physical but also private problems.

I would like to thank Prof. Peter Schmelcher for agreeing to evaluate this thesis and to write the second referee report. Especially I thank him for his interest in our work.

I thank Jerome Estève who was our team leader for most of the time during this thesis. His great physical knowledge and his talent always impressed me very much and I could learn a lot from him. He (nearly ;-)) always had the right answer to any kind of physical problem.

I thank my PHD colleague Christian Groß, a physicist with excellent experimental as well as theoretical skills. I could learn many things from him. I thank him for always having been a fair colleague open for any kind of discussions. We went together through good and bad times of the experiment. When nothing worked he always had the enthusiasm to change things from the scratch.

Especially I thank our Diploma student Philipp Ronzheimer with whom I closely worked together on the performance of the soliton measurements and on the subsequent data evaluation and numerical modeling. He was a great enrichment for the soliton project. Especially his continuously pushing forward of the effective potential approach helped us gaining a deeper insight into the physics of the soliton interaction. We always worked together in an enjoyable way and had a lot of fruitful

discussions.

Prof. Panayotis Kevrekidis, Georgios Theocharis and Prof. Dimitri Frantzeskakis I would like to thank for their continuous support from the theory side. Their ideas made us aware that we can measure the inter-soliton interaction as an increase of the oscillation frequency of the solitons. I enjoyed very much the time when Panos was a guest here in Heidelberg, when we had many fruitful discussions.

I thank Eike Nicklas and Tilman Zibold, who both started as Diploma students and are now PHD students, for their contributions to the experiment and their help.

I thank all members of the BEC group for the nice atmosphere, which had always the character of a real team.

Jens Appmeier, Rudolf Gati, Karsten Joho and Timo Ottenstein I thank for their contributions to the experiment, their help and the nice atmosphere during my initial time in the group.

Philipp Ronzheimer, Fabienne Haupert, Jerome Estève, Christian Groß, Georgios Theocharis and Eike Nicklas I thank for helping me with the correction of this thesis.

Additionally I would like to thank all other people of the group from the NaLi-, ATTA- and Argon-Experiment for the great overall atmosphere in the group and the fun we had.

I thank our team-assistants Dagmar Hufnagel und Christiane Jäger for their continuous support on any kind of problems.

The staff of the mechanics- and electronics workshop I thank for building a lot of important devices for our setup.

Außerdem möchte ich mich bei den Menschen bedanken, die alle Höhen und Tiefen während dieser Zeit mit mir zusammen durchlebt haben.

Ich danke meinen Eltern, die mich während meiner gesamten Ausbildung immer unterstützt haben und immer an mich geglaubt haben. Leider konnte meine Mutter das Ende dieser Arbeit und diesen Punkt in meinem Leben nicht mehr miterleben. Ihr Tod in 2007 war ein schwerer Verlust für meine Familie und hat mich sehr getroffen.

Mein ganz besonderer Dank gilt meiner Frau Julia, die immer an meiner Seite war, ganz egal was auch passierte. Ohne sie hätte ich es nicht geschafft.